Measuring D(4000) in z$\sim$1.6 galaxies using WFC3/G102L observations with HST: a feasibility study

By

Brittany Henke

Submitted to the Department of Physics and Astronomy and the
Graduate Faculty of the University of Kansas
in partial fulfillment of the requirements for the degree of
Master of Science

Dr. Gregory Rudnick, Chairperson

Committee members

Dr. Bruce Twarog

Dr. Mikhail Medvedev

Date defended: February 2, 2015

The Thesis Committee for Brittany Henke certifies
that this is the approved version of the following thesis :

Measuring D(4000) in z$\sim$1.6 galaxies using WFC3/G102L observations with HST: a feasibility study

Dr. Gregory Rudnick, Chairperson

Date approved: February 2, 2015

Abstract

This is a feasibility study for the analysis of *Hubble Space Telescope* observations of galaxy cluster IRC 0218A at a redshift of z = 1.62. The main goals were as follows: to investigate any systematic biases in $D(4000)$ and $D_n(4000)$, commonly used indices for probing a galaxy's average stellar age, for different star formation histories, ages, metallicities, and dust extinctions; to determine the precision with which $D(4000)$ and $D_n(4000)$ can be measured for galaxies at a range of magnitudes; and to constrain the conditions under which a measurement of $D(4000)$ or $D_n(4000)$ is a reliable probe of a galaxy's average stellar age. A grid of template galaxies was constructed using the GALAXEV package described by Bruzual & Charlot (2003), and the *Hubble* observations were simulated using the Space Telescope Science Institute's aXeSIM software package. No obvious systematic biases in $D(4000)$ or $D_n(4000)$ were observed. $D(4000)$ and $D_n(4000)$ could be accurately measured within a 10% uncertainty up to the study's J-band magnitude limit of 22.8 and within a 5% uncertainty up to a J-band magnitude of 21.6. However, even these small errors in $D(4000)$ correspond to large errors in calculated stellar age. A measurement of $D(4000)$ or $D_n(4000)$ can only roughly constrain the age of a galaxy's stellar population for J-band magnitudes brighter than ~ 21.6.

Acknowledgements

Many thanks to Professor Gregory Rudnick for guidance in this project and to the Madison & Lila Self Graduate Fellowship for financial support.

Contents

List of Figures

Chapter 1

Introduction

1.1 Galaxy Evolution

Galaxies plotted on a color-magnitude (or color-mass) diagram tend to exhibit a bimodal distribution of red quiescent galaxies and blue star-forming galaxies. Bell et al. (2004) first noticed this pattern at all redshifts out to z $\sim$ 1. Red galaxies, which generally display early-type morphologies, arrange themselves onto what is commonly known as the 'red sequence.' Blue galaxies, most often with late-type morphologies, lie in another distinct region of color-magnitude space called the 'blue cloud.' In between the red sequence and the blue cloud lies the 'green valley,' where very few galaxies exist. Figure 1.1, taken from Faber et al. (2007), shows a simple schematic of the galaxy color-mass diagram.

In nearby galaxies, the light-weighted stellar ages of star-forming and quiescent galaxies have been found to correlate with galaxy mass (e.g., Gallazzi et al., 2005; Mateus et al., 2006). Low-mass galaxies are typically dominated by young stellar populations, while massive galaxies are old. The trend of increasing light-weighted age with increasing mass is already well established at z = 0.7 (Gallazzi et al., 2014); the most massive galaxies in the Gallazzi et al. (2014) study at this so-called intermediate redshift generally contain the oldest stellar populations. The behavior of the age-versus-mass relation for even higher-redshift galaxies, such as the cluster galaxies at the focus

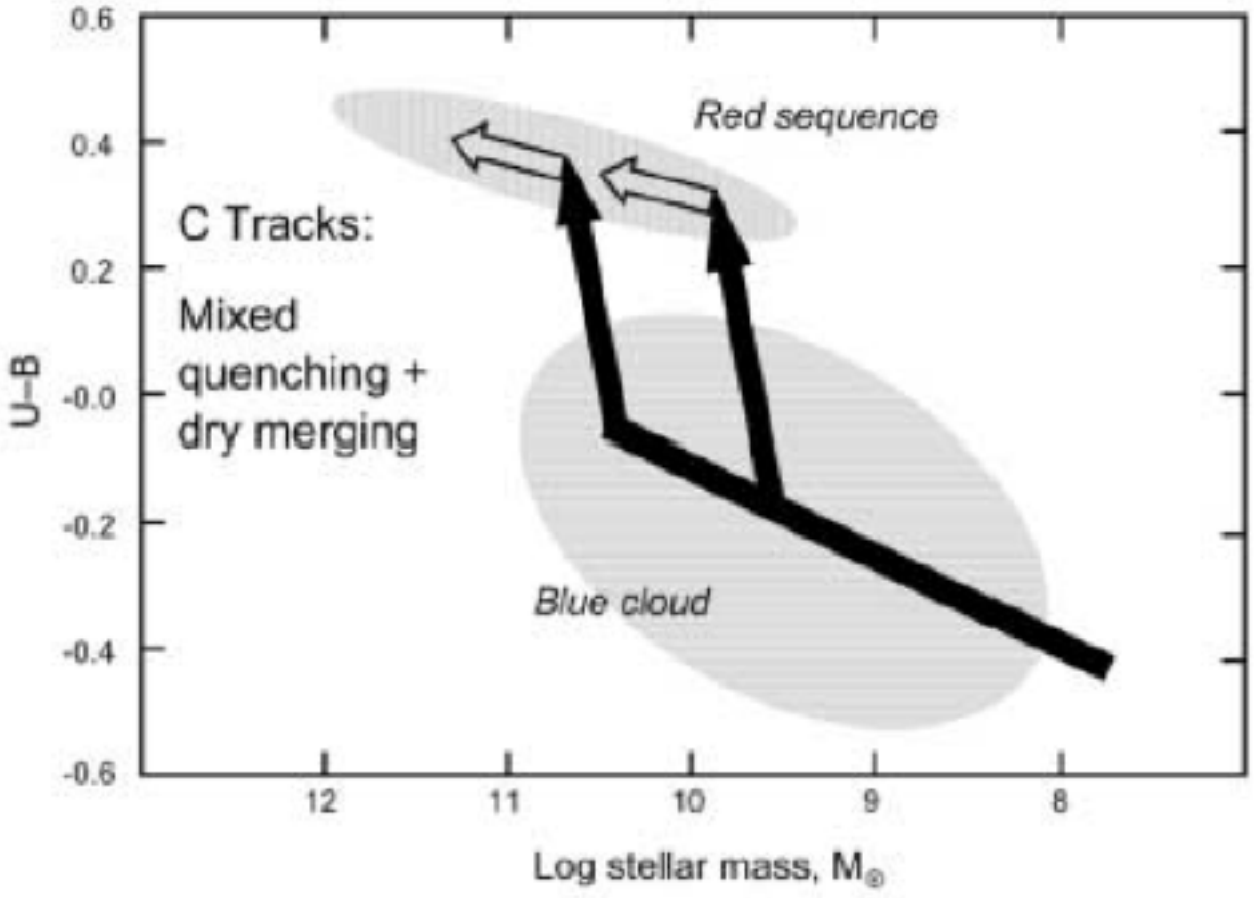

Figure 1.1: Schematic of galaxy color-mass diagram showing the blue cloud, the red sequence, and possible galaxy evolutionary tracks (Faber et al., 2007). Black arrows show galaxies migrating from the blue cloud to the red sequence through some unspecified quenching process during major mergers. White arrows show galaxies evolving along the red sequence through gas-poor, or "dry," mergers and aging of the stellar populations.

of this study, is a fascinating question.

In the local Universe, the color-magnitude diagram is characterized by a strong red sequence, which hosts galaxies with low star formation rates, very little cold gas, and usually high masses (Kauffmann et al., 2003). A population of these red, quiescent galaxies has even been observed out to z $\sim$ 2, about 3.3 Gyr after the big bang (e.g., Labbé et al., 2005; Daddi et al., 2005; Cassata et al., 2008; Kriek et al., 2008; Brammer et al., 2009). Remarkably, since z $\sim$ 1 the galaxy color-magnitude diagram has changed rapidly; the colors of the blue cloud have become redder and the number density of blue luminous galaxies has fallen, while there has been a drastic increase in stellar mass on the red sequence (e.g., Bell et al., 2004; Brown et al., 2007; Faber et al., 2007) and a corresponding increase in number density of massive quiescent galaxies (Muzzin et al., 2013a; Moustakas et al., 2013; Ilbert et al., 2013; Brammer et al., 2011; Borch et al., 2006). This dramatic growth of the red galaxy population has proven to be an enduring problem in astronomy, making the study of passive galaxies at all redshifts very important. It is likely that both galaxy mergers and star formation quenching in a fraction of the blue galaxies have likely been driving the radical evolution in the color-magnitude diagram (Bell et al., 2004; Faber et al., 2007).

The study of galaxy clusters in particular is vital to solving the problem of rapid red sequence growth from high redshifts to today. Galaxy clusters are the largest gravitationally-bound structures in the Universe. Many researchers consider them test beds for understanding the mechanisms by which star formation is quenched. Because the cooling of gas from the intracluster medium is considered inefficient and the large relative velocities in a cluster prevent merging, most cluster galaxies that leave the blue cloud never return (Rudnick et al., 2012). Most importantly, measuring the evolution of galaxies in clusters allows researchers to constrain theoretical models of galaxy evolution.

Furthermore, it appears that the dense cluster environment does play a role in truncation of star formation. Newman et al. (2014), in a study of a cluster at z = 1.8, find a high fraction of quenched systems compared to coeval field galaxies of the same mass. Interestingly, the mean ages of the quenched galaxies do not differ from the field samples, implying that the specific quenching mech-

anism, internal or external, that affects a galaxy has no large effect on when truncation actually occurs. The relative importance of environmentally related processes, such as ram-pressure stripping, gas starvation, and galaxy-galaxy interactions, and internal mechanisms, such as feedback from supernovae and active galactic nuclei, as they relate to the cessation of star formation is an area of active research (Newman et al., 2014).

Understanding the entire history of star formation quenching in the field and in clusters helps to unravel the relative importance of internal and external quenching processes. Consequently, the high-redshift cluster environment is an attractive target to investigate. The rate of increase in number density of quiescent galaxies and stellar mass on the red sequence appears most rapid around z $\geq$ 1.3 (Newman et al., 2012). Most of the stars in cluster galaxies are forming at these high redshifts, and many clusters are assembling. Detailed analyses of the stellar populations of high-redshift red cluster galaxies can help disentangle the processes responsible for the growth of the red sequence at this point in cosmic history. Due to observational difficulties, only a few galaxy clusters harboring a red galaxy population at z > 1.6 have been found (e.g., Papovich et al., 2010; Gobat et al., 2013; Stanford et al., 2012; Zeimann et al., 2012; Muzzin et al., 2013b; Tanaka et al., 2013; Galametz et al., 2013). This paper focuses on the galaxy cluster at z = 1.62 in Papovich et al. (2010).

1.2 $D(4000)$ and $D_n(4000)$

In a galaxy's spectrum, just blueward of 4000 Å lies what is known as the 4000-Å break (Bruzual & Charlot, 2003). The break is caused by the accumulation of a large number of metal absorption lines prominent in cool stars. These lines are nonexistent in young, hot stars because the metals are ionized. The strength of the 4000-Å break is often measured by a discontinuity index called $D(4000)$. Originally defined by Bruzual A. (1983), $D(4000)$ is the ratio of the average flux density F_ν in the bands 3750-3950 and 4050-4250 Å. It probes the light-weighted stellar age of a galaxy and is less affected by extinction than (U-V).

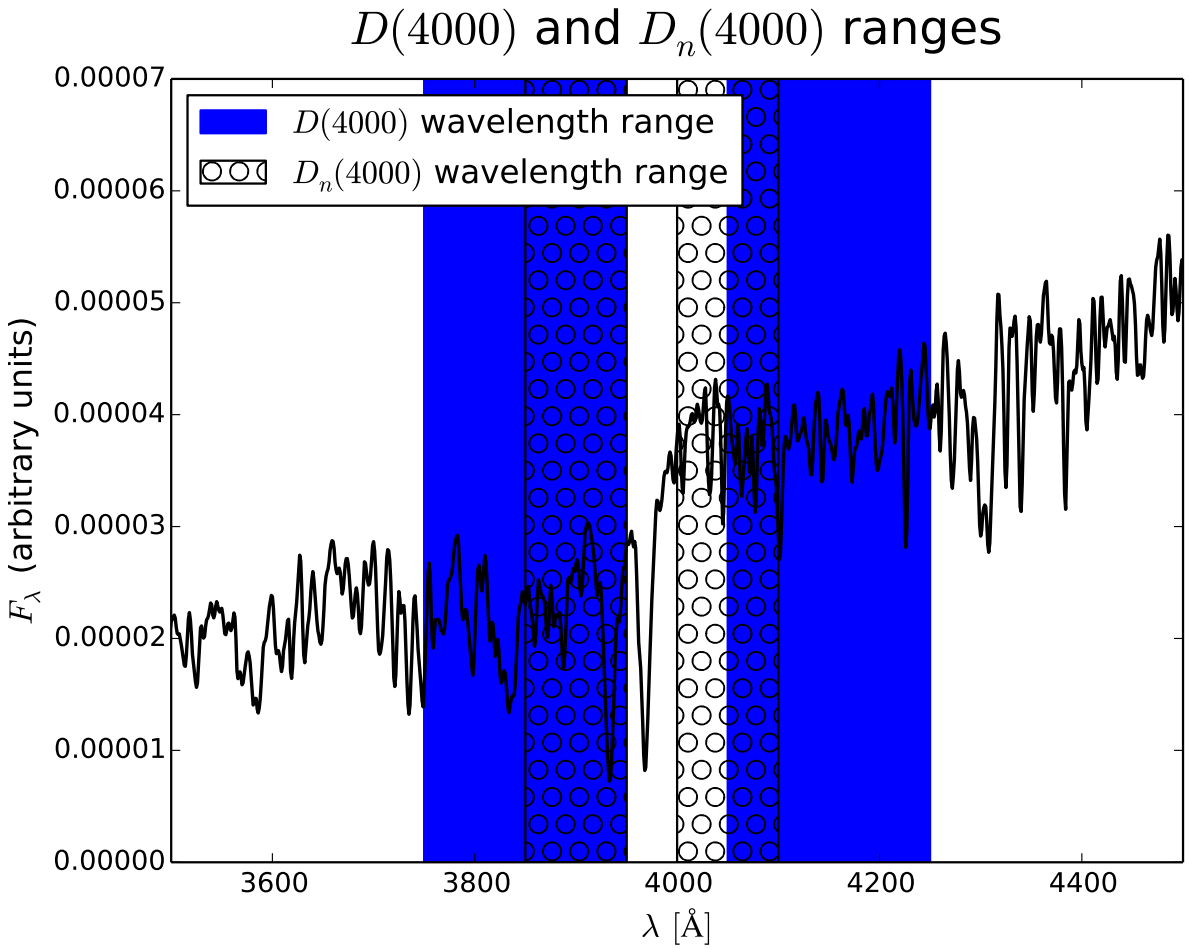

Figure 1.2: The ranges used for the $D(4000)$ and $D_n(4000)$ indices. The narrower bands used by $D_n(4000)$ lead to an index that is less sensitive to reddening effects than $D(4000)$. The spectrum used in this example corresponds to a galaxy with solar metallicity and no dust extinction, 3.0 Gyr after the end of star formation.

More commonly used in recent studies is $D_n(4000)$, which uses the narrower bands 3850-3950 and 4000-4100 Å and is less sensitive to reddening effects (Balogh et al., 1999). Either index is a good indicator of recent star formation, since the index increases with age for certain star formation histories (Hernán-Caballero et al., 2013). It is worth noting that $D(4000)$ and $D_n(4000)$ are sensitive to metallicity, as they are produced by metallic lines. Figure 1.2 shows the wavelength ranges used by the index, and Figure 1.3 shows how the indices change with star formation rate (SFR) for a simple star formation history.

My aim in this project was to measure $D(4000)$ and $D_n(4000)$ for a grid of model galaxies

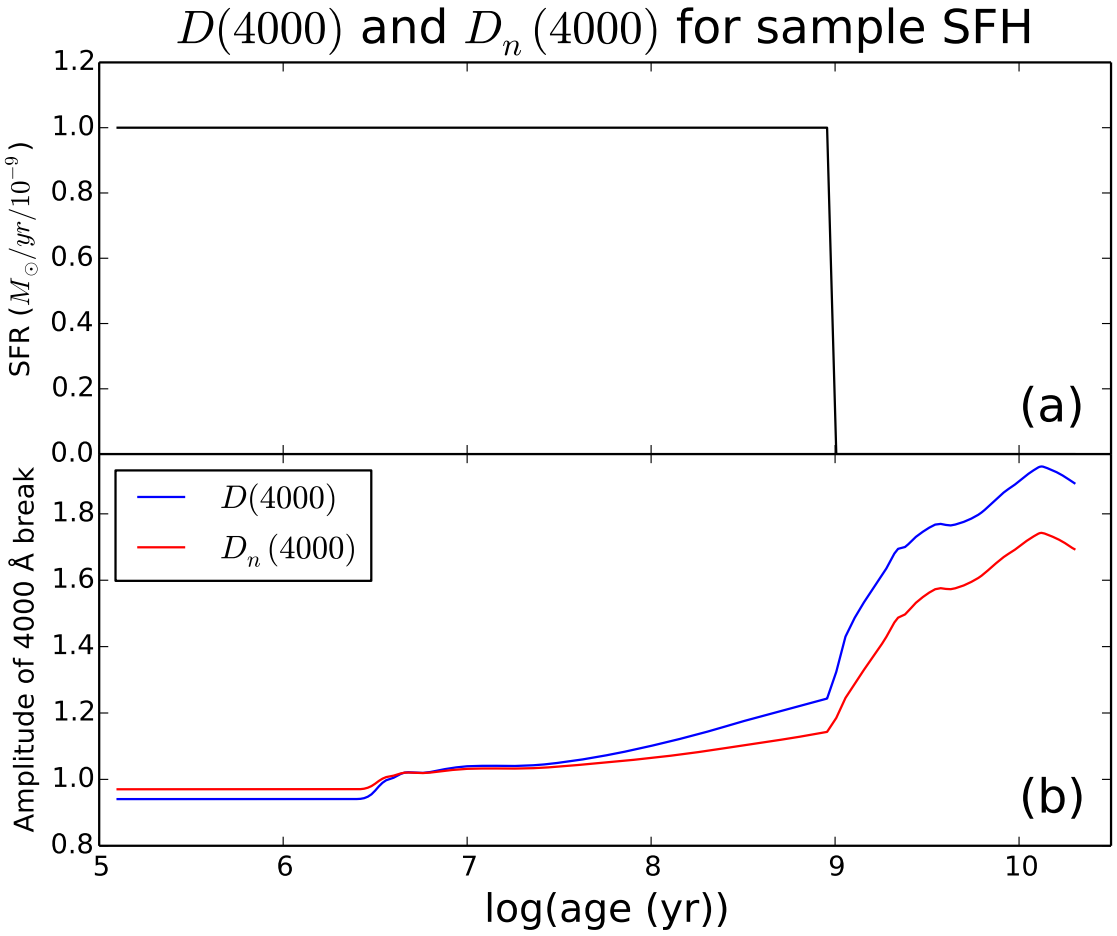

Figure 1.3: Star formation rate and amplitude of the 4000 Å break using the $D(4000)$ and $D_n(4000)$ measurements. This simple star formation history, in which SFR is constant for a time before dropping abruptly to zero, was the only model considered in this feasibility study.

artificially placed at z = 1.62 and determine if the two indices are systematically biased for different star formation histories, ages, metallicities, and optical depths. I explored the random error associated with different galaxy magnitudes to determine the precision with which $D(4000)$ can be reconstructed, and I found the uncertainty in average stellar age obtained by measuring $D(4000)$.

1.3 Wide Field Camera 3

The observations relevant to this project were made with Wide Field Camera 3 (WFC3), an infrared imager aboard the *Hubble Space Telescope* (*HST*; Dressel, 2014). WFC3 includes two infrared grisms for slitless spectroscopy. Slitless spectroscopy, unlike traditional spectroscopy, does not involve slits which only allow light from small sources to be diffracted. Instead, this technique spreads each source in a field into its dispersed spectrum. See Figure 1.4, taken from Brammer et al. (2012), for a demonstration of slitless spesctroscopy using a WFC3 grism. A grism is a combination of a grating and a prism, resulting in the dispersive effects of the grating being superimposed on those of the prism. A grism creates a dispersed spectrum, centered on the object's location. Grisms are often useful because they allow flexible combinations of resolution and wavelength.

The WFC3 grism called G102L, used by my collaborators to observe galaxy cluster IRC 0218A, is capable of observing at wavelengths between 850 and 1140 nm. At z = 1.62, the redshift of IRC 0218A, the 4000-Å break is contained within this range.

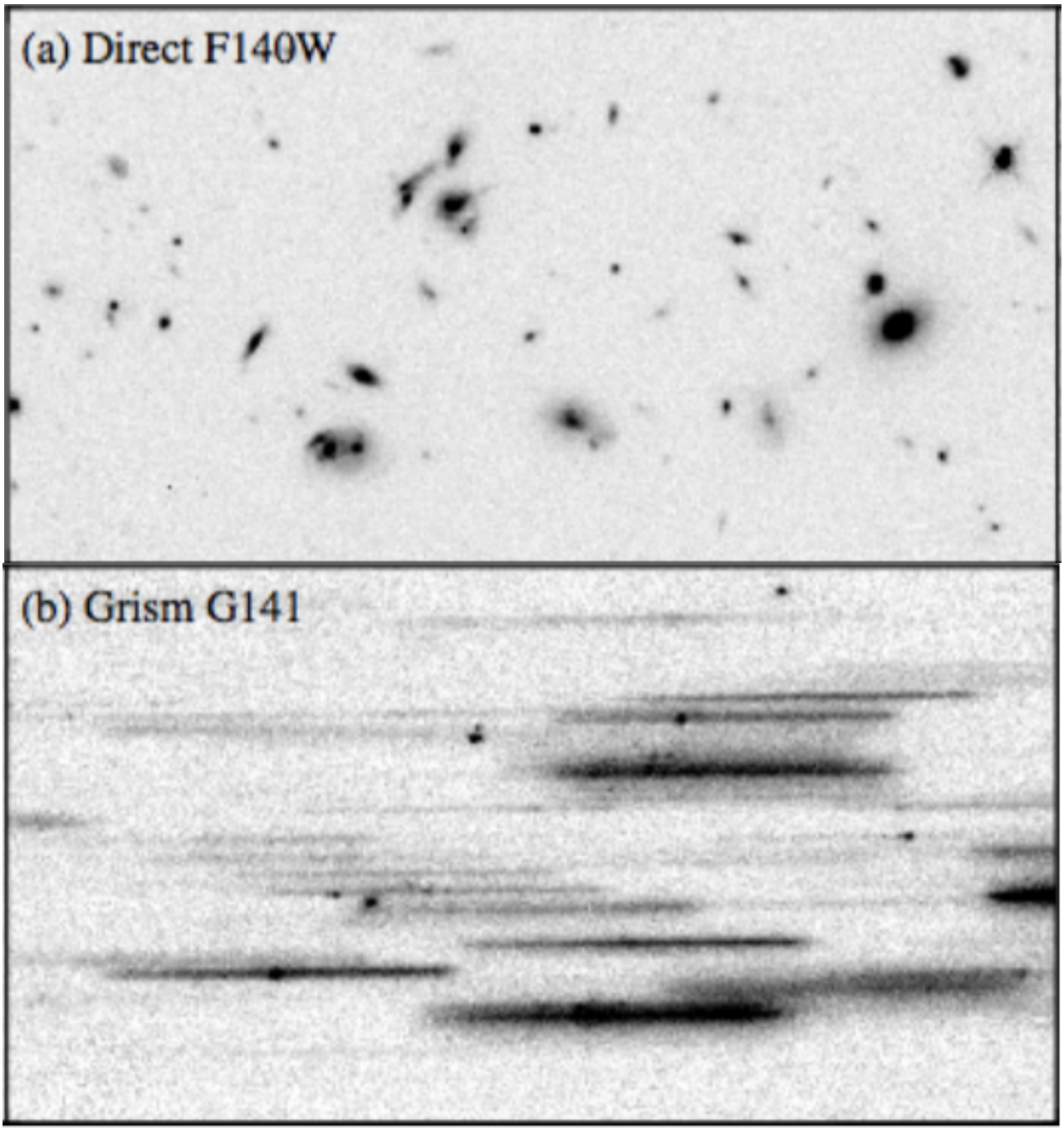

Figure 1.4: Demonstration of slitless spectroscopy using a WFC3 grism aboard HST (Brammer et al., 2012). The observed direct image of a 50" $\times$ 28" cutout within the GOODS-South field is shown in (a), and its corresponding grism panel is shown in (b), with wavelength increasing toward the right.

Chapter 2

Methods

2.1 Population Synthesis Model

I built a grid of model galaxies using the GALAXEV package described by Bruzual & Charlot (2003). Their population synthesis model relies on the fact that the star formation history (SFH) and other physical parameters of a galaxy affect its observed integrated light, and therefore can be reconstructed using the galaxy's spectrum. The model computes the spectral evolution of stellar populations across a wavelength range from 3200 to 9500 Å at a high resolution of 3 Å and across a wider wavelength range (91 Å to 160 μm) at a lower resolution based on the library of observed stellar spectra assembled by Le Borgne et al. (2003). While their model is often applied to model colors and interpret observed high-resolution galaxy spectra, I used the GALAXEV package to provide sample spectra of galaxies varying in age and SFH, chemical enrichment, and dust content. The GALAXEV spectrum of one such galaxy is shown in Figure 2.1. The range of higher resolution (3200 to 9500 Å) for the model is evident.

Beginning with the stellar spectral library of Le Borgne et al. (2003), the Bruzual & Charlot (2003) model employs a stellar evolution prescription based on an isochrone synthesis technique developed by the authors (Charlot & Bruzual, 1991; Bruzual A. & Charlot, 1993). This technique is based on the idea that a population of stars with any given SFH can be expanded in a series

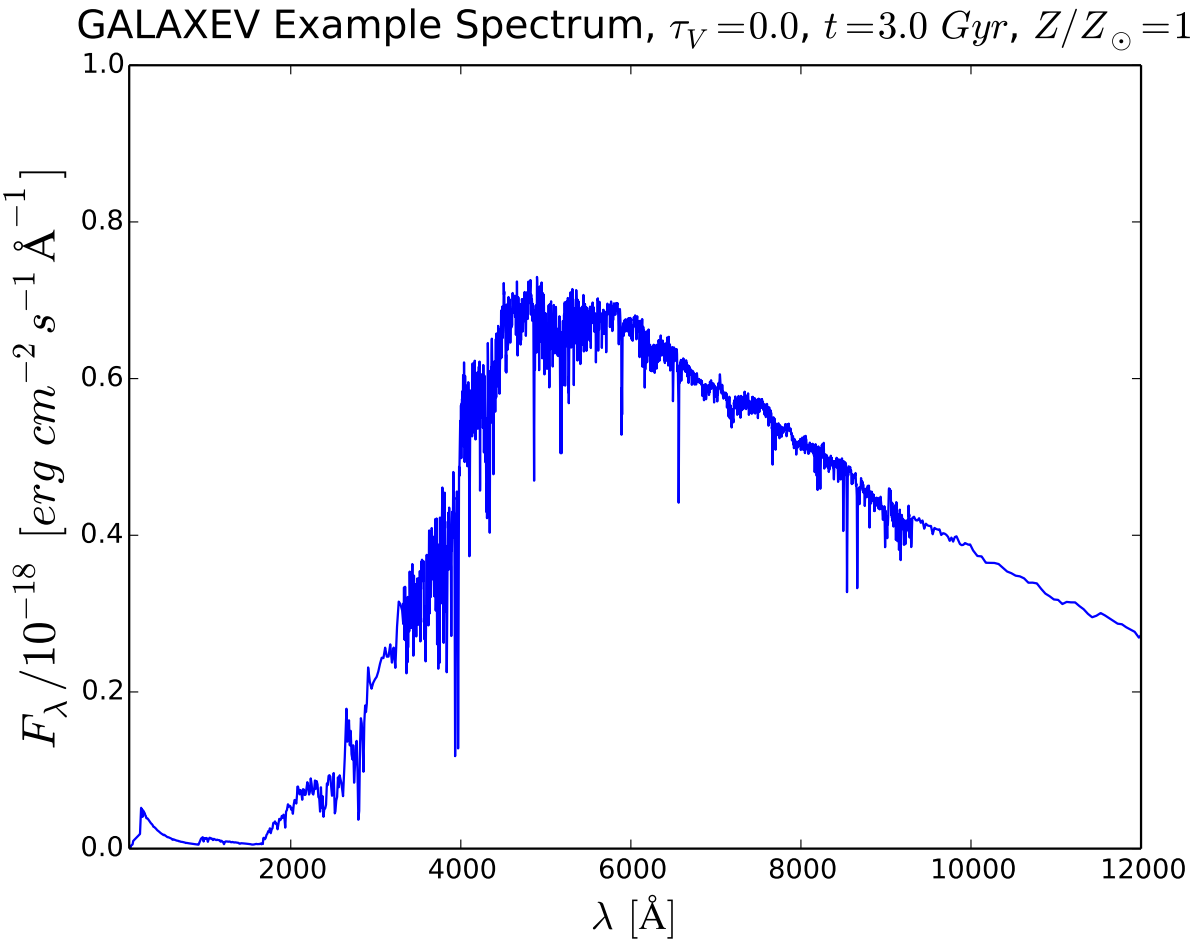

Figure 2.1: Sample Bruzual & Charlot GALAXEV spectrum for a galaxy 3.0 Gyr after the last episode of star formation, with solar metallicity and no dust extinction. The range of higher resolution (3200 to 9500 Å) can be observed in the figure.

of simple stellar populations (SSPs), which are essentially instantaneous starbursts. Assuming a time-independent initial mass function (IMF), they populate different evolutionary stages along each isochrone with stars of initial masses distributed according to the IMF. After assigning spectra to stars according to their evolutionary stages, they add the spectra of the individual stars along the isochrone to get the SSP's spectral energy distribution (SED). These SEDs are combined in accordance with the galaxy's SFH to obtain the integrated spectrum of the galaxy. The sample spectra I created for my study all assume a Chabrier (2003) IMF. This is the IMF recommended by Bruzual & Charlot (2003) because it is physically motivated and provides a better fit to the counts of low-mass stars and brown dwarfs in the Galactic disk than does a Kroupa (2001) IMF, although the difference is minor.

Attenuation of starlight by dust in the Bruzual & Charlot (2003) population synthesis model is parameterized using the physically-motivated prescription of Charlot & Fall (2000). In this process, a different effective attenuation optical depth affects stars younger than 0.01 Gyr than affects stars older than 0.01 Gyr. Optical depth here refers to the number of mean free path lengths along the line of sight; it is approximately equal to the absorption along the line of sight in magnitudes. The characteristic age of 0.01 Gyr corresponds to the typical lifetime of a giant molecular 'birth cloud'. After the giant molecular cloud disperses, the attenuation is due to the galaxy's diffuse interstellar medium. Therefore, attenuation of photons is much greater for young stellar populations than it is for older populations. The GALAXEV package accepts values of τ_V, the total effective V-band optical depth seen by young stars, to parameterize the dust content of a galaxy.

2.2 aXeSIM: The Slitless Simulation Package

To simulate WFC3 grism observations, I used the aXeSIM software package[1] (The aXe Software Package 2013). The slitless spectroscopy group of the Space Telescope European Coordinating Facility (ST-ECF) developed this PyRAF module as part of the support for the WFC3 slitless

[1] aXeSIM information and instructions for use may be found at http://axe-info.stsci.edu/.

spectroscopy modes (Kümmel, Walsh, & Kuntschner 2010).

The aXeSIM package uses the same configuration and calibration files needed for the reduction of slitless spectroscopy data with the aXe extraction software. It takes as input a list of descriptions of simulation objects, including redshifts, flux levels, and image templates, and simulates a slitless spectral image and a direct image to match the spectral image (if a total passband or filter is specified). These images are simulations of standard WFC3 slitless observations. Sky background and random noise (simply readout and photon noise from the background and other objects) can be added to the output images, as well. The simulation package does not include nonlinear detector effects, such as saturation.

Figure 2.2 shows a sample z = 1.62 galaxy template spectrum and its corresponding aXeSIM extracted spectrum, including uncertainty, at a J-band magnitude of 21.0. Similar plots obtained from observing galaxies at magnitudes of 21.6, 22.2, and 22.8 (the magnitude limit of the study) can be found in the Appendix. The corresponding direct image and slitless dispersed image for the galaxy are displayed in Figure 2.3.

2.3 Project Description

This is a feasibility study for the analysis of HST observations of a galaxy cluster at redshift z = 1.62, about 4 Gyr after the Big Bang. The goal is to determine any systematic biases in $D(4000)$ and $D_n(4000)$ and find the magnitude limit under which a measurement of $D(4000)$ is a reliable probe of a galaxy's average stellar age. Researchers are hoping to use $D(4000)$ to constrain the stellar ages of galaxies in cluster IRC 0218A (also called XMMLSS J02182-05102) and study galaxy evolution (Tran et al., 2010; Papovich et al., 2010; Rudnick et al., 2012; Lotz et al., 2013). Figure 2.4, taken from Papovich et al. (2010), gives a false-color image of the cluster.

My collaborators are performing a detailed study of galaxy evolution in IRC 0218A using HST WFC3 imaging and spectroscopy. This cluster was selected as an overdensity of galaxies at high redshift based on a *Spitzer* IRAC (infrared array camera) color selection in which both star-

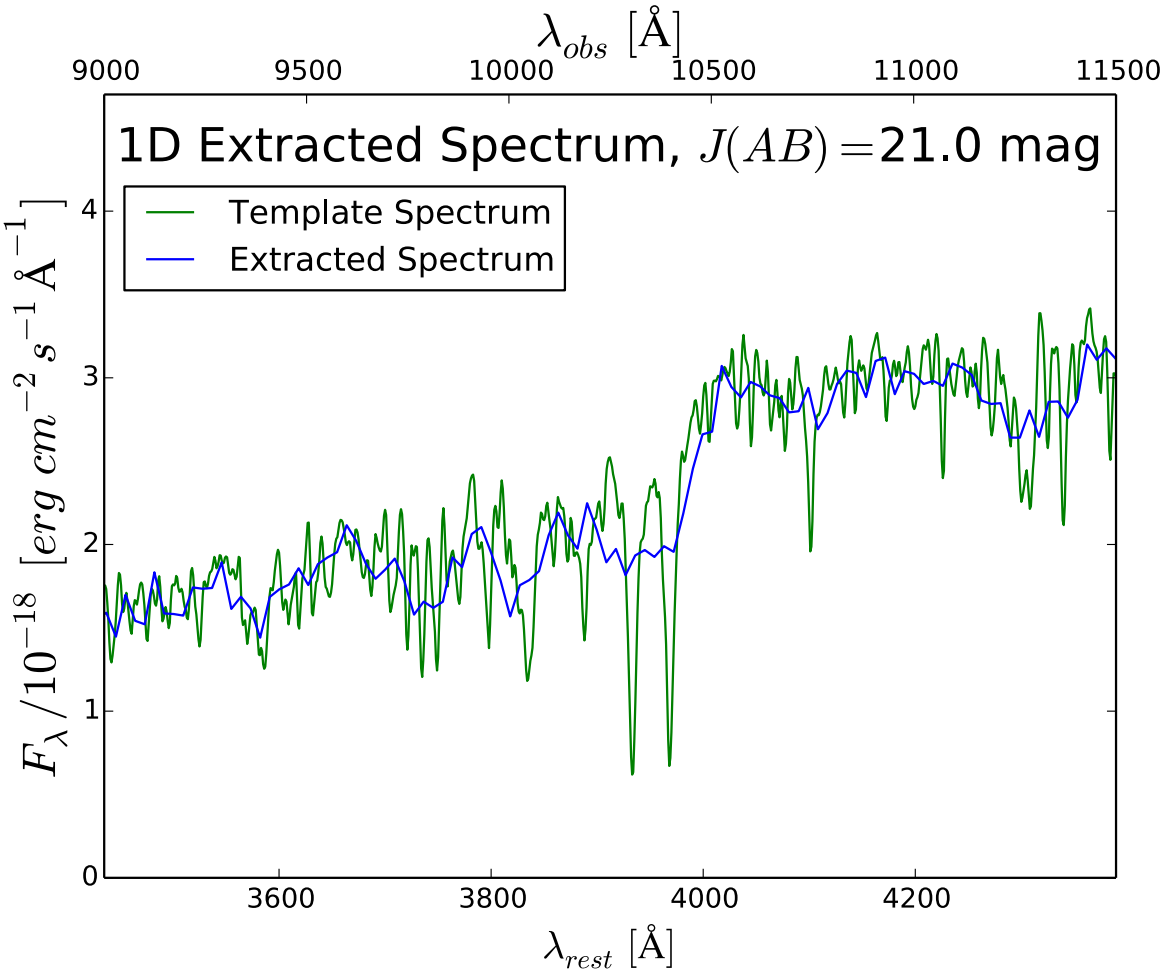

Figure 2.2: Sample galaxy template spectrum and its corresponding aXeSIM extracted spectrum for a galaxy 3.0 Gyr after the last episode of star formation, with metallicity $Z/Z_\odot = 0.2$ and no dust extinction. The green line is the intrinsic galaxy spectrum, the blue line is its aXeSIM one-dimensional extracted spectrum simulated with 10 orbits (about 28 ksec) of HST/WFC3 G102 grism spectroscopy, and the blue shaded region gives the measurement uncertainty in the extracted spectrum.

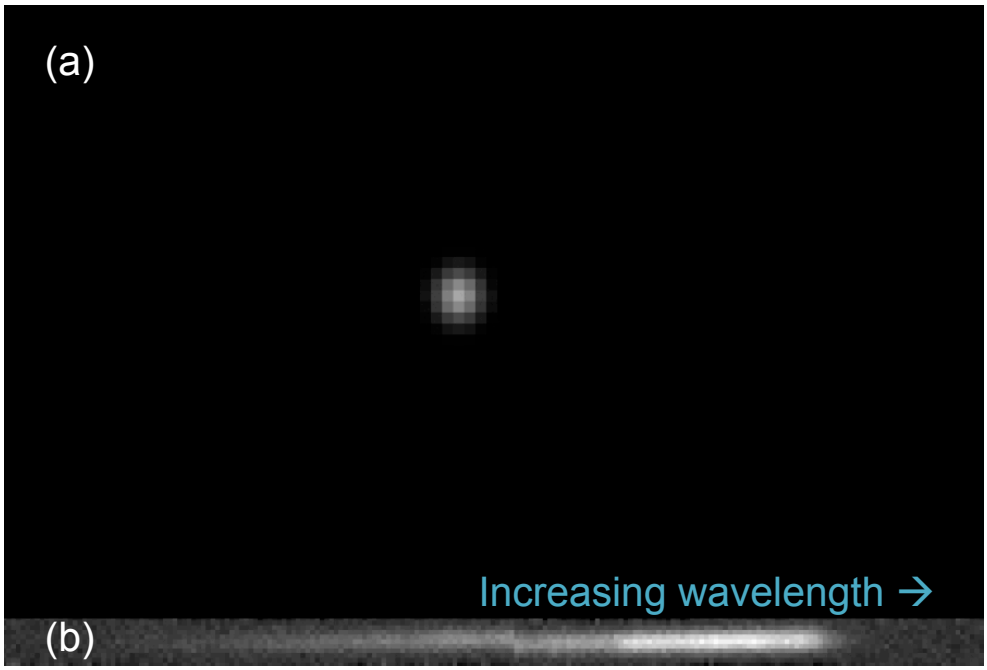

Figure 2.3: Sample galaxy direct image (a) and slitless dispersed image (b) given by aXeSIM for the same galaxy template used in Figure 2.2. Wavelength increases toward the right in the grism panel.

forming and quiescent galaxies appear red (Papovich, 2008). Although the selection process had no dependence on rest-frame color, this cluster has a strong, well-defined red sequence (Papovich et al., 2010). Interestingly, there also exists a high level of star formation in the cluster core, indicating that the massive cluster galaxies are still forming many of their stars (Tran et al., 2010).

Because it appears to still be in the process of forming, IRC 0218A is a key cluster for studies of galaxy evolution. Furthermore, the cluster conveniently offers an abundance of multiwavelength data (Tran et al., 2010; Papovich et al., 2010; Rudnick et al., 2012; Lotz et al., 2013). Using the HST WFC3 grism, my collaborators hope to measure accurate redshifts and spectral features for the red IRC 0218A galaxies out to a J-band magnitude of J(AB) = 22.8 mag, the magnitude limit of this study. The G102 grism was used because its wavelength coverage contains the 4000 Å break for galaxies at a redshift of $z \sim 1.6$. This break is evident, for example, in Figure 2.2, which shows the extracted simulated spectrum of a galaxy with J(AB) = 21.0 in a 10-orbit G102 observation.

The hope is that measuring $D(4000)$, or alternatively, $D_n(4000)$, will give a meaningful constraint on the age of each cluster galaxy's stellar population. This will allow researchers to study

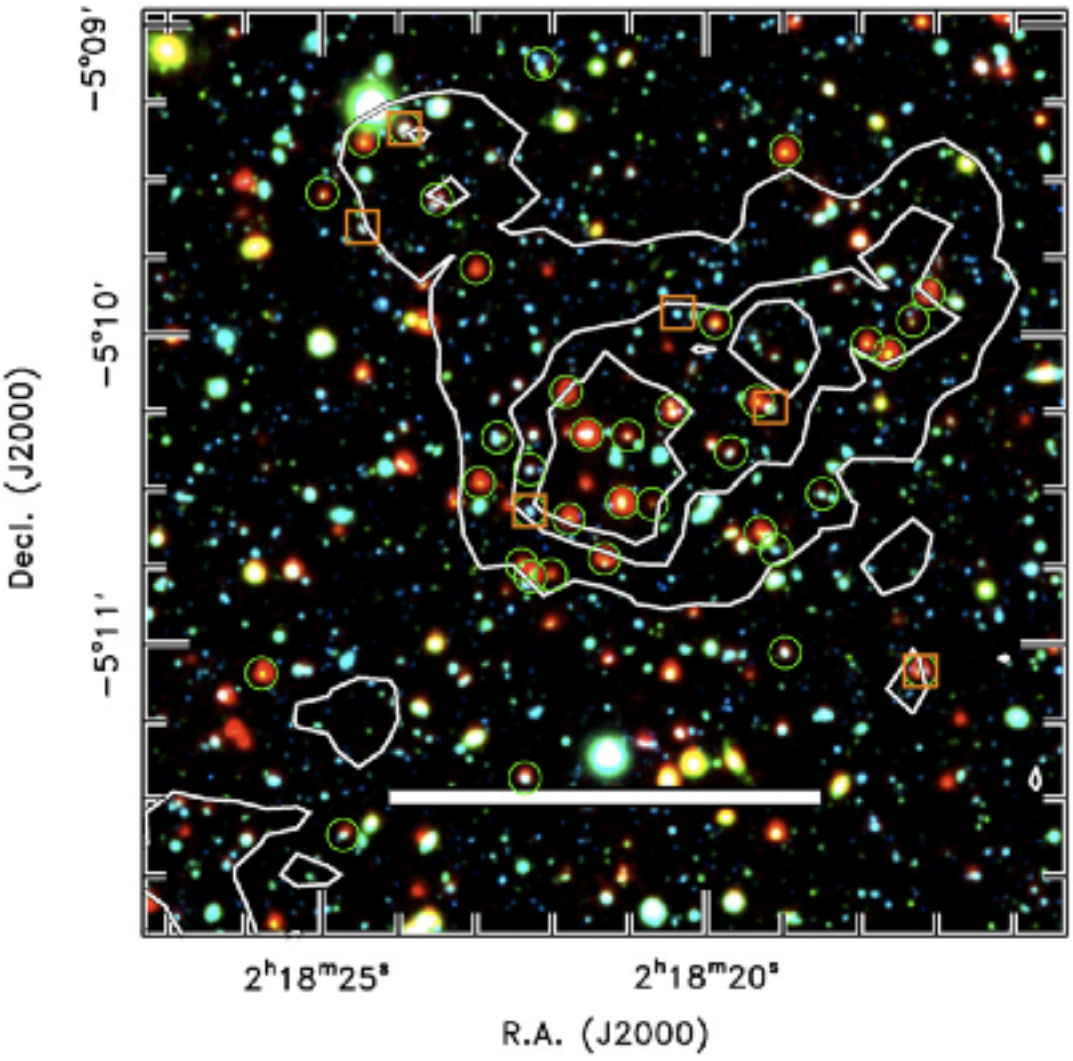

Figure 2.4: 3' × 3' false-color image of IRC 0218A (Papovich et al., 2010). This is equivalent to 1.5 Mpc × 1.5 Mpc at z = 1.62. Blue corresponds to the Suprime-Cam *B* band, green to the Suprime-Cam *i* band, and red to the *Spitzer* 4.5 μm band. The white bar shows a distance of 0.7 Mpc at z = 1.62.

how the average stellar age in these galaxies varies as a function of other galaxy properties such as mass, dust, and location in the cluster. Comparing these trends to those of nearby galaxies and to high-redshift field galaxies will provide valuable science, if $D(4000)$ is indeed a reliable measure of stellar population age at a redshift of z = 1.62. For example, a correlation between stellar population age and stellar mass has been observed for nearby galaxies (e.g., Gallazzi et al., 2005; Mateus et al., 2006). Do galaxies follow the same trend in such high-redshift clusters as IRC 0218A? Do field galaxies at that redshift follow a different relation? Do star forming galaxies in the cluster environment exhibit a similar correlation? These are all questions that can be tackled by the HST analysis of this cluster. Ultimately, this work could also contribute to the determination of whether massive galaxies stop star formation for different reasons than low-mass galaxies.

This feasibility study serves to check for systematic biases in $D(4000)$ and $D_n(4000)$ and determine down to what magnitude a $D(4000)$ measurement is reasonably precise at a redshift of z $\sim$ 1.6 using HST's WFC3/G102L infrared grism so that researchers can begin to answer the above questions. Although most galaxy studies exclusively use $D_n(4000)$ as of this writing because it is less susceptible to dust extinction, the lower signal-to-noise inherent in the measurement may prove to be a substantial disadvantage at these magnitudes. A grid of model galaxies was constructed using the GALAXEV package by varying several parameters: the metallicity, dust extinction, and a time parameter that folds in star formation history (SFH) and age. Two metallicities covering a wide range were considered: $Z/Z_{\odot} = 0.2$ and $Z/Z_{\odot} = 1.0$. Since the GALAXEV model does not include recycling, all stars form at that metallicity. Dust extinction was parameterized by τ_V, the total effective V-band optical depth seen by young stars according to the simple prescription of Charlot & Fall (2000). The birth cloud optical depths considered were τ_V = 0.0, τ_V = 1.0, τ_V = 2.0, and τ_V = 3.0. The time parameter is slightly more involved. All galaxies in the grid of models were formed at z $\sim$ 9 and were given one continuous burst of star formation during which stars form at a constant rate for a set amount of time varying from 0.5 to 3.5 Gyr, when star formation is abruptly dropped to zero. Each galaxy was then permitted to evolve passively until 3.5 Gyr after star formation began, at which time the spectrum was "observed" at z = 1.62 using aXeSIM. The

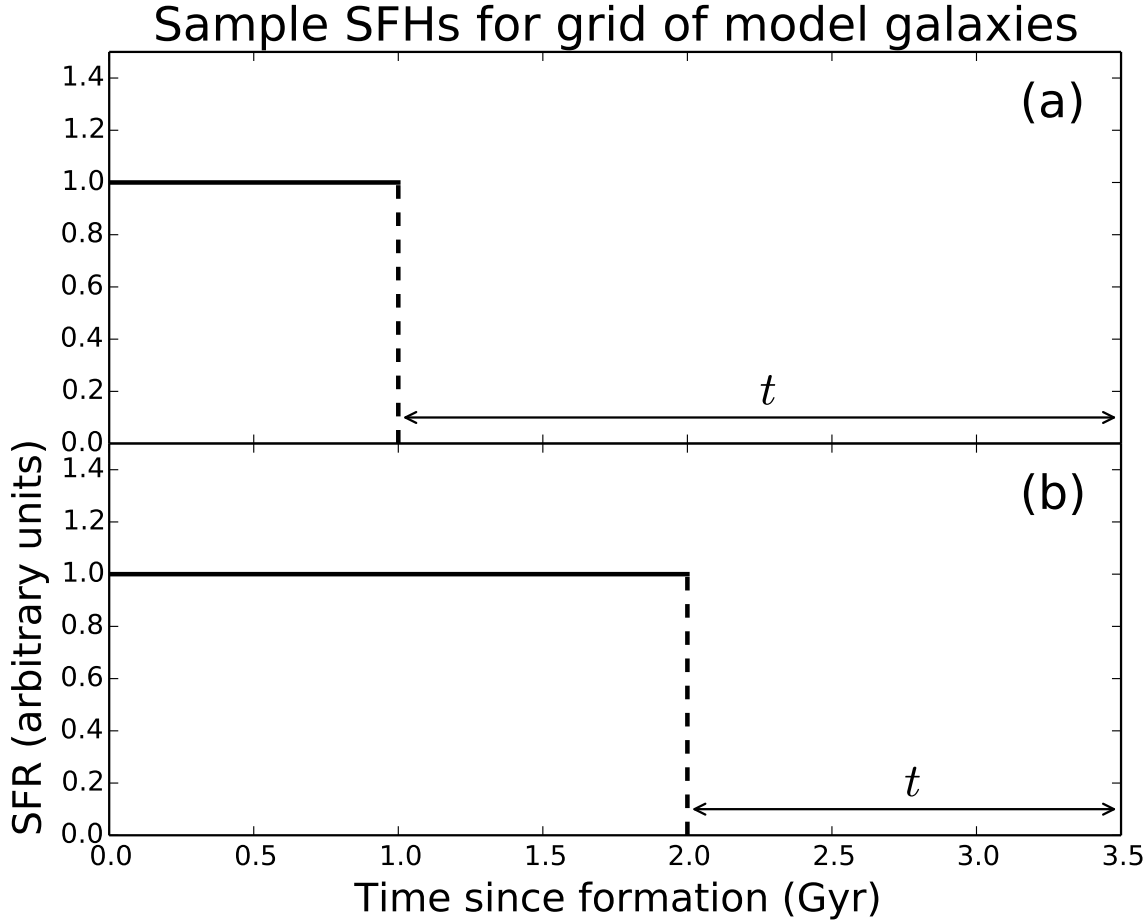

Figure 2.5: Simple schematic of sample SFHs considered in the grid of template galaxies, with the t parameter labelled. A 1 Gyr burst of star formation, corresponding to $t = 2.5$ Gyr, is given in (a); a 2 Gyr burst of star formation, corresponding to $t = 1.5$ Gyr, is shown in (b).

variable t, which gives the time between star formation ending and the observation, in this way combines SFH and stellar population age. Figure 2.5 shows a simple schematic of the t parameter for clarification.

A range of galaxy magnitudes in the cluster is of course expected, so the magnitude of the galaxies simulated was also varied. To match the actual observations, aXeSIM was used to simulate observations of galaxies at z = 1.62 with 10 orbits (about 28 ksec) of HST/WFC3 G102 grism spectroscopy. The magnitudes I considered varied from J(AB) = 21.0 mag to the study's magnitude limit of J(AB) = 22.8 mag. Varying each of the parameters separately gives a total of 224 unique simulated galaxies to analyze.

Armed with this grid of model galaxies, I calculated the strength of the 4000 Å break for each galaxy and compared the results to the $D(4000)$ and $D_n(4000)$ measurements for the extracted spectra obtained using aXeSIM. My aim was to determine whether $D(4000)$ or $D_n(4000)$ includes less systematic biases and whether this could be described as a function of stellar age, dust extinction, metallicity, or magnitude.

Chapter 3

Results

3.1 Model Galaxy Spectra

The GALAXEV spectra for all galaxies in the grid of models were first plotted and normalized to 22.8 mag at 1250 nm, corresponding to the J-band magnitude limit of the study, and any differences in the spectra were noted. Figure 3.1 shows trends in metallicity, using $Z/Z_{\odot} = 0.2$ and $Z/Z_{\odot} = 1.0$. For illustration purposes, only the spectra of a young ($t = 0.0$ Gyr) and an old ($t = 3.0$ Gyr) model galaxy with $\tau_V = 0$ are shown in the figure. The plots corresponding to all optical depths and ages can be found in the Appendix. In all cases, there is very little difference in the spectra for $Z/Z_{\odot} = 0.2$ and $Z/Z_{\odot} = 1.0$. Each $Z/Z_{\odot} = 1.0$ spectrum clearly shows a larger 4000 Å break than its corresponding $Z/Z_{\odot} = 0.2$ spectrum, and this result holds for all values of τ_V. This makes sense; metal absorption lines are responsible for the 4000 Å break, so a galaxy containing more metal-rich stars should show a stronger 4000 Å break in its spectrum. We expect the differences between $Z/Z_{\odot} = 0.2$ and $Z/Z_{\odot} = 1.0$ galaxy spectra to increase with increasing age because over time, a galaxy's spectrum becomes less dominated by hot, massive stars with ionized metals (and therefore no metal absorption lines) and becomes more dominated by cool stars with noticeable metal lines. Figure 3.1 does illustrate this trend.

Next, the entire grid of model galaxies was run through aXeSIM. A direct image, grism dis-

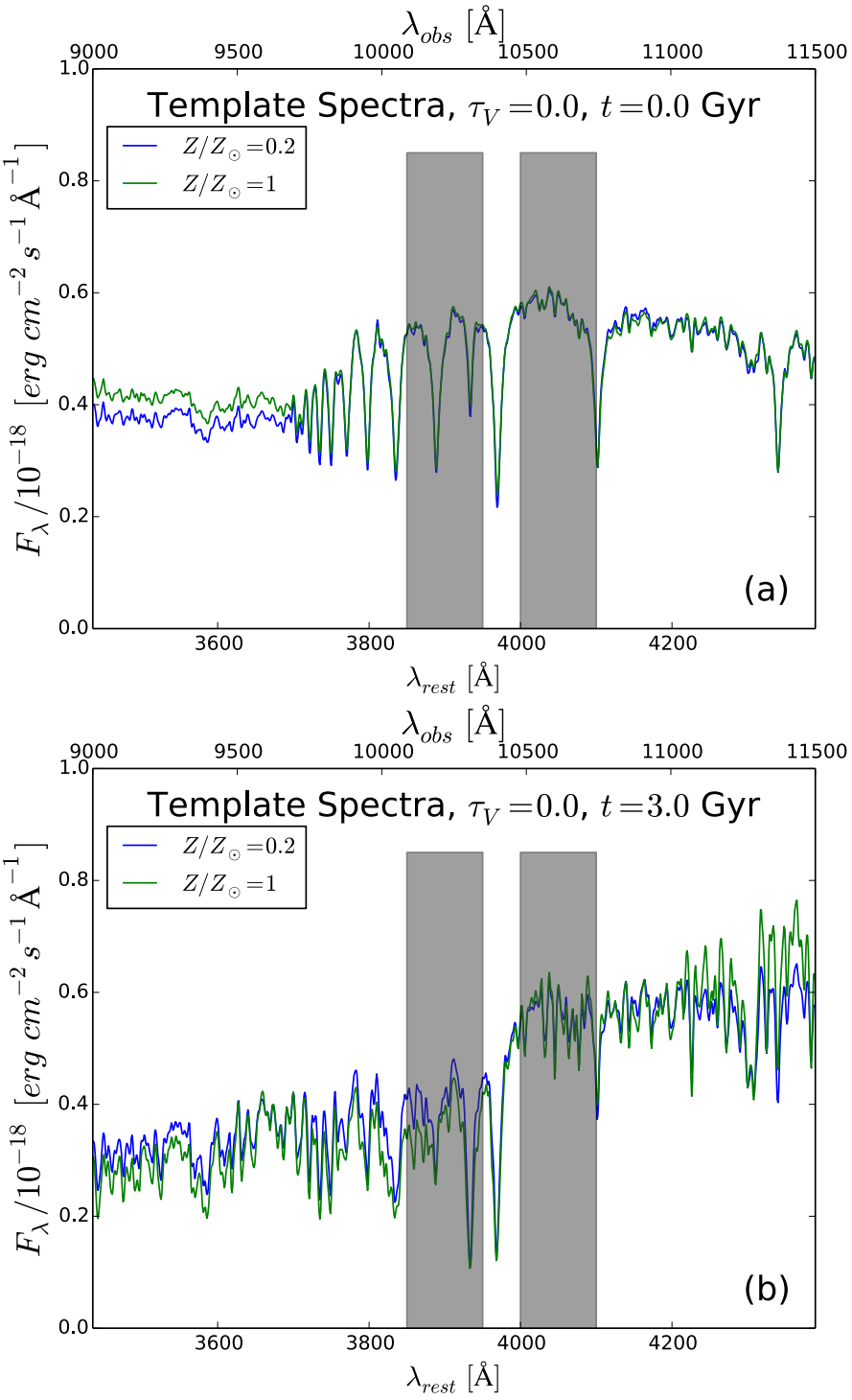

Figure 3.1: Bruzual & Charlot GALAXEV spectra, normalized at an observed wavelength of 1250 nm, for several galaxies in the grid of templates with no dust extinction. The effect of metallicity Z on a galaxy's spectrum is being investigated. Although differences between $Z/Z_\odot = 0.2$ and $Z/Z_\odot = 1.0$ are minor, these differences generally increase with average stellar age, and galaxies with higher metallicity exhibit stronger 4000 Å breaks. Gray shaded regions mark the $D_n(4000)$ wavelength ranges. The two plots correspond to values of t: (a) $t = 0.0$ Gyr, and (b) $t = 3.0$ Gyr.

persed image, and one-dimensional extracted spectrum was simulated for all 224 combinations of magnitude, metallicity, dust, and stellar age/SFH. Figure 3.2 shows the aXeSIM extracted spectra of the same template galaxies displayed in Figure 3.1, 'observed' at a J-band magnitude of 21.0. Again, only these four galaxies are shown for simplicity; the remaining plots can be found in the Appendix. At this brightness, the $Z/Z_{\odot} = 1.0$ extracted spectra clearly have a larger 4000 Å break than the $Z/Z_{\odot} = 0.2$ spectra, as observed in the galaxy templates. The very minor differences between spectra at the two metal abundances become more pronounced with increasing age.

Plots similar to those shown in Figure 3.1 explore the effect of attenuation optical depth on GALAXEV galaxy spectra (see Figure 3.3). It is clear that the effect of changing τ_V is extremely small. Varying the dust extinction has by far the largest effect on the spectra at $t = 0.0$ Gyr, but there is almost no difference in the spectra due to extinction once the giant molecular birth clouds disperse 0.01 Gyr after star formation ends. In fact, the birth clouds disperse quickly enough that there is very little effect on $D(4000)$ even at $t = 0.0$ Gyr. For simplicity, only the spectra of a few galaxies with solar metallicity are shown here; the remaining plots can be found in the Appendix.

The aXeSIM extracted spectra of the same template galaxies shown in Figure 3.3, again simulated at $J(AB) = 21.0$ mag, can be found in Figure 3.4. See the Appendix for more plots showing the effect of varying τ_V in aXeSIM spectra. As was the case with the Bruzual & Charlot template galaxies, there are very small observable differences between the galaxy spectra corresponding to $\tau_V = 0.0$ and $\tau_V = 3.0$ at $t = 0.0$ Gyr, but by $t = 3.0$ Gyr these differences have all but vanished.

By far the most influential parameter on a galaxy's intrinsic spectrum is t, which intertwines SFH and average stellar age. Figure 3.5 illustrates the effect of varying t on GALAXEV galaxy spectra. Plots corresponding to all extinctions can be found in the Appendix; only those galaxies with no dust extinction are shown in this figure. For the simple SFHs I gave the galaxies in the grid of models, it makes sense that $D(4000)$ increases with increasing t, since stellar age is precisely what $D(4000)$ is expected to constrain. The largest jump in $D(4000)$ occurs between the $t = 0.0$ Gyr spectrum and the $t = 0.5$ Gyr spectrum because most of the hot, massive stars containing ionized metals die in this time frame. At $t = 0.0$ Gyr, galaxy spectra are still dominated by light

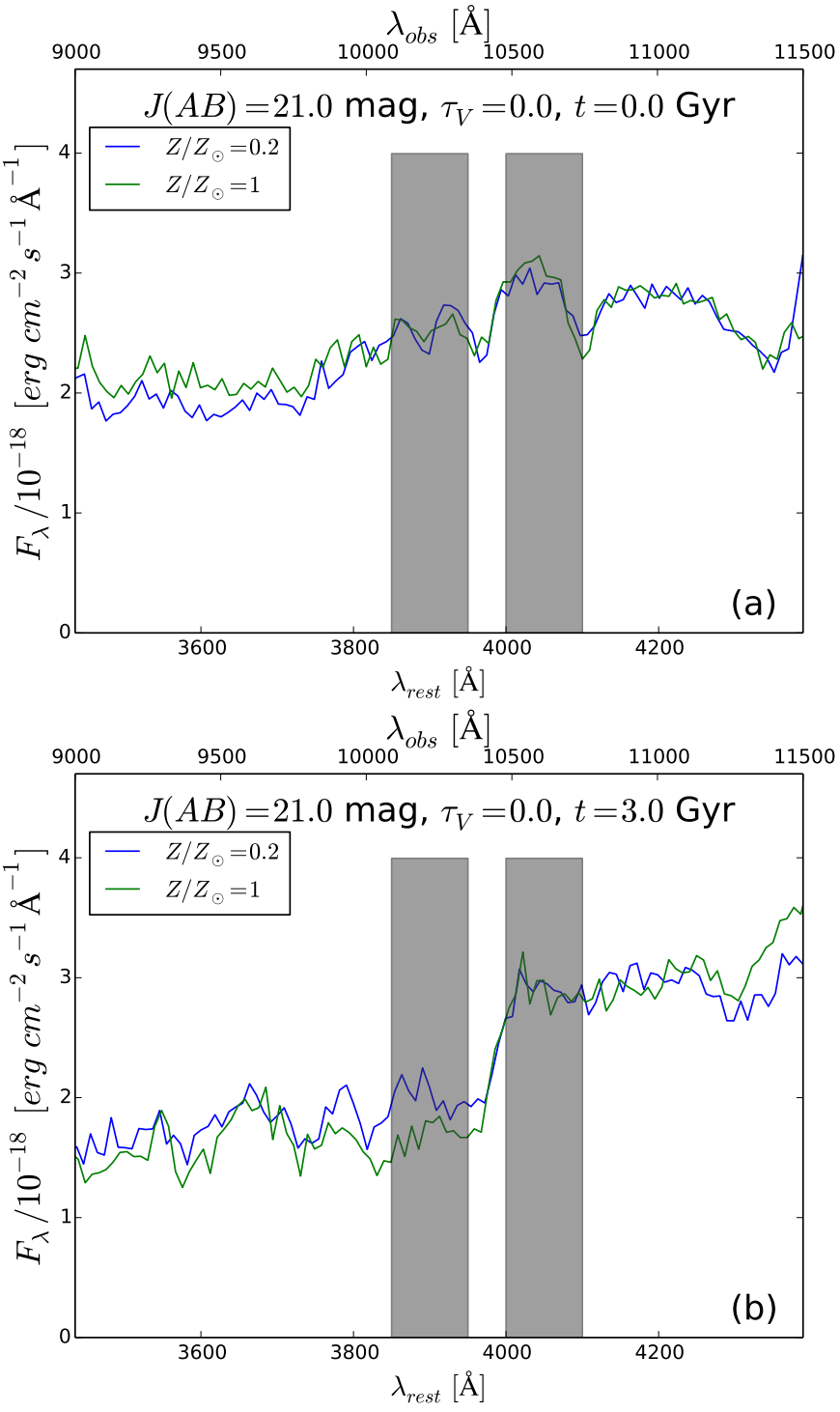

Figure 3.2: Extracted aXeSIM spectra, normalized at an observed wavelength of 1250 nm, for a 10-orbit HST observation for the same galaxies presented in Figure 3.1. The small effect of metallicity Z on a galaxy's spectrum can be observed. Although differences between $Z/Z_\odot = 0.2$ and $Z/Z_\odot = 1.0$ are minor, these differences generally increase with average stellar age, and galaxies with higher metallicity exhibit stronger 4000 Å breaks. Gray shaded regions mark the $D_n(4000)$ wavelength ranges. The two plots correspond to values of t: (a) $t = 0.0$ Gyr, and (b) $t = 3.0$ Gyr.

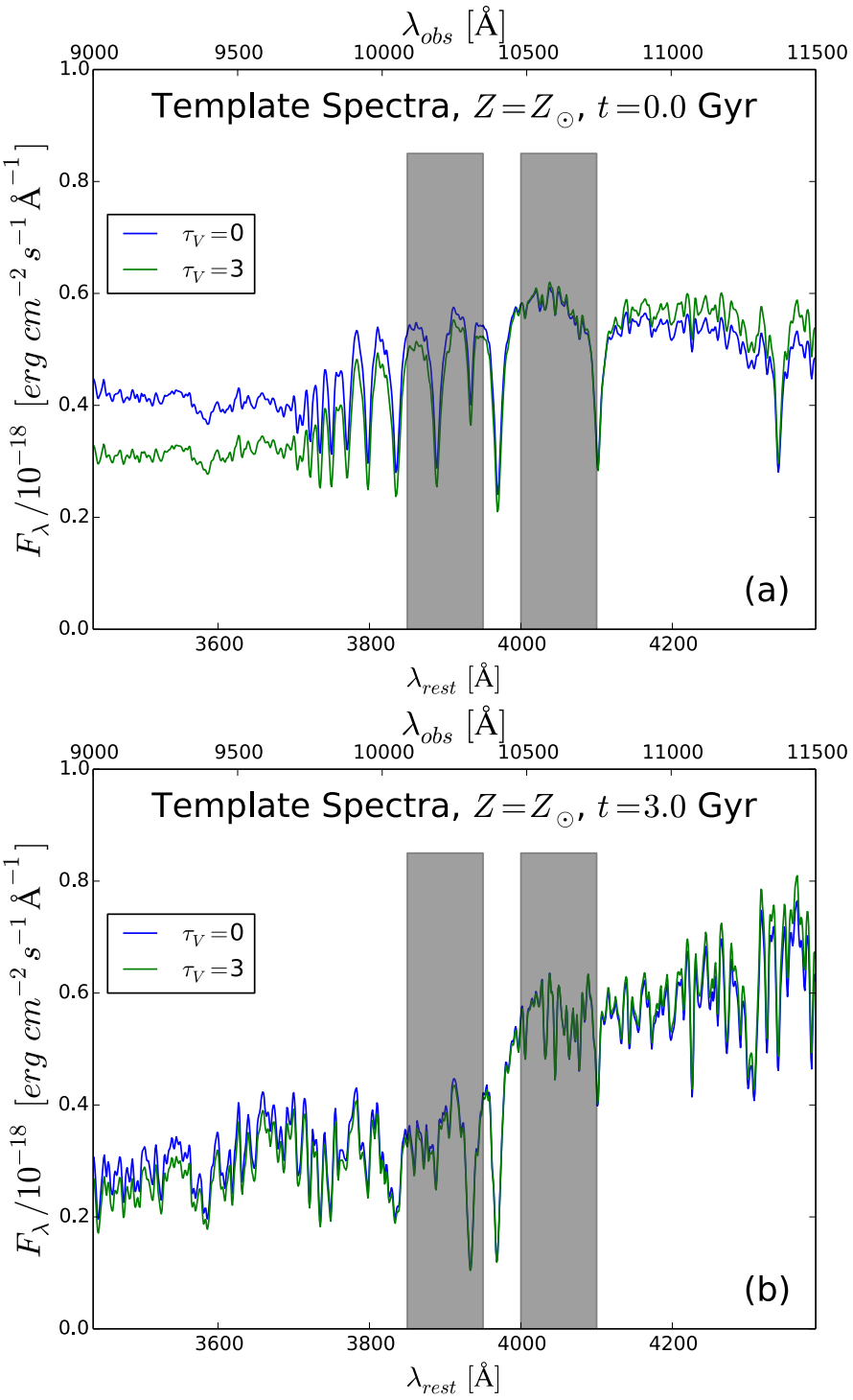

Figure 3.3: Bruzual & Charlot GALAXEV spectra, normalized at an observed wavelength of 1250 nm, for several galaxies in the grid of templates with solar metallicity. The effect of dust extinction on a galaxy's spectrum is being investigated. Higher values of τ_V correspond to more extinction by dust. After the giant molecular birth clouds disperse 0.01 Gyr after star formation ends, the minor spectral differences caused by τ_V virtually disappear. Gray shaded regions mark the $D_n(4000)$ wavelength ranges. The two plots correspond to values of t: (a) $t = 0.0$ Gyr, and (b) $t = 3.0$ Gyr.

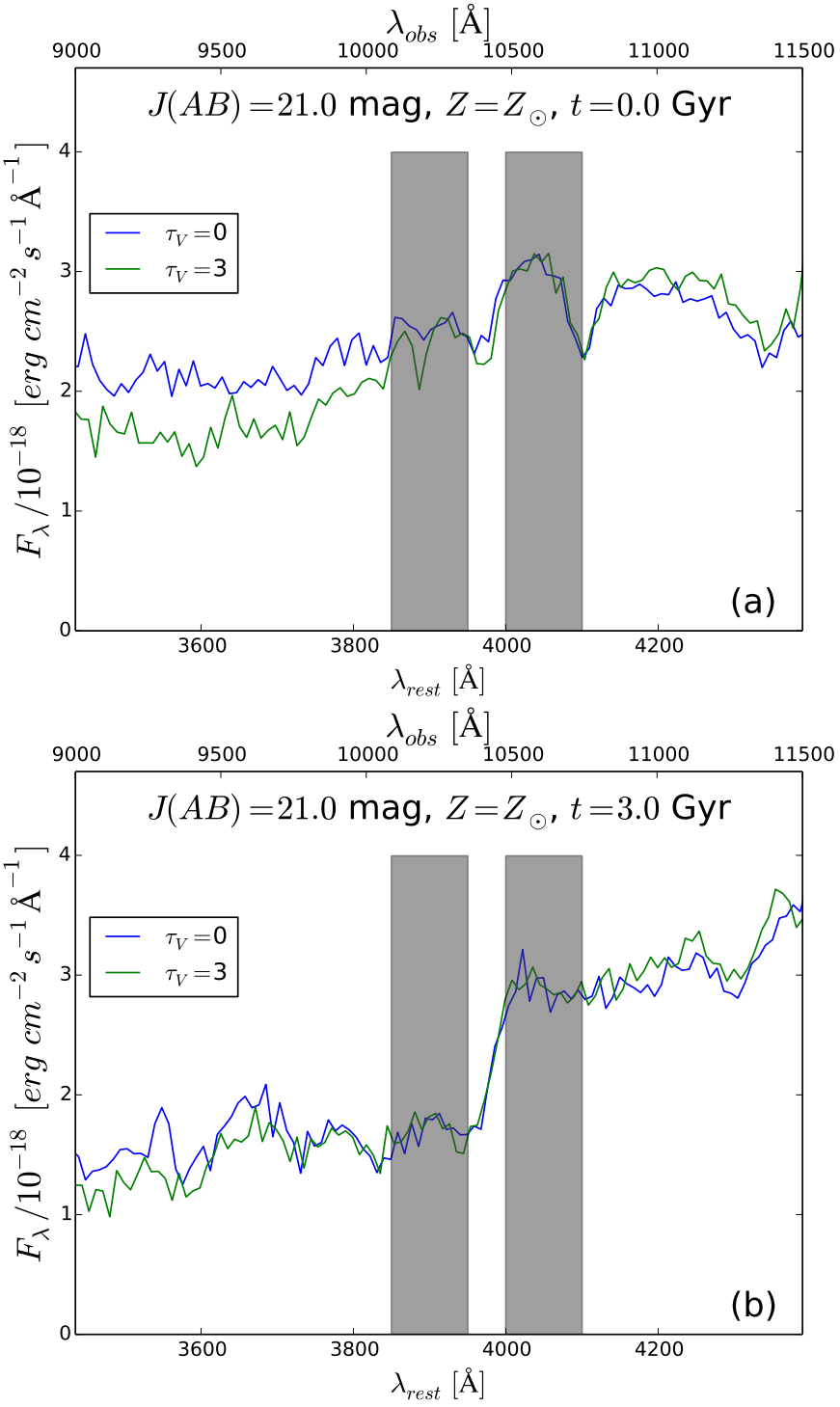

Figure 3.4: Extracted aXeSIM spectra, normalized at an observed wavelength of 1250 nm, for a 10-orbit HST observation for the same galaxies presented in Figure 3.3. The extremely small effect on a galaxy's spectrum of varying τ_V can be observed at $t = 0.0$ Gyr, but there appear to be no obvious differences at $t = 3.0$ Gyr. Gray shaded regions mark the $D_n(4000)$ wavelength ranges. The two plots correspond to values of t: (a) $t = 0.0$ Gyr, and (b) $t = 3.0$ Gyr.

from these massive stars with few metal absorption lines, and $D(4000)$ is small. The strength of the 4000 Å break increases dramatically by $t = 0.5$ Gyr, when cool, less massive stars with strong metal lines in their spectra have come to dominate the integrated galaxy spectra. This trend is visible in Figure 3.5 at both metallicities.

Figure 3.6 shows the one-dimensional extracted spectra corresponding to the galaxy templates displayed in Figure 3.5, 'observed' at a J-band magnitude of 21.0. Plots showing the remaining extinction values can be found in the Appendix. At this magnitude, rough changes in the strength of the 4000 Å break with increasing t can be seen, especially between the $t = 0.0$ Gyr spectrum and the $t = 0.5$ Gyr spectrum, where the largest jump in the template spectra also occurs.

3.2 $D(4000)$ Measurements

Once all GALAXEV template spectra and aXeSIM one-dimensional extracted spectra for my grid of template galaxies were obtained, I measured the strength of the 4000 Å break for each of them using both $D(4000)$ and $D_n(4000)$. For the SFHs I specified in the model galaxies, both indices should increase monotonically with age. This is true for part (a) of Figure 3.7, which shows the actual $D(4000)$ and $D_n(4000)$ values for galaxies with $Z/Z_\odot = 1.0$ and $\tau_V = 0$. Since in general the galaxy spectra exhibit increasing flux toward larger wavelengths near the 4000 Å break, the $D(4000)$ measurement is consistently higher than $D_n(4000)$. This relation holds at all four magnitudes I used, shown in parts (b) through (e) of Figure 3.7. It is clear from this figure that although we still see a general increasing trend at each magnitude, even at a brightness of 21.0 mag the $D(4000)$ and $D_n(4000)$ measurements are not monotonically increasing due to random error in the observations. This is likely a unique result to each particular aXeSIM 'observation' and we can expect the dips in the measured $D(4000)$ versus t plots to occur at different t values in subsequent simulations.

It is interesting to look at trends of the intrinsic $D(4000)$ and $D_n(4000)$ values for galaxies with different metallicities and dust extinctions. Figure 3.8 gives the $D(4000)$ and $D_n(4000)$ measure-

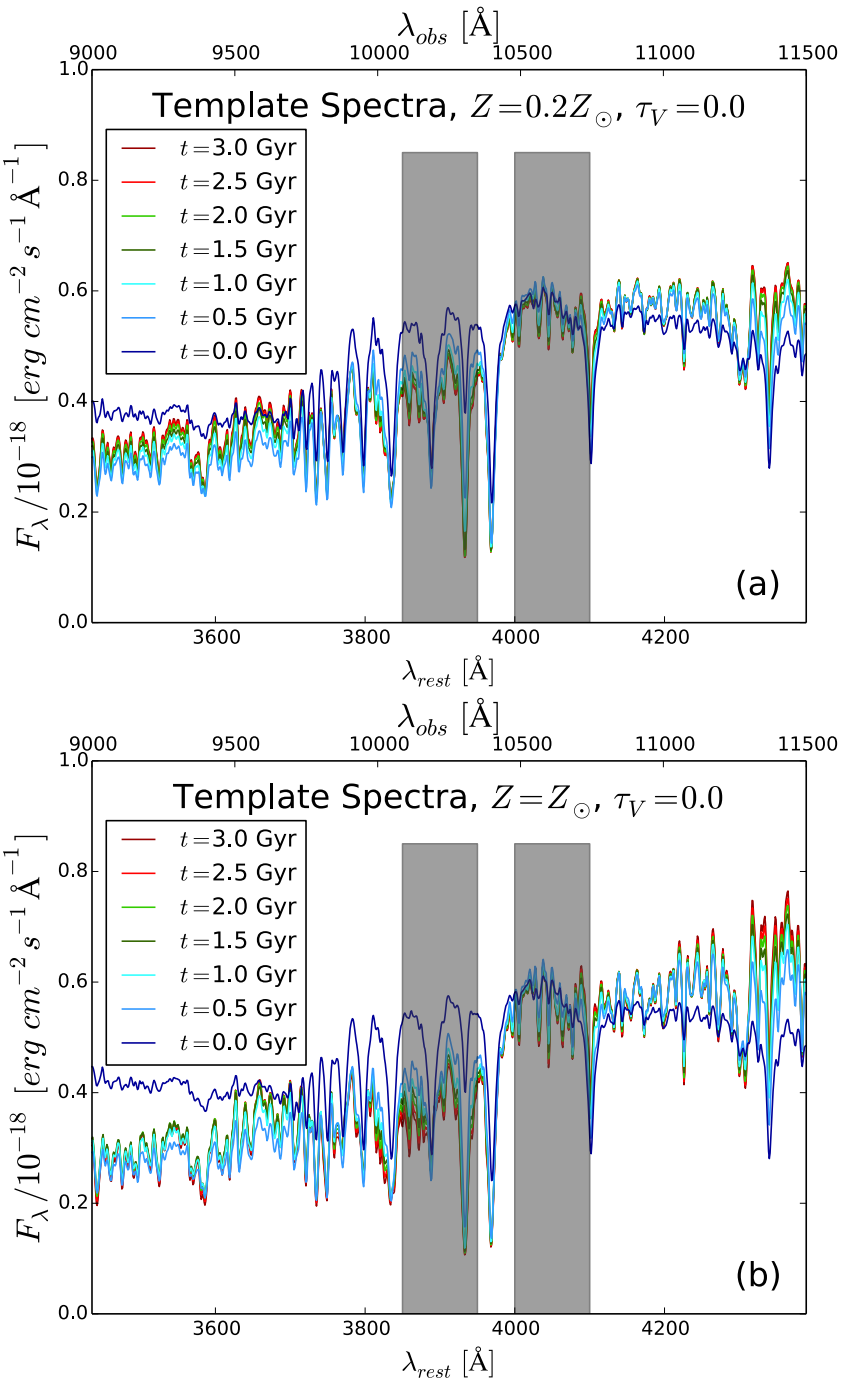

Figure 3.5: Bruzual & Charlot GALAXEV spectra, normalized at an observed wavelength of 1250 nm, for all galaxies in the grid of models with no dust extinction. The effect on a galaxy's spectrum of varying my t parameter is being investigated. Higher values of t correspond to a shorter period of constant star formation and a longer elapsed time since star formation ended. It is evident that the strength of the 4000 Å break increases with increasing t, with the largest jump occurring between the $t = 0.0$ Gyr spectrum and the $t = 0.5$ Gyr spectrum. Gray shaded regions mark the $D_n(4000)$ wavelength ranges. The two plots correspond to different metal abundances: (a) $Z/Z_\odot = 0.2$, and (b) $Z/Z_\odot = 1.0$.

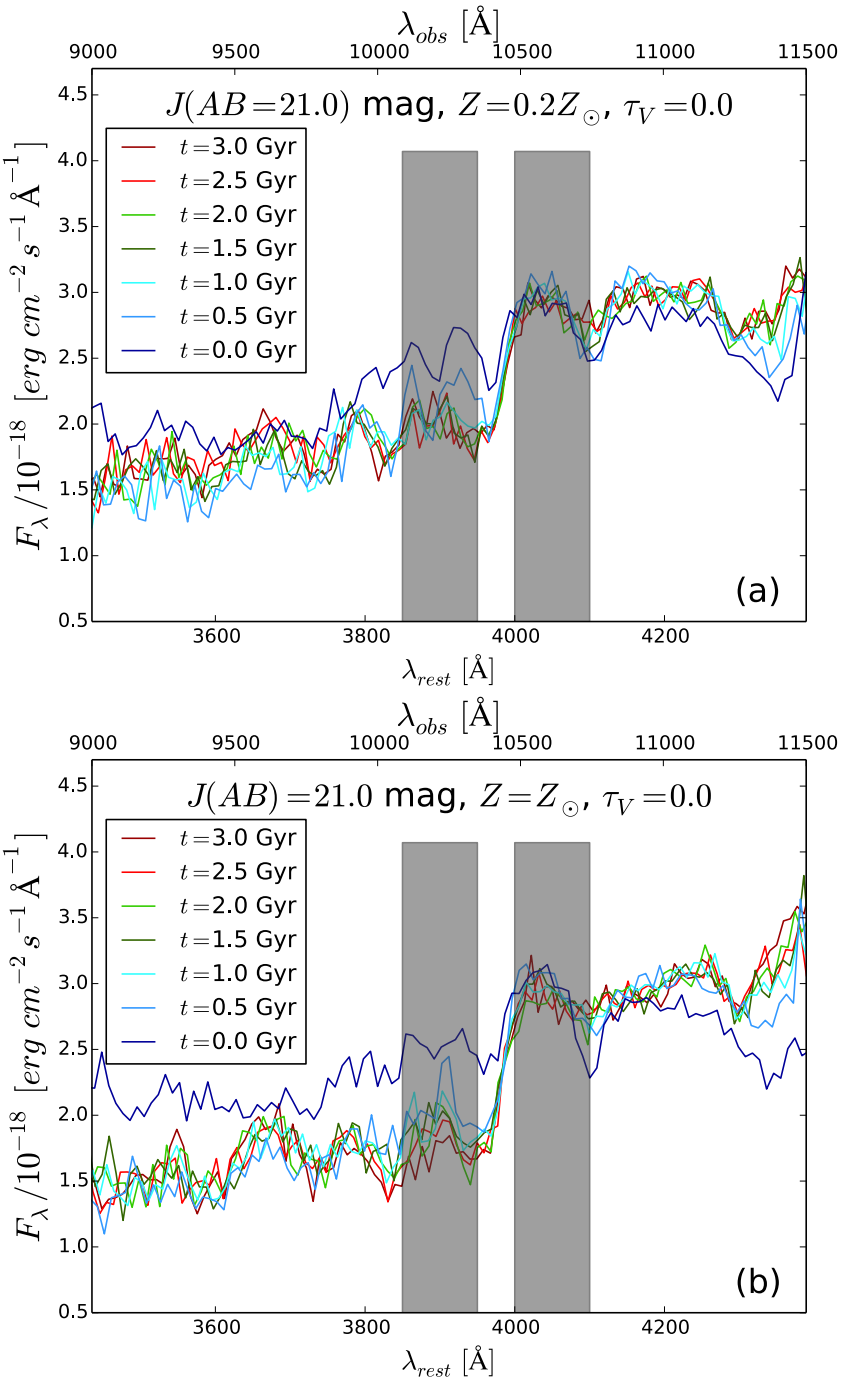

Figure 3.6: Extracted aXeSIM spectra, normalized at an observed wavelength of 1250 nm, for a 10-orbit HST observation for all galaxies in the grid of models with no dust extinction. The noticeable effect on a galaxy's spectrum of varying my t parameter can be observed. Higher values of t correspond to a shorter period of constant star formation and a longer elapsed time since star formation ended. The largest jump in the strength of the 4000 Å break is visible between the $t = 0.0$ Gyr spectrum and the $t = 0.5$ Gyr spectrum, but $D(4000)$ and $D_n(4000)$ continue to increase as the stellar population ages. Gray shaded regions mark the $D_n(4000)$ wavelength ranges. The two plots correspond to different metal abundances: (a) $Z/Z_\odot = 0.2$, and (b) $Z/Z_\odot = 1.0$.

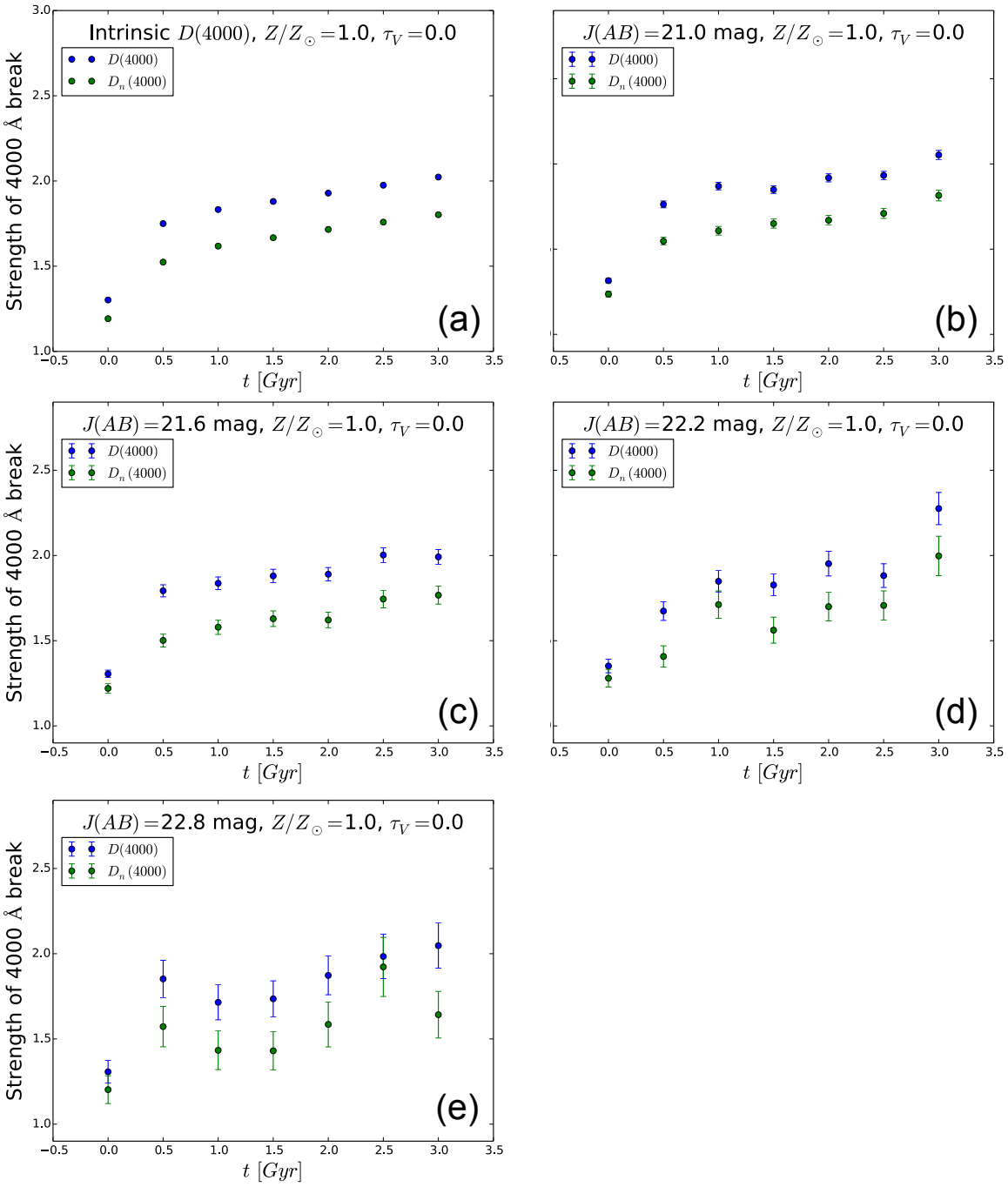

Figure 3.7: $D(4000)$ and $D_n(4000)$ measurements for galaxies with $Z/Z_\odot = 1.0$ and $\tau_V = 0$. The plots correspond to the magnitudes I used in my grid of models: (a) Bruzual & Charlot GALAXEV galaxy templates, (b) $J(AB) = 21.0$ mag, (c) $J(AB) = 21.6$ mag, (d) $J(AB) = 22.2$ mag, and (e) $J(AB) = 22.8$ mag. All simulations correspond to a 10-orbit HST observation. Due to increased random error, the accuracy and precision of the $D(4000)$ and $D_n(4000)$ measurements worsens as galaxy brightness decreases.

ment values as a function of age at all combinations of $Z/Z_{\odot}$ and τ_V. $D(4000)$ is always higher than $D_n(4000)$. Due to the reddening effect of τ_V, both $D(4000)$ and $D_n(4000)$ increase slightly with increasing dust extinction, but it is also true that $D_n(4000)$ is less affected by dust than is $D(4000)$. Both indices also increase with metallicity because the 4000 Å is, in fact, caused by a buildup of metal absorption lines prominent in cool stars just blueward of 4000 Å.

3.3 Systematic Errors

By first looking at the infinite signal-to-noise case, we can gain an understanding of potential systematic biases in the $D(4000)$ and $D_n(4000)$ measurements for the galaxy models. I compared the measured values for the two indices to their intrinsic values for each galaxy and plotted the result against the stellar population parameters Z, τ_V, and t. Some of these plots can be found in the Appendix, but a few representative figures are displayed here. Figure 3.9 is an example of $D(4000)$ and $D_n(4000)$ measurement accuracies for two galaxies identical in every way except metallicity. By exploring many similar plots, I concluded that varying metallicity has no effect on whether $D(4000)$ or $D_n(4000)$ is consistently higher or lower than the intrinsic spectrum's corresponding measurement. There is no obvious trend in metallicity that is consistent across multiple parameter sets. I performed this experiment at four different magnitudes, revealing that the measured $D(4000)$ and $D_n(4000)$ indices, with their respective systematic uncertainties, are always within 5% of the intrinsic values for J-band magnitudes of 21.6 and brighter. The $D(4000)$ and $D_n(4000)$ measurements are always within 10% of their intrinsic values for $J(AB) = 22.2$ mag and nearly always within 10% at $J(AB) = 22.8$ mag.

Figure 3.10 tells a very similar story. The four galaxies used in this illustrative plot are identical except in optical depth τ_V. As with the metallicity, there are no noticeable trends in dust extinction that remain consistent across multiple parameter sets. Varying τ_V appears to have little to no biasing effect on either $D(4000)$ or $D_n(4000)$. This is expected, since the Bruzual & Charlot galaxy template spectra were also relatively unaffected by varying τ_V.

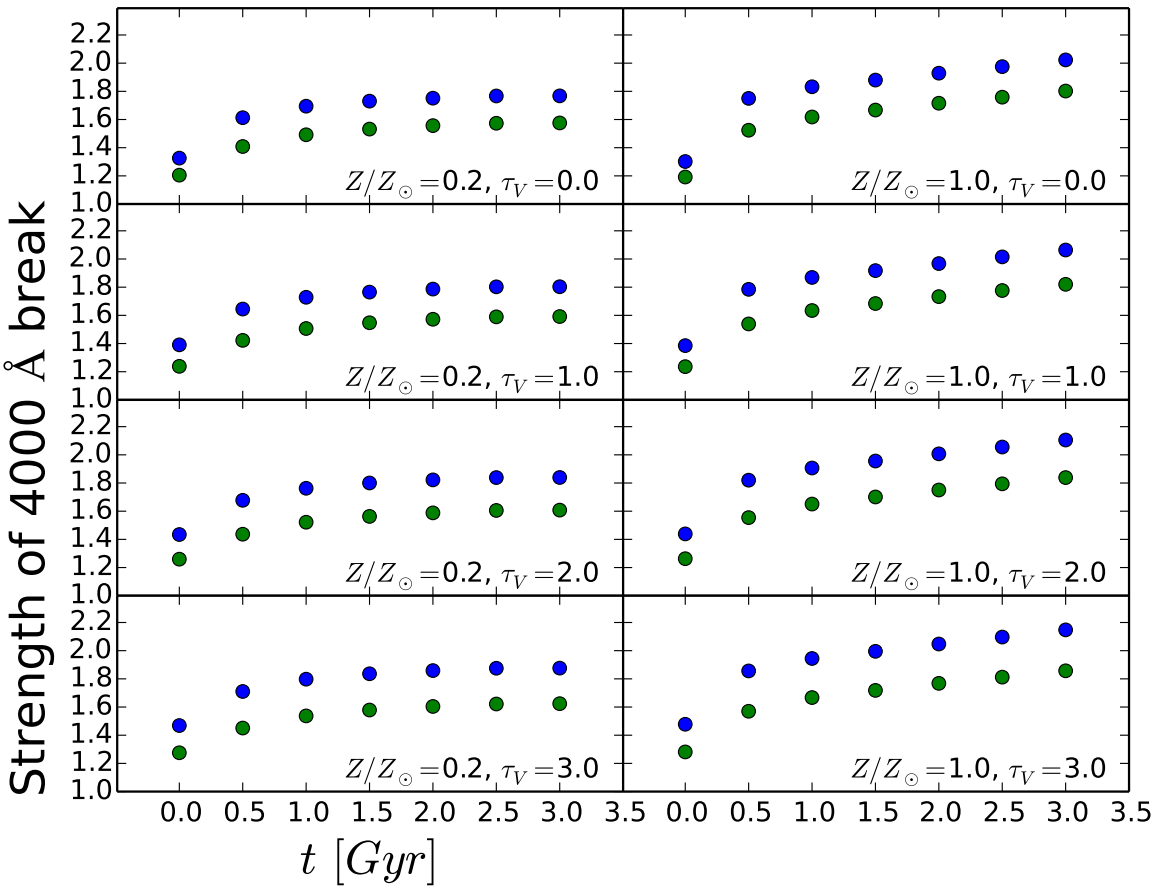

Figure 3.8: Intrinsic $D(4000)$ and $D_n(4000)$ values for all metallicities, extinctions, and t values I varied in Bruzual & Charlot's GALAXEV package to create the grid of template galaxies. The attenuation optical depth represented in the plots changes from $\tau_V = 0$ to $\tau_V = 3$ from the top to the bottom of each column, and the metallicity varies from $Z/Z_\odot = 0.2$ to $Z/Z_\odot = 1.0$ from the left to the right of each row. Each $D(4000)$ measurement is represented by a blue dot, and green dots correspond to $D_n(4000)$ measurements. Both indices increase with increasing dust extinction and metallicity. $D(4000)$ is more sensitive to dust than is $D_n(4000)$.

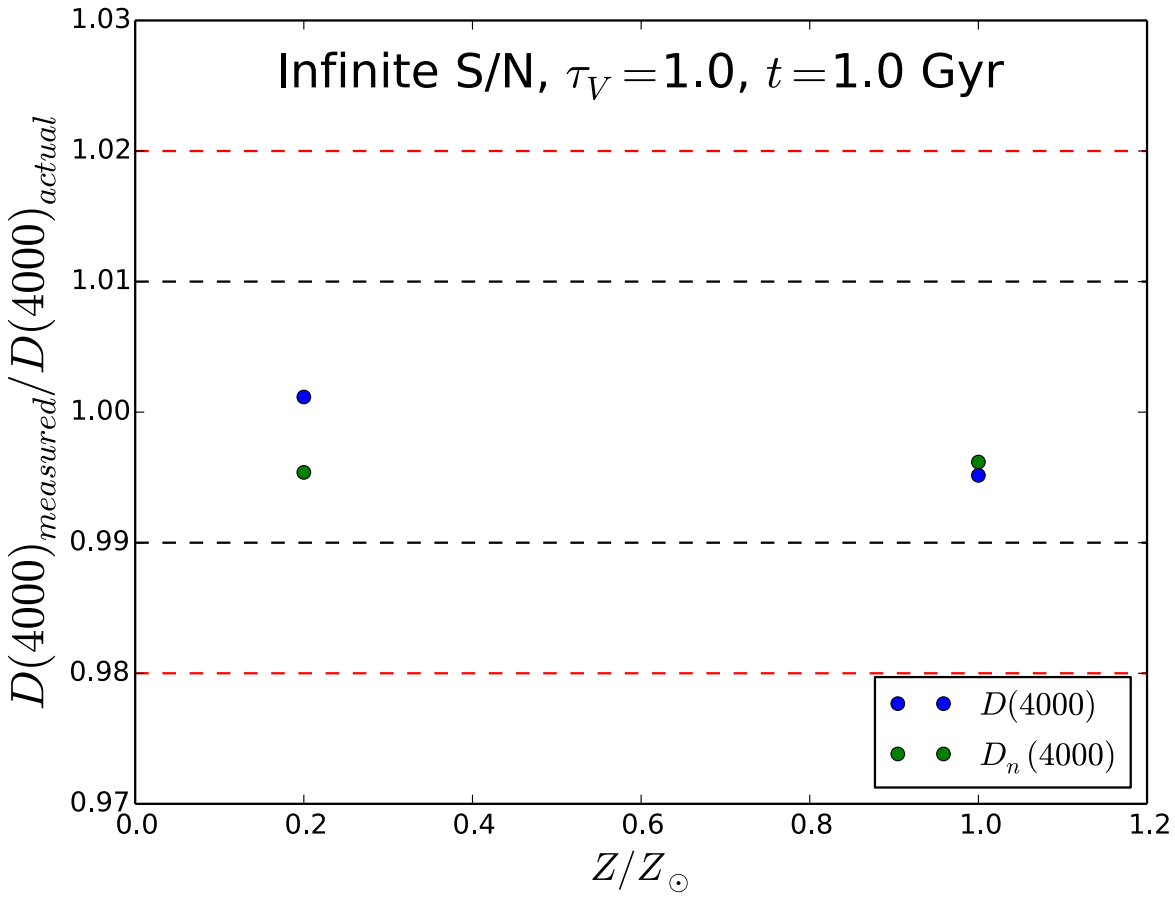

Figure 3.9: The measured $D(4000)$ (or $D_n(4000)$) value divided by the intrinsic $D(4000)$ ($D_n(4000)$) measurement for two galaxies with infinite signal-to-noise measurements, an optical depth of $\tau_V = 1.0$, and 1.0 Gyr since the abrupt end of star formation. The black dotted lines correspond to a 1% difference from unity, and the red dotted lines correspond to a 2% difference. For these template galaxies at $Z/Z_\odot = 0.2$ and $Z/Z_\odot = 1.0$, all four measurements fall within 1% of unity. There are no obvious metallicity biases in the strength of the 4000 Å break.

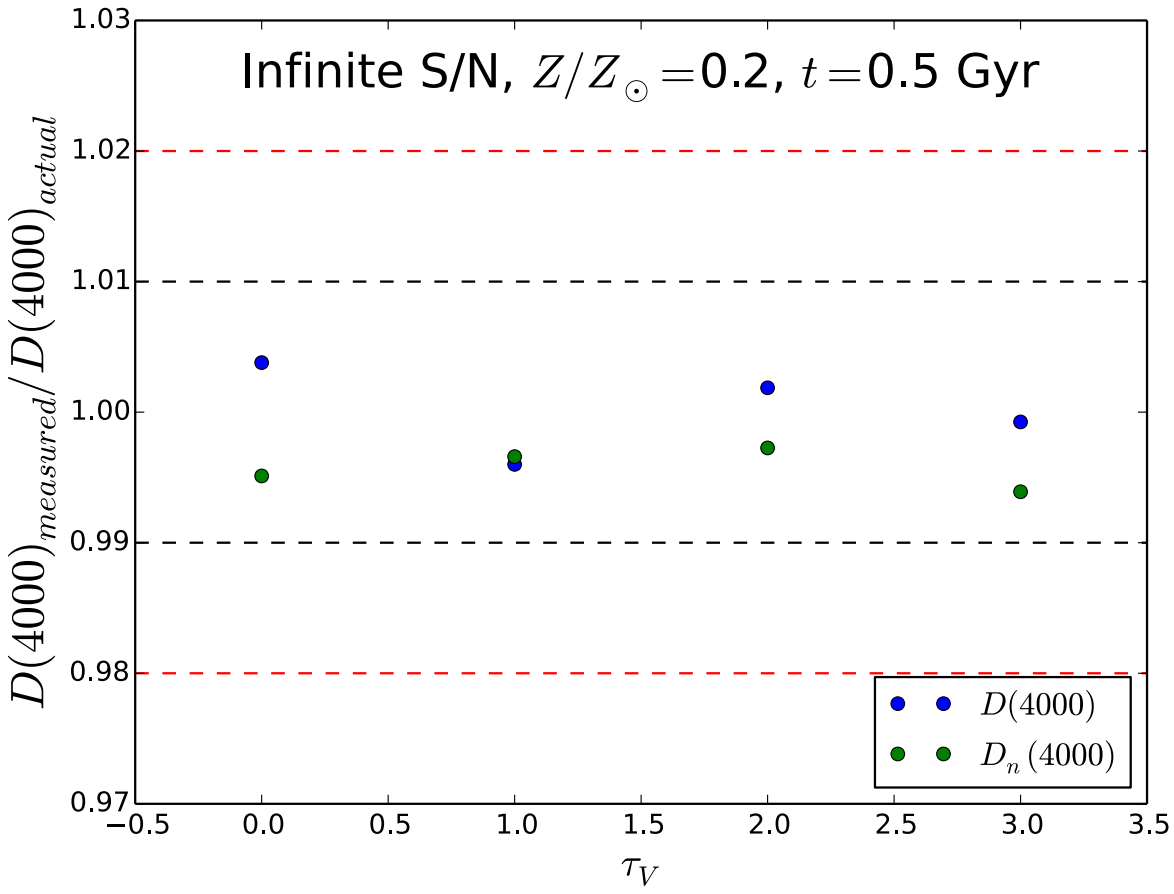

Figure 3.10: The measured $D(4000)$ (or $D_n(4000)$) value divided by the intrinsic $D(4000)$ ($D_n(4000)$) measurement for four galaxies with infinite signal-to-noise measurements, a metal abundance of $Z/Z_\odot = 0.2$, and 0.5 Gyr since star formation ended. The black dotted lines correspond to a 1% difference from unity, and the red dotted lines correspond to a 2% difference. For these four galaxies with varying levels of dust extinction, all measurements fall within 1% of unity. There appear to be no observable biases in the strength of the 4000 Å break with varying τ_V.

Potential biases of $D(4000)$ and $D_n(4000)$ with varying t were also investigated. Figure 3.11 shows one example of the plots comparing the measured $D(4000)$ index to the intrinsic $D(4000)$ index. Again, no observable patterns across multiple parameter sets appeared in the figures. Since there are no strong trends with average stellar age, as with the other parameters, there is no need to apply a correction in measuring the strength of the 4000 Å break in real cluster galaxies at z $\sim$ 1.6.

3.4 Random Errors

Random uncertainties in aXeSIM's one-dimensional extracted spectra are caused by readout and photon noise from sky background and from objects in the image. The noise corresponding to the aXeSIM observations at each magnitude can be visualized in Figure 3.12. The plots show a Bruzual & Charlot GALAXEV template spectrum, its aXeSIM extracted spectrum, and the uncertainty in the extracted spectrum at each magnitude used in this feasibility study. The brightest cluster galaxies we observe in IRC 0218A, at around $J(AB) = 21.0$ mag, have an uncertainty in flux of $\sim 5\%$ per pixel, while the faintest cluster galaxies, at the study's magnitude limit of $J(AB) = 22.8$ mag, have a $\sim 25\%$ flux uncertainty. Since it is obvious from the previous section that systematic errors have a minimal effect on the $D(4000)$ and $D_n(4000)$ measurements, my goal was to quantify the effect of these random errors on the reliability of $D(4000)$.

I compared the measured values for $D(4000)$ and $D_n(4000)$ to their intrinsic values for each galaxy and plotted the result against magnitude to gain a better understanding of how random uncertainties affect these measurements. All the plots can be found in the Appendix, but one representative plot is displayed in Figure 3.13. The $D(4000)$ and $D_n(4000)$ measurements are almost always within 10% and often within 5% of their intrinsic values at all magnitudes I used in the feasibility study. The only two exceptions occurred when $J(AB) = 22.8$ mag; the measured value of $D(4000)$ differed from its true value by greater than 10% at $\tau_V = 3.0$, $Z/Z_\odot = 0.2$, and $t = 0.5$, and the measured value of $D_n(4000)$ differed from its true value by greater than 10% at $\tau_V = 3.0$, $Z/Z_\odot = 0.2$, and $t = 0.0$. Overall, there were no noticeable trends with magnitude in

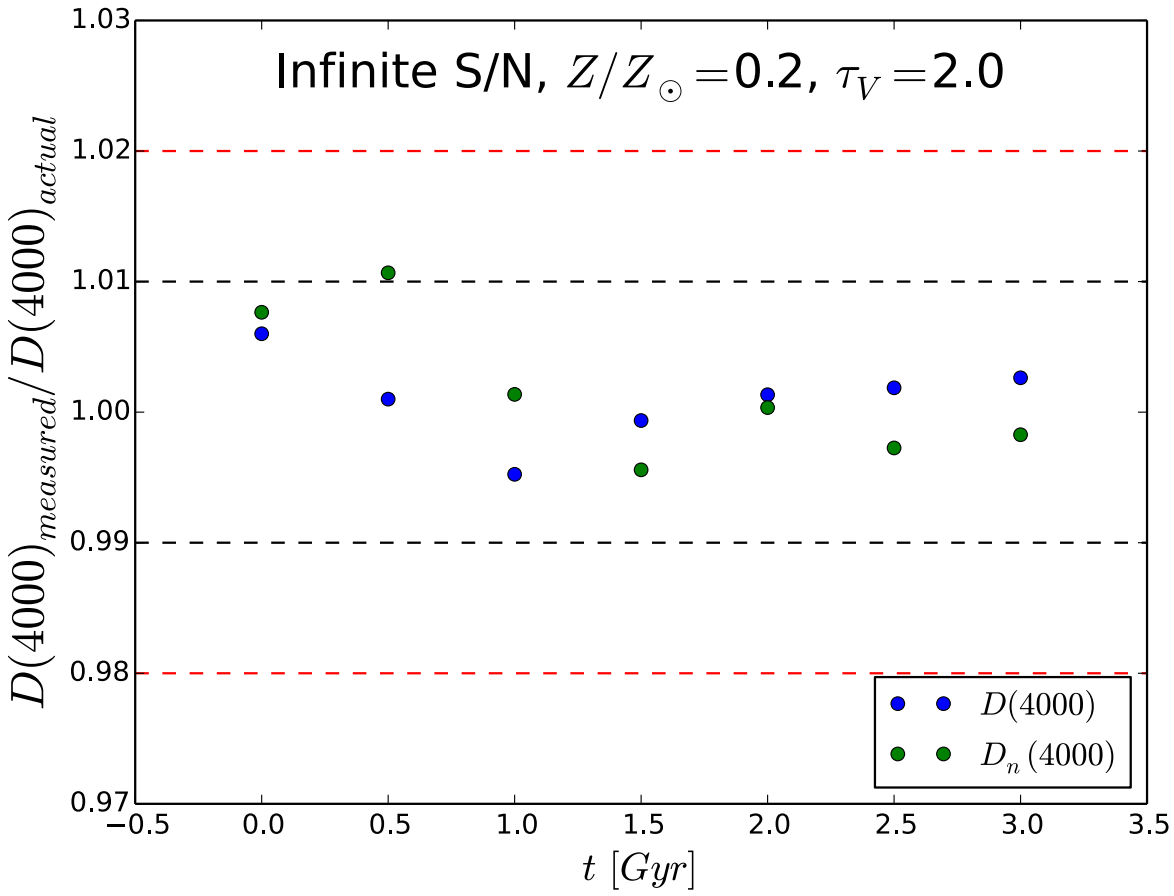

Figure 3.11: The measured $D(4000)$ (or $D_n(4000)$) value divided by the intrinsic $D(4000)$ ($D_n(4000)$) measurement for seven galaxies with infinite signal-to-noise measurements, a metal abundance of $Z/Z_\odot = 0.2$, and an optical depth of $\tau_V = 2.0$. The black dotted lines correspond to a 1% difference from unity, and the red dotted lines correspond to a 2% difference. For these galaxies with varying times t since star formation ended, all measurements fall within 2% of unity. No age biases in the strength of the 4000 Å break were observed.

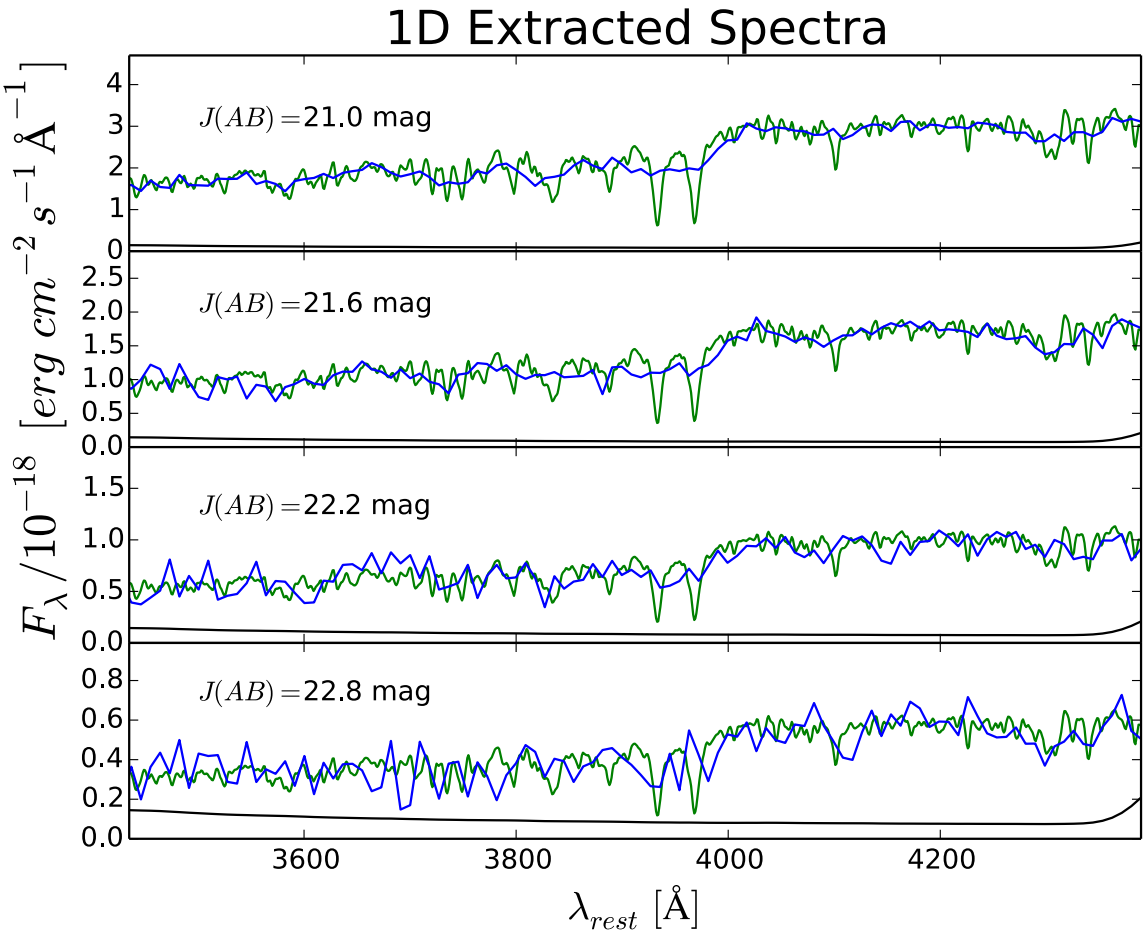

Figure 3.12: Bruzual & Charlot GALAXEV galaxy template spectrum, aXeSIM extracted spectrum for a 10-orbit HST observation, and uncertainty in the extracted spectrum at each magnitude used in the feasibility study. The effect of these random errors on the reliability of $D(4000)$, or equivalently, $D_n(4000)$, is the end goal of this study. The green line in each plot represents the intrinsic spectrum of a galaxy with metallicity $Z/Z_\odot = 0.2$, attenuation optical depth $\tau_V = 0.0$, and elapsed time since the end of star formation $t = 3$. This spectrum is identical in all four plots. The blue line gives the aXeSIM one-dimensional extracted spectrum, with a measurement uncertainty shown by the black line on the bottom of each plot. The magnitudes represented in the plots are, from top to bottom, $J(AB) = 21.0$ mag, $J(AB) = 21.6$ mag, $J(AB) = 22.2$ mag, and $J(AB) = 22.8$ mag.

$D(4000)_{measured}/D(4000)_{actual}$ that remained regular across multiple parameter sets. In addition, neither $D(4000)$ nor $D_n(4000)$ were consistently high or low.

For a subset of the galaxies in my grid of Bruzual & Charlot GALAXEV template galaxy spectra, I plotted the uncertainties in $D(4000)$ and $D_n(4000)$ against magnitude to see how much a change in magnitude from $J(AB) = 21.0$ to $J(AB) = 22.8$ changes the uncertainty. The uncertainty in $D(4000)$ or, equivalently, $D_n(4000)$, is always greater at fainter magnitudes due to random error. The random errors associated with the $D_n(4000)$ measurement are always greater than those of the $D(4000)$ because $D_n(4000)$ uses a smaller wavelength range. I found that increasing the metal abundance of a galaxy's stars, aging its stellar population, and increasing the amount of extinction by dust all lead to slightly higher uncertainties. Figures 3.14, 3.15, and 3.16 illustrate these observations for a few galaxies; the remaining figures can be found in the Appendix.

To gain a better understanding of the effect of magnitude on $D(4000)$ measurement uncertainty, I plotted the percent uncertainty in $D(4000)$ against the same four magnitudes used in this feasibility study. The percent error increases with magnitude as expected, and $D_n(4000)$ measurements always have higher percent uncertainties than their corresponding $D(4000)$ measurements. The error is within 10% uncertainty at all magnitudes for all the parameter sets I considered, and it is always within 5% uncertainty for galaxies with J-band magnitudes of 21.6 or brighter. The same trends as above were observed; increasing metallicity, stellar population age, and extinction by dust all lead to slightly raised percent uncertainties. Since these tendencies are more exaggerated in Figures 3.14, 3.15, and 3.16, I did not choose to include any plots presenting the percent uncertainty of $D(4000)$ here. For the curious, these plots are presented in the Appendix for a subset of the galaxies in the grid of models.

The ultimate goal of this feasibility study was to determine the conditions under which a measurement of the $D(4000)$ index reliably constrains the average stellar age of a galaxy at z $\sim$ 1.6 using HST's WFC3 grism. With this in mind, I used a simple linear interpolation technique to establish the effect of an uncertainty in $D(4000)$ on our interpretation of a galaxy's stellar age. Figure 3.17 provides a useful schematic using $D_n(4000)$ with a particular example of one such

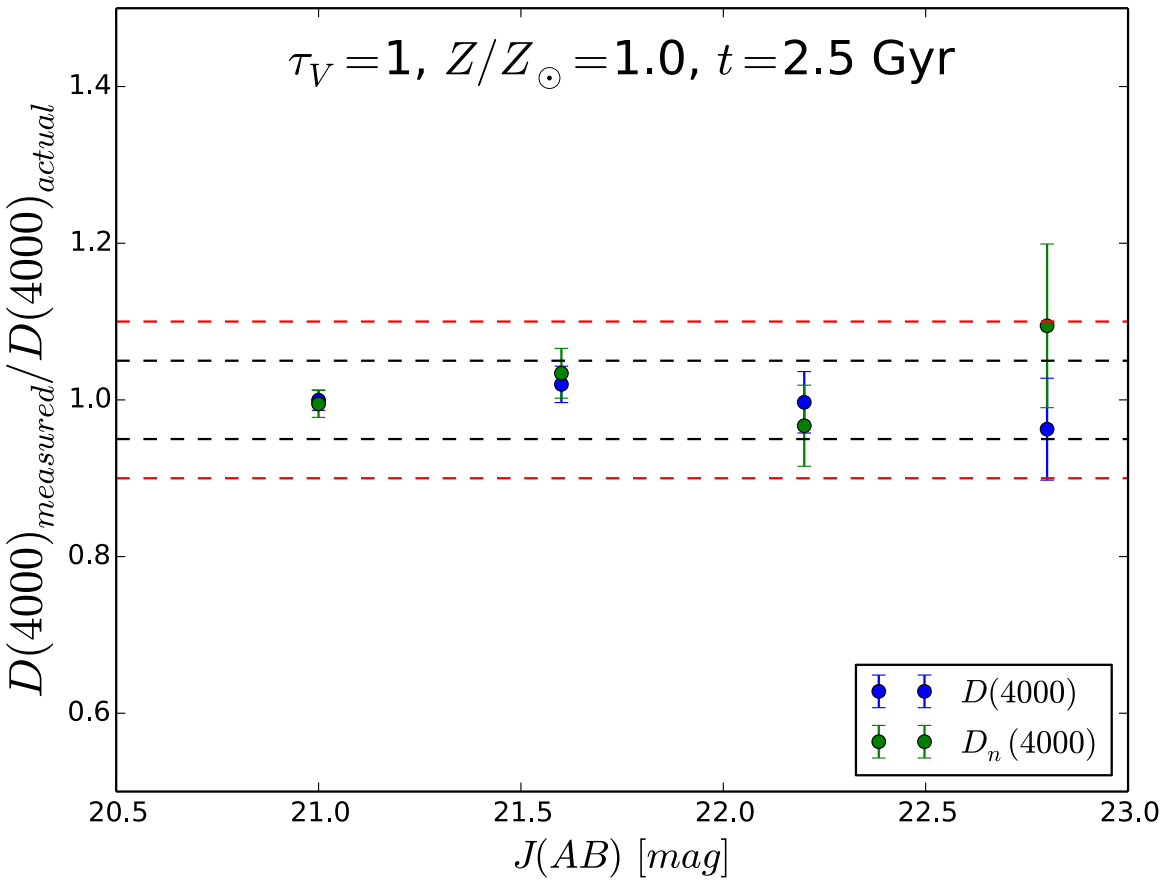

Figure 3.13: The measured $D(4000)$ (or $D_n(4000)$) value divided by the intrinsic $D(4000)$ ($D_n(4000)$) measurement for four galaxies with a metal abundance of $Z/Z_\odot = 1.0$, an optical depth of $\tau_V = 1.0$, and a time $t = 2.5$ Gyr since the end of star formation. The black dotted lines correspond to a 5% difference from unity, and the red dotted lines correspond to a 10% difference. For these four galaxies, all measurements, with their uncertainties, fall within 5% of unity. All simulations correspond to a 10-orbit HST observation. No magnitude biases in the strength of the 4000 Å break were observed.

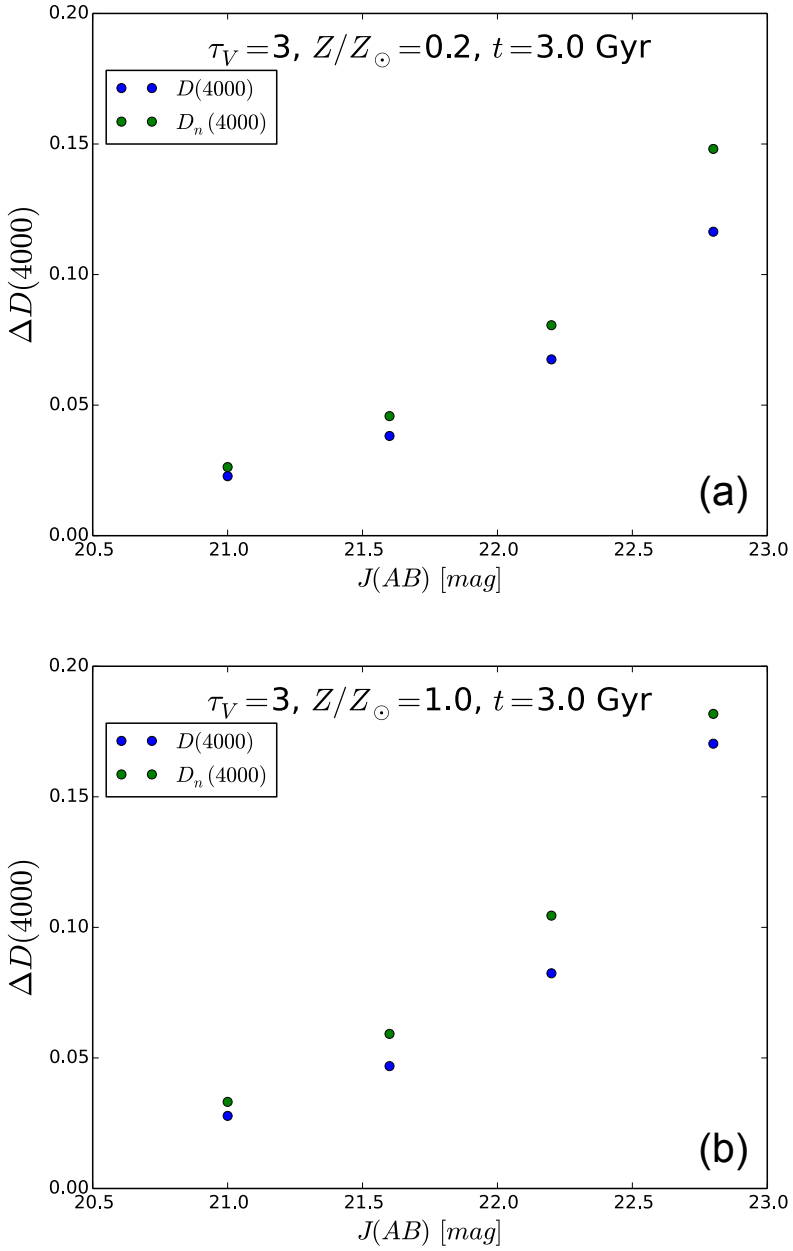

Figure 3.14: Uncertainties $\Delta D(4000)$ in $D(4000)$ and $D_n(4000)$ plotted against the magnitudes considered in the feasibility study. $\Delta D(4000)$ always rises at fainter magnitudes, and the uncertainty in $D_n(4000)$ is always greater than that of $D(4000)$. The galaxies represented in plots (a) and (b) have identical dust extinctions and average stellar ages, but differ in metallicity. An increased metal abundance leads to higher uncertainties in $D(4000)$ and $D_n(4000)$.

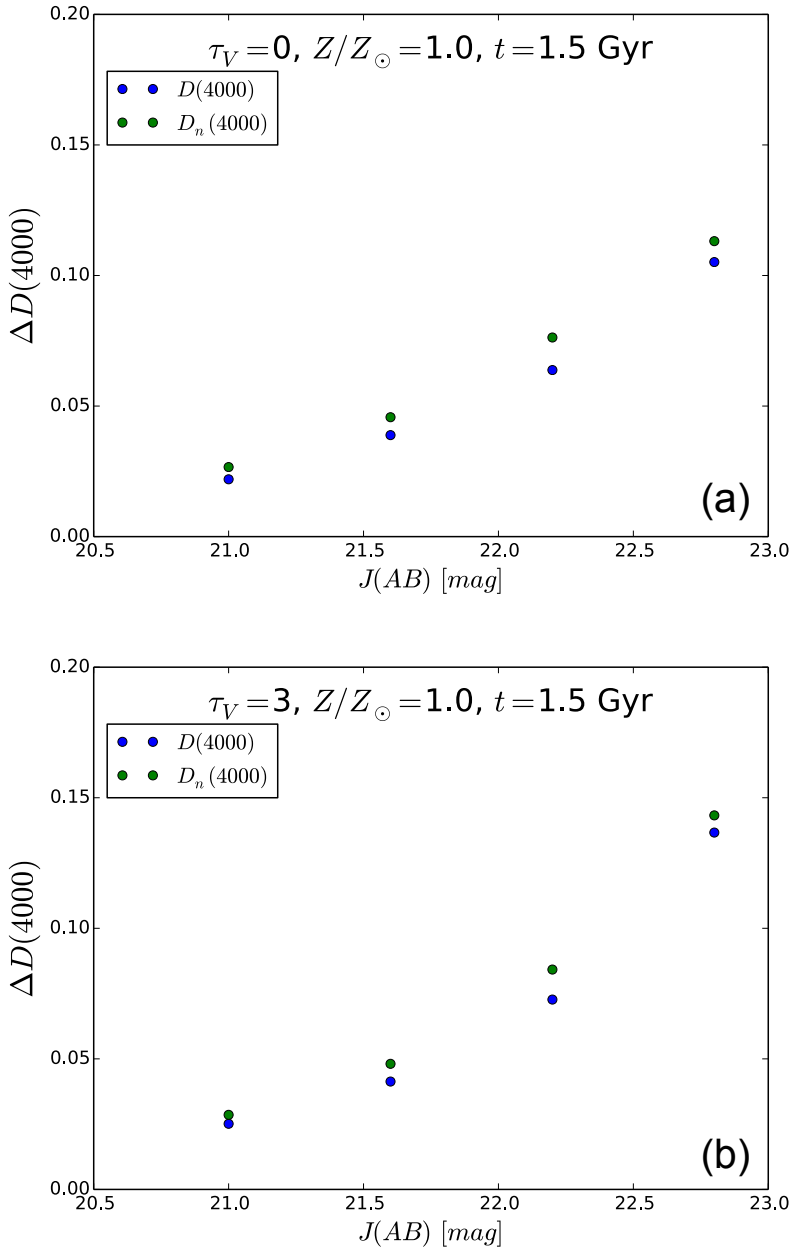

Figure 3.15: Uncertainties $\Delta D(4000)$ in $D(4000)$ and $D_n(4000)$ plotted against a range of magnitudes expected in the observations. $\Delta D(4000)$ increases at faint magnitudes, and the uncertainty in $D_n(4000)$ is always greater than that of $D(4000)$. The galaxies represented in plots (a) and (b) have identical metal abundances and average stellar ages, but differ in dust extinction. Increased dust extinction leads to higher uncertainties in $D(4000)$ and $D_n(4000)$.

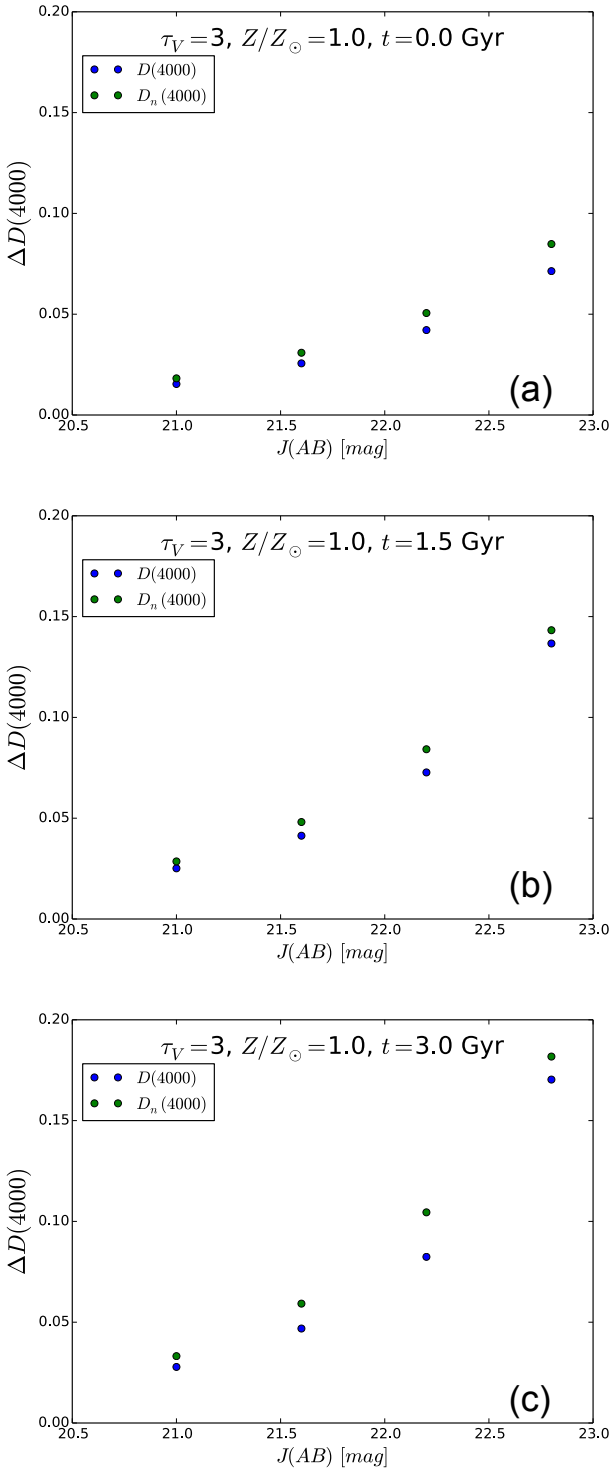

Figure 3.16: Uncertainties $\Delta D(4000)$ in $D(4000)$ and $D_n(4000)$ plotted against the same four magnitudes considered. $\Delta D(4000)$ always increases at fainter magnitudes, and the uncertainty in $D_n(4000)$ is consistently greater than that of $D(4000)$. The galaxies represented in plots (a), (b), and (c) have identical metal abundances dust extinctions, but differ in average stellar age. Increased t leads to higher uncertainties in $D(4000)$ and $D_n(4000)$.

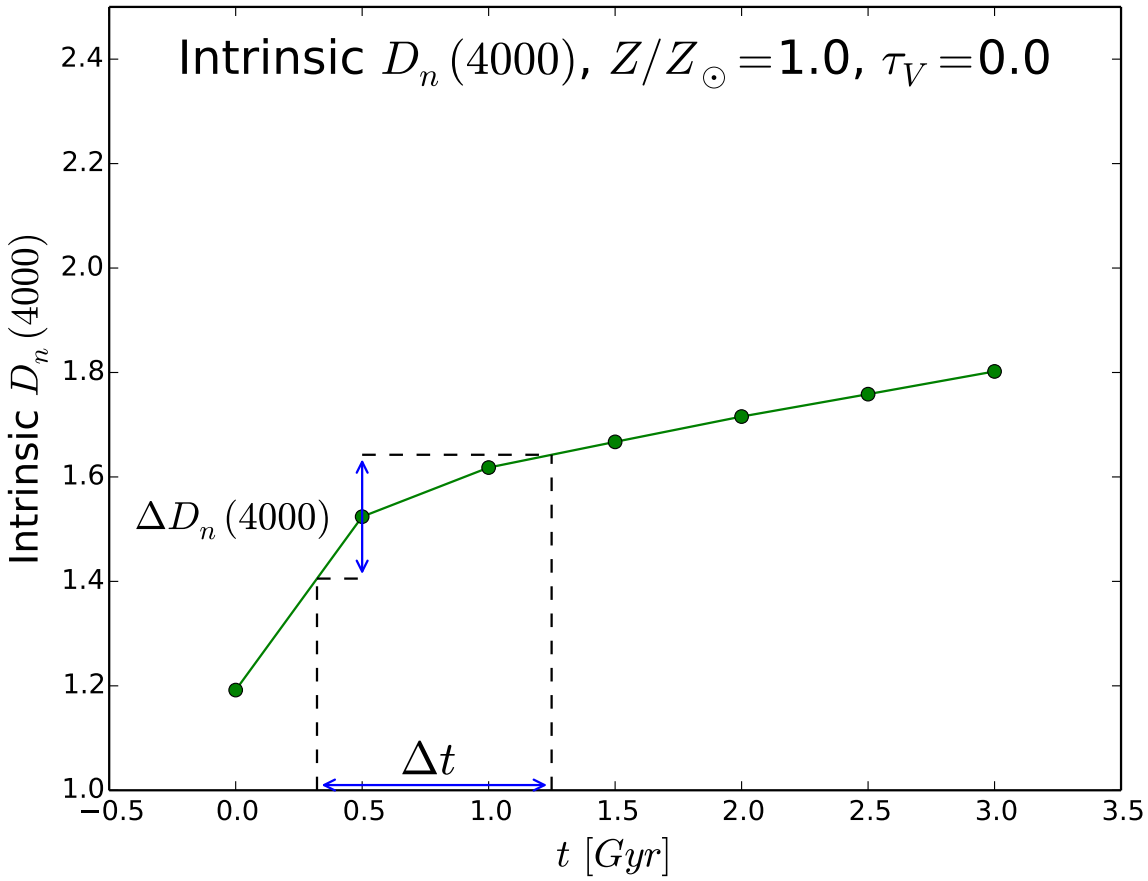

Figure 3.17: Diagram demonstrating how uncertainty in age Δt was calculated. The $D_n(4000)$ versus t plot corresponding to the galaxy's metallicity and dust extinction was first described using a piecewise function of linear interpolations between data points. Then, the uncertainty in $D_n(4000)$ was matched to a range in average stellar ages Δt as shown in the schematic.

calculation. I began with a plot of the intrinsic $D_n(4000)$ value versus age t, and I described the relationship roughly using a piecewise linear function. I then found the range in t spanned by the uncertainty in $D_n(4000)$ according to my linear interpolations between $D_n(4000)$ data points. It is clear that $D(4000)$ is not very sensitive to average stellar age after about 1 Gyr, so high values age uncertainty are expected. Since there are no major systematic biases, I only considered a subset of the model galaxies: those with $\tau_V = 0.0$ and $Z/Z_\odot = 1.0$.

All stellar age uncertainty plots for galaxies with dust extinction $\tau_V = 0.0$ and metallicity $Z/Z_\odot = 1.0$ but different values of t are found in Figure 3.18. The uncertainty in age Δt at a

particular age always rises at fainter magnitudes. In general, the uncertainty at each magnitude increases with the t parameter. Furthermore, $D_n(4000)$ leads to higher age uncertainties than does $D(4000)$.

Even more useful is the percent uncertainty in average stellar age calculated using the strength of the 4000 Å break. Figure 3.19 shows the percent uncertainty in age corresponding to the six plots in Figure 3.18. As before, an increase in percent uncertainty is observed with fainter magnitudes, but now the increase in percent uncertainty is associated with decreasing age. The $D_n(4000)$ index always leads to higher percent uncertainties than does the $D(4000)$ index. Unfortunately, these plots prove that it is difficult to precisely constrain stellar age using the 4000 Å break alone at the magnitudes expected in the HST observations. Any galaxy at the study's magnitude limit of $J(AB) = 22.8$ mag will have an uncertainty in age of around 100% or higher. The galaxies I considered at $J(AB) = 22.2$ mag all had greater than 50% uncertainties, as well. A measurement of the strength of the 4000 Å break could potentially be useful at magnitudes of $\sim$21.6 or brighter; the model galaxies in this feasibility study gave an error in age of about 50% at $J(AB) = 21.6$ mag and less than 50% at $J(AB) = 21.0$ mag. It is worth noting that these uncertainties are only valid for the particular SFH I used in my models; the error in age is even greater without knowing the SFH of the galaxies. At the very least, my collaborators should be able to use the 4000 Å break to tell the difference between a galaxy with an old stellar population and a galaxy containing young stars for sufficiently bright galaxies.

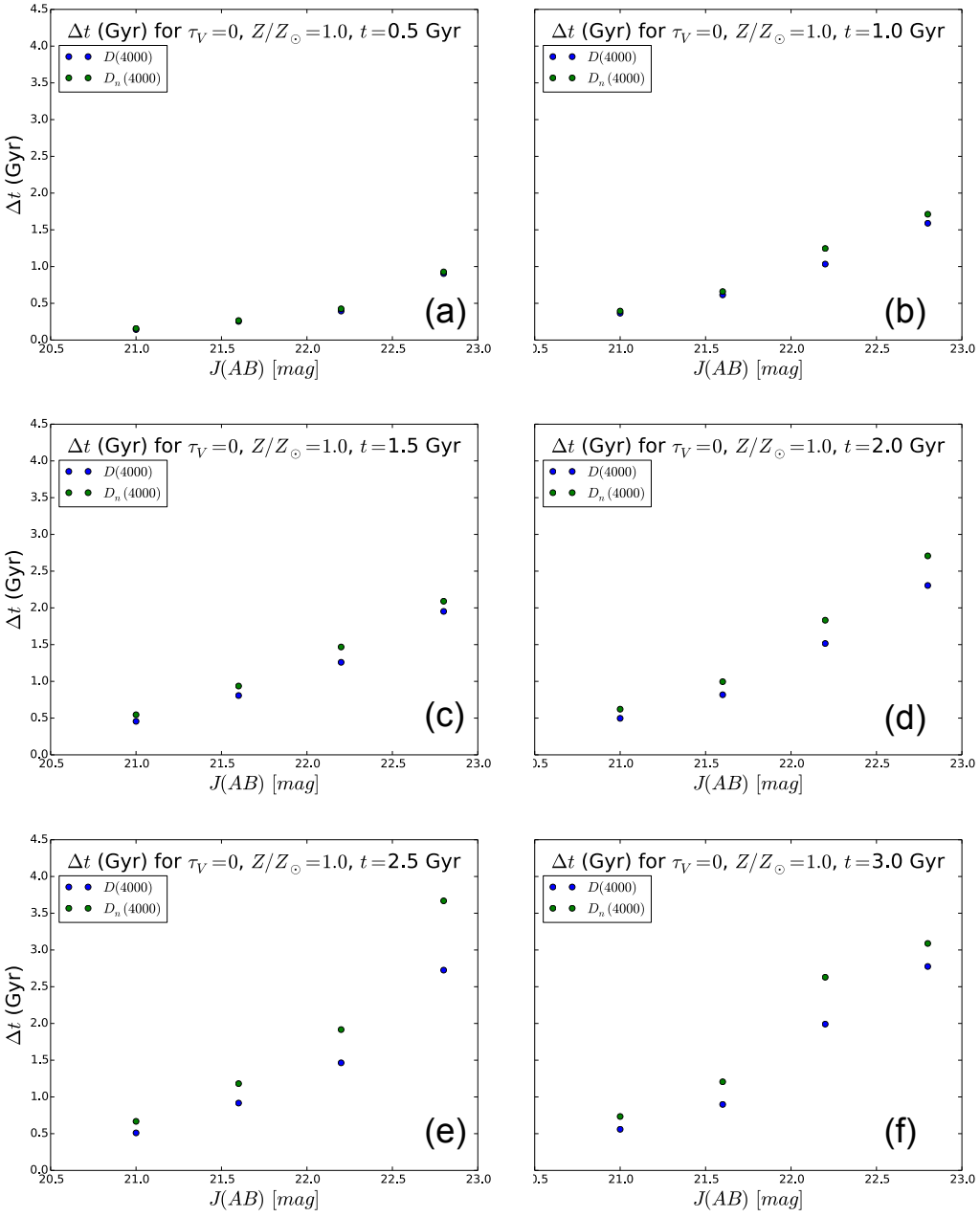

Figure 3.18: Stellar age uncertainty plots for $\tau_V = 0.0$ and $Z/Z_\odot = 1.0$. Age uncertainties are calculated using the method demonstrated in Figure 3.17. The value of Δt increases at fainter magnitudes for a fixed stellar population age; it also increases for older stellar populations at a fixed magnitude. Using $D_n(4000)$ always gives higher age uncertainties than using $D(4000)$ gives. The six plots correspond to values of t: (a) $t = 0.5$ Gyr, (b) $t = 1.0$ Gyr, (c) $t = 1.5$ Gyr, (d) $t = 2.0$ Gyr, (e) $t = 2.5$ Gyr, and (f) $t = 3.0$ Gyr.

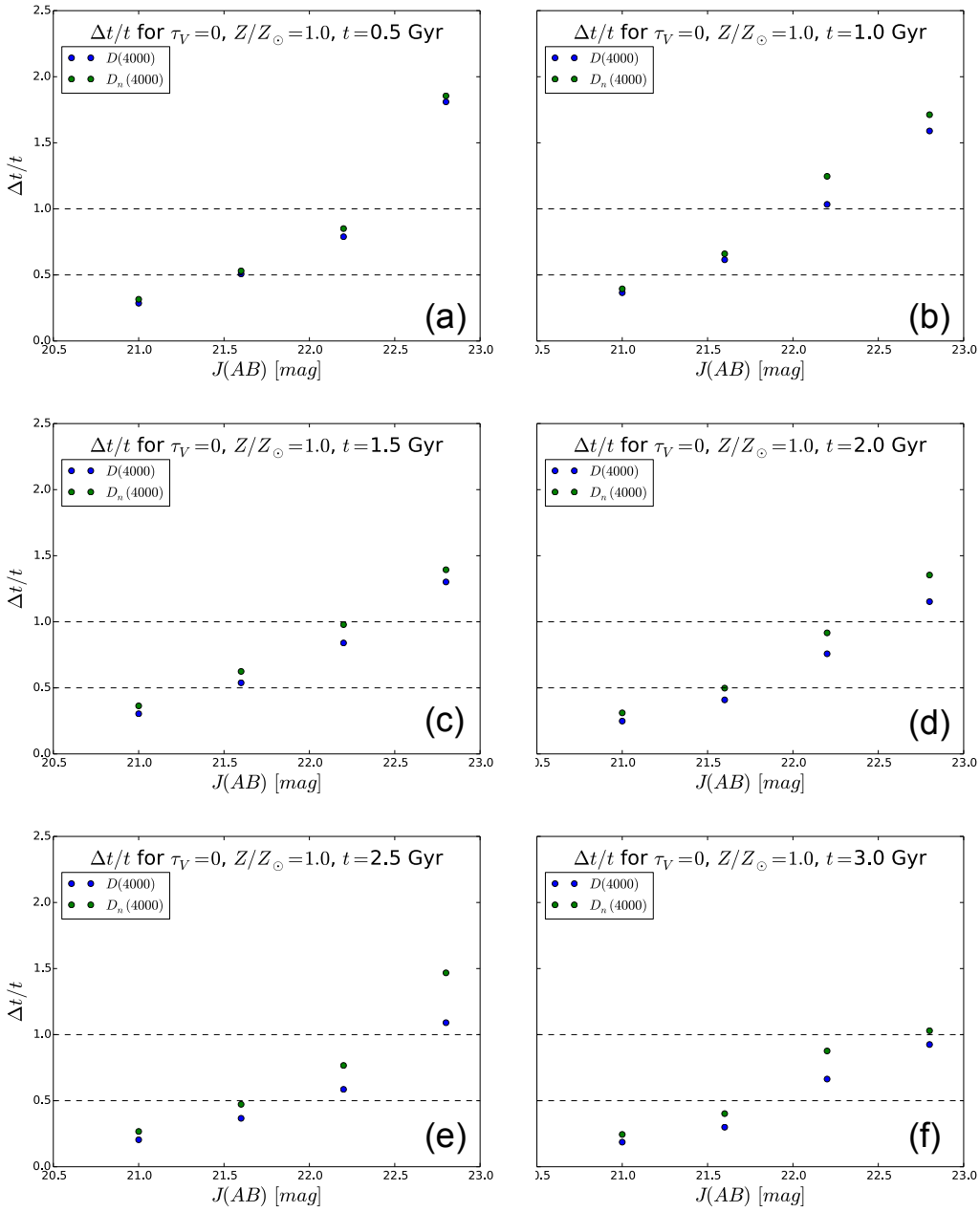

Figure 3.19: Stellar age percent uncertainty plots for $\tau_V = 0.0$ and $Z/Z_\odot = 1.0$. Age uncertainties are calculated using the method demonstrated in Figure 3.17. The value of $\Delta t/t$ increases at fainter magnitudes and increases at larger values of t. Dotted lines at 50% uncertainty and 100% uncertainty help prove the difficulty of accurately constraining stellar age using $D(4000)$ at these magnitudes. Although uncertainties are too high to be useful for the $J(AB) = 22.2$ mag and $J(AB) = 22.8$ mag galaxies, the strength of the 4000 Å break could potentially be measured to get a general idea of stellar population age at magnitudes around $J(AB) = 21.6$ mag or brighter. The six plots correspond to values of t: (a) $t = 0.5$ Gyr, (b) $t = 1.0$ Gyr, (c) $t = 1.5$ Gyr, (d) $t = 2.0$ Gyr, (e) $t = 2.5$ Gyr, and (f) $t = 3.0$ Gyr.

Chapter 4

Discussion and Limitations

The first goal of this feasibility study was to measure $D(4000)$ and $D_n(4000)$ for simulated observations of a grid of Bruzual & Charlot model galaxies at z = 1.62 and determine if the two indices are systematically biased for different SFHs, ages, metallicities, and optical depths. No major biases were observed by varying t, which combines SFH and time since star formation ended, the attenuation optical depth τ_V, and the metallicity Z. In particular, varying τ_V caused almost no change in a galaxy's spectrum because I utilized Bruzual & Charlot's two-part attenuation model, described in Section 2.1, instead of a simple dust screen. Although Bruzual & Charlot's 'birth cloud' optical depth is physically motivated, the giant molecular birth clouds disperse so suddenly that varying τ_V has virtually no effect, even when $t = 0$. Once the birth clouds disperse, there is almost no extinction difference between galaxies with different values of τ_V; this can be seen in plots of the intrinsic template galaxy spectra. A different dust model might serve my purposes by allowing me to better understand the effect of dust extinction on a galaxy's spectrum, the strength of its 4000 Å break, and ultimately the percent error in average stellar age calculated using the $D_n(4000)$ index.

To gain a general idea of biases in $D_(4000)$ and $D_n(4000)$ with age, I varied a parameter called t, described in Section 2.3, that intertwines SFH and time elapsed since the end of star formation. In determining the properties of real galaxies, the effect of stellar age and SFH on

spectra would have to be disentangled. This is complicated by the fact that my results only apply for the simple SFH model given in Section 2.3; excluding our knowledge of SFH would cause even greater uncertainties in stellar age found with $D_n(4000)$. However, the general results of my feasibility study, that systematic biases in $D_n(4000)$ with age and SFH are negligible and that ages can be precisely constrained for only the brightest galaxies at z $\sim$ 1.6 due to random error, are still useful for high-redshift clusters observed using the WFC3 prisms aboard HST.

There were very few systematic effects in the $D(4000)$ and $D_n(4000)$ indices across the parameter space considered in my grid of model galaxies. The $D(4000)$ offset with respect to the intrinsic spectrum's $D(4000)$ measurement is very small and does not depend on age/SFH, dust extinction, or metallicity. Instead, random error, associated with simulating observations of galaxies at different magnitudes, played the largest role in determining the precision with which $D(4000)$ and $D_n(4000)$ can be reconstructed and the associated uncertainty in average stellar age obtained by measuring the strength of the 4000 Å break. Plotting the percent error in $D(4000)$ and $D_n(4000)$ revealed that the error is within 5% uncertainty for galaxies with J-band magnitudes of 21.6 or brighter and within 10% uncertainty for magnitudes up to the study's magnitude limit of $J(AB) = 22.8$ mag. The percent error in average stellar age calculated from a $D(4000)$ or $D_n(4000)$ measurement, however, does not enjoy the same accuracy. Only those galaxies with a magnitude of 21.6 or brighter have errors within $\sim$50% uncertainty.

The measurement uncertainties inherent in the aXeSIM one-dimensional extracted galaxy spectra lead to uncertainties in $D(4000)$ and $D_n(4000)$ measurements for these galaxies, which in turn correspond to large uncertainties in average stellar age since neither $D(4000)$ nor $D_n(4000)$ has much sensitivity to age after about 1 Gyr. The calculated uncertainties in age for this feasibility study, which mostly taken into consideration the random component of error, become even larger if SFH is unknown. It is therefore very difficult to accurately constrain a galaxy's average stellar age using a measurement of the $D(4000)$ index. For the galaxies in my grid of models, a magnitude of $J(AB) = 22.8$ mag corresponds to an uncertainty in age of greater than $\sim$100%, $J(AB) = 22.2$ mag to an uncertainty of greater than $\sim$50%, $J(AB) = 21.6$ mag to an uncertainty of

$\sim$50%, and $J(AB) = 21.0$ mag (the brightest galaxy magnitude expected in the HST observations of IRC 0218A) to an uncertainty of less than $\sim$50%. This means that $D_n(4000)$ alone cannot be used to reconstruct stellar age in galaxies with magnitudes greater than about 21.6, but $D_n(4000)$ may at least be able to distinguish between a young ($\sim$0.5 Gyr) and an old ($\sim$3.0 Gyr) stellar population in the brightest galaxies. Had I considered asymmetric error bars in reconstructed stellar age, rather than symmetric error bars only (yielding Δt), our ability to determine age would be improved. Furthermore, if multiple galaxies are stacked in bins of magnitude or fit simultaneously using a library of model galaxy templates, the sample as a whole might have reasonable uncertainties, allowing researchers to look for trends of stellar age with other galaxy parameters. At the very least, other spectral features sensitive to age, in addition to $D_n(4000)$, could be considered in galaxies too faint to use $D_n(4000)$ alone. For example, the H_δ absorption line is sensitive to age and falls within our grism spectral range.

There appears to be no major difference in stellar age percent uncertainty between using $D(4000)$ and $D_n(4000)$. $D(4000)$ will always have less random noise than $D_n(4000)$ for a single measurement, but it is also more susceptible to dust and will therefore always be more biased than $D_n(4000)$. Therefore, $D_n(4000)$, even with its slightly less precise constraint on stellar age, can be used in studies where the small difference in error does not drastically affect the result.

Chapter 5

Summary and Conclusions

The goal of this project was three-fold: determine if $D(4000)$ and $D_n(4000)$, commonly used probes for the light-weighted stellar age of galaxies, are systematically biased for different SFHs, ages, metallicities, and optical depths; determine the precision with which $D(4000)$ can be reconstructed for galaxies at a range of magnitudes; and analyze the uncertainty in average stellar age, obtained by using the strength of the 4000 Å break, to find the conditions under which a measurement of $D(4000)$ is a reliable probe of a stellar population's age. This is ultimately a feasibility study for the analysis of HST observations of galaxy cluster IRC 0218A, at a redshift of z = 1.62. The results will be useful for observations of any galaxies at a redshift around z $\sim$ 1.6 made with HST's WFC3/G102L infrared grism.

My grid of template galaxies was constructed using the GALAXEV package described by Bruzual & Charlot (2003). I varied three parameters: the metallicity Z, the 'birth cloud' optical depth τ_V, and a time parameter t that intertwines SFH and elapsed time since star formation ended. For the simple SFHs I used to make the grid of models, $D(4000)$ and $D_n(40000)$ increase monotonically with t. To simulate WFC3 grism observations at a range of galaxy magnitudes, I used the aXeSIM software package.

The first part of this feasibility study involved a search for systematic biases in $D(4000)$ and $D_n(4000)$ for different SFHs/ages, metallicities, and dust extinctions. No obvious systematic bi-

ases were observed by varying any of the three parameters. Instead, random noise in the observations plays the largest role in the precision with which the strength of the 4000 Å break can be measured and the average stellar age reconstructed.

To better understand the effect of magnitude and therefore random error on $D(4000)$ measurement uncertainty, I plotted the percent uncertainty in $D(4000)$ against galaxy magnitude. The error is within 10% uncertainty at all magnitudes and within 5% for galaxies with J-band magnitudes of 21.6 or brighter. However, since $D(4000)$ is not as sensitive to stellar age after a galaxy's star formation has been cut off for about 1 Gyr, even a small error in a $D(4000)$ measurement can correspond to a large error in calculated stellar age. Plotting the percent uncertainty in t, calculated using the measured strength of the 4000 Å break, against galaxy magnitude proves how difficult it is to precisely constrain stellar age in high redshift galaxies using only $D(4000)$. For the particular SFH I used in my models, galaxies with $J(AB) = 22.8$ mag have at least a $\sim$100% uncertainty in age, galaxies with $J(AB) = 22.2$ mag have at least a $\sim$50% uncertainty, galaxies with $J(AB) = 21.6$ mag have an uncertainty in age of $\sim$50%, and the brightest galaxies considered, those with $J(AB) = 21.0$ mag, have uncertainties barely less than 50%. Furthermore, these errors are even greater if SFH is unknown. Although random errors are too great at all magnitudes in the study to accurately and precisely constrain stellar age using a $D(4000)$ measurement alone, my collaborators should still be able to use the strength of the 4000 Å break to distinguish between very young galaxies and those with older stellar populations. The 4000 Å can also be used in combination with other spectral features to reconstruct stellar age in high-redshift galaxies.

The percent uncertainty in stellar age is always somewhat greater when using $D_n(4000)$ than when using $D(4000)$ because the narrower wavelength bands of the $D_n(4000)$ index mean a lower signal-to-noise ratio. However, $D_n(4000)$ is also less affected by dust than $D(4000)$, so it makes sense to use the narrow measurement in studies where the small difference in random error between the two indices does not affect the result dramatically.

My collaborators will be able to use $D_n(4000)$ in some limited capacity to give a meaningful, if not very precise, constraint on the age of each galaxy's stellar population in IRC 0218A. This

will allow them to study how the ages of the stellar populations in these galaxies vary as a function of other galaxy properties such as mass, dust, and location in the cluster. These trends can be compared to nearby galaxies and to high-redshift field galaxies to learn about galaxy evolution in a variety of conditions.

References

Balogh, M. L., Morris, S. L., Yee, H. K. C., Carlberg, R. G., & Ellingson, E. (1999). Differential Galaxy Evolution in Cluster and Field Galaxies at z˜0.3. ApJ, 527, 54–79.

Bell, E. F., Wolf, C., Meisenheimer, K., Rix, H.-W., Borch, A., Dye, S., Kleinheinrich, M., Wisotzki, L., & McIntosh, D. H. (2004). Nearly 5000 Distant Early-Type Galaxies in COMBO-17: A Red Sequence and Its Evolution since z˜1. ApJ, 608, 752–767.

Borch, A., Meisenheimer, K., Bell, E. F., Rix, H.-W., Wolf, C., Dye, S., Kleinheinrich, M., Kovacs, Z., & Wisotzki, L. (2006). The stellar masses of 25 000 galaxies at $0.2 \leq z \leq 1.0$ estimated by the COMBO-17 survey. A&A, 453, 869–881.

Brammer, G. B., van Dokkum, P. G., Franx, M., Fumagalli, M., Patel, S., Rix, H.-W., Skelton, R. E., Kriek, M., Nelson, E., Schmidt, K. B., Bezanson, R., da Cunha, E., Erb, D. K., Fan, X., Förster Schreiber, N., Illingworth, G. D., Labbé, I., Leja, J., Lundgren, B., Magee, D., Marchesini, D., McCarthy, P., Momcheva, I., Muzzin, A., Quadri, R., Steidel, C. C., Tal, T., Wake, D., Whitaker, K. E., & Williams, A. (2012). 3D-HST: A Wide-field Grism Spectroscopic Survey with the Hubble Space Telescope. ApJS, 200, 13.

Brammer, G. B., Whitaker, K. E., van Dokkum, P. G., Marchesini, D., Franx, M., Kriek, M., Labbé, I., Lee, K.-S., Muzzin, A., Quadri, R. F., Rudnick, G., & Williams, R. (2011). The Number Density and Mass Density of Star-forming and Quiescent Galaxies at $0.4 \leq z \leq 2.2$. ApJ, 739, 24.

Brammer, G. B., Whitaker, K. E., van Dokkum, P. G., Marchesini, D., Labbé, I., Franx, M., Kriek, M., Quadri, R. F., Illingworth, G., Lee, K.-S., Muzzin, A., & Rudnick, G. (2009). The Dead Sequence: A Clear Bimodality in Galaxy Colors from z = 0 to z = 2.5. ApJ, 706, L173–L177.

Brown, M. J. I., Dey, A., Jannuzi, B. T., Brand, K., Benson, A. J., Brodwin, M., Croton, D. J., & Eisenhardt, P. R. (2007). The Evolving Luminosity Function of Red Galaxies. ApJ, 654, 858–877.

Bruzual, G. & Charlot, S. (2003). Stellar population synthesis at the resolution of 2003. MNRAS, 344, 1000–1028.

Bruzual A., G. (1983). Spectral evolution of galaxies. I - Early-type systems. ApJ, 273, 105–127.

Bruzual A., G. & Charlot, S. (1993). Spectral evolution of stellar populations using isochrone synthesis. ApJ, 405, 538–553.

Cassata, P., Cimatti, A., Kurk, J., Rodighiero, G., Pozzetti, L., Bolzonella, M., Daddi, E., Mignoli, M., Berta, S., Dickinson, M., Franceschini, A., Halliday, C., Renzini, A., Rosati, P., & Zamorani, G. (2008). GMASS ultradeep spectroscopy of galaxies at z $\tilde{2}$. III. The emergence of the color bimodality at z $\tilde{2}$. A&A, 483, L39–L42.

Chabrier, G. (2003). Galactic Stellar and Substellar Initial Mass Function. PASP, 115, 763–795.

Charlot, S. & Bruzual, A. G. (1991). Stellar population synthesis revisited. ApJ, 367, 126–140.

Charlot, S. & Fall, S. M. (2000). A Simple Model for the Absorption of Starlight by Dust in Galaxies. ApJ, 539, 718–731.

Daddi, E., Dickinson, M., Chary, R., Pope, A., Morrison, G., Alexander, D. M., Bauer, F. E., Brandt, W. N., Giavalisco, M., Ferguson, H., Lee, K.-S., Lehmer, B. D., Papovich, C., & Renzini, A. (2005). The Population of BzK-selected ULIRGs at z ˜ 2. ApJ, 631, L13–L16.

Dressel, L. (2014). *WFC3 Instrument Handbook*. Space Telescope Science Institute.

Faber, S. M., Willmer, C. N. A., Wolf, C., Koo, D. C., Weiner, B. J., Newman, J. A., Im, M., Coil, A. L., Conroy, C., Cooper, M. C., Davis, M., Finkbeiner, D. P., Gerke, B. F., Gebhardt, K., Groth, E. J., Guhathakurta, P., Harker, J., Kaiser, N., Kassin, S., Kleinheinrich, M., Konidaris, N. P., Kron, R. G., Lin, L., Luppino, G., Madgwick, D. S., Meisenheimer, K., Noeske, K. G., Phillips, A. C., Sarajedini, V. L., Schiavon, R. P., Simard, L., Szalay, A. S., Vogt, N. P., & Yan, R. (2007). Galaxy Luminosity Functions to z˜1 from DEEP2 and COMBO-17: Implications for Red Galaxy Formation. ApJ, 665, 265–294.

Galametz, A., Stern, D., Pentericci, L., De Breuck, C., Vernet, J., Wylezalek, D., Fassbender, R., Hatch, N., Kurk, J., Overzier, R., Rettura, A., & Seymour, N. (2013). A large-scale galaxy structure at z = 2.02 associated with the radio galaxy MRC 0156-252. A&A, 559, A2.

Gallazzi, A., Bell, E. F., Zibetti, S., Brinchmann, J., & Kelson, D. D. (2014). Charting the Evolution of the Ages and Metallicities of Massive Galaxies since z = 0.7. ApJ, 788, 72.

Gallazzi, A., Charlot, S., Brinchmann, J., White, S. D. M., & Tremonti, C. A. (2005). The ages and metallicities of galaxies in the local universe. MNRAS, 362, 41–58.

Gobat, R., Strazzullo, V., Daddi, E., Onodera, M., Carollo, M., Renzini, A., Finoguenov, A., Cimatti, A., Scarlata, C., & Arimoto, N. (2013). WFC3 GRISM Confirmation of the Distant Cluster Cl J1449+0856 at langzrang = 2.00: Quiescent and Star-forming Galaxy Populations. ApJ, 776, 9.

Hernán-Caballero, A., Alonso-Herrero, A., Pérez-González, P. G., Cardiel, N., Cava, A., Ferreras, I., Barro, G., Tresse, L., Daddi, E., Cenarro, J., Conselice, C. J., Guzmán, R., & Gallego, J. (2013). SHARDS: stellar populations and star formation histories of a mass-selected sample of $0.65 < z < 1.1$ galaxies. MNRAS, 434, 2136–2152.

Ilbert, O., McCracken, H. J., Le Fèvre, O., Capak, P., Dunlop, J., Karim, A., Renzini, M. A., Caputi, K., Boissier, S., Arnouts, S., Aussel, H., Comparat, J., Guo, Q., Hudelot, P., Kartaltepe, J., Kneib, J. P., Krogager, J. K., Le Floc'h, E., Lilly, S., Mellier, Y., Milvang-Jensen, B.,

Moutard, T., Onodera, M., Richard, J., Salvato, M., Sanders, D. B., Scoville, N., Silverman, J. D., Taniguchi, Y., Tasca, L., Thomas, R., Toft, S., Tresse, L., Vergani, D., Wolk, M., & Zirm, A. (2013). Mass assembly in quiescent and star-forming galaxies since $z \simeq 4$ from UltraVISTA. A&A, 556, A55.

Kauffmann, G., Heckman, T. M., White, S. D. M., Charlot, S., Tremonti, C., Peng, E. W., Seibert, M., Brinkmann, J., Nichol, R. C., SubbaRao, M., & York, D. (2003). The dependence of star formation history and internal structure on stellar mass for 10^5 low-redshift galaxies. MNRAS, 341, 54–69.

Kriek, M., van der Wel, A., van Dokkum, P. G., Franx, M., & Illingworth, G. D. (2008). The Detection of a Red Sequence of Massive Field Galaxies at z ˜ 2.3 and Its Evolution to z ˜ 0. ApJ, 682, 896–906.

Kroupa, P. (2001). On the variation of the initial mass function. MNRAS, 322, 231–246.

Labbé, I., Huang, J., Franx, M., Rudnick, G., Barmby, P., Daddi, E., van Dokkum, P. G., Fazio, G. G., Schreiber, N. M. F., Moorwood, A. F. M., Rix, H.-W., Röttgering, H., Trujillo, I., & van der Werf, P. (2005). IRAC Mid-Infrared Imaging of the Hubble Deep Field-South: Star Formation Histories and Stellar Masses of Red Galaxies at $z > 2$. ApJ, 624, L81–L84.

Le Borgne, J.-F., Bruzual, G., Pelló, R., Lançon, A., Rocca-Volmerange, B., Sanahuja, B., Schaerer, D., Soubiran, C., & Vílchez-Gómez, R. (2003). STELIB: A library of stellar spectra at R ˜ 2000. A&A, 402, 433–442.

Lotz, J. M., Papovich, C., Faber, S. M., Ferguson, H. C., Grogin, N., Guo, Y., Kocevski, D., Koekemoer, A. M., Lee, K.-S., McIntosh, D., Momcheva, I., Rudnick, G., Saintonge, A., Tran, K.-V., van der Wel, A., & Willmer, C. (2013). Caught in the Act: The Assembly of Massive Cluster Galaxies at z = 1.62. ApJ, 773, 154.

Mateus, A., Sodré, L., Cid Fernandes, R., Stasińska, G., Schoenell, W., & Gomes, J. M. (2006).

Semi-empirical analysis of Sloan Digital Sky Survey galaxies - II. The bimodality of the galaxy population revisited. MNRAS, 370, 721–737.

Moustakas, J., Coil, A. L., Aird, J., Blanton, M. R., Cool, R. J., Eisenstein, D. J., Mendez, A. J., Wong, K. C., Zhu, G., & Arnouts, S. (2013). PRIMUS: Constraints on Star Formation Quenching and Galaxy Merging, and the Evolution of the Stellar Mass Function from z = 0-1. ApJ, 767, 50.

Muzzin, A., Marchesini, D., Stefanon, M., Franx, M., McCracken, H. J., Milvang-Jensen, B., Dunlop, J. S., Fynbo, J. P. U., Brammer, G., Labbé, I., & van Dokkum, P. G. (2013a). The Evolution of the Stellar Mass Functions of Star-forming and Quiescent Galaxies to z = 4 from the COSMOS/UltraVISTA Survey. ApJ, 777, 18.

Muzzin, A., Wilson, G., Demarco, R., Lidman, C., Nantais, J., Hoekstra, H., Yee, H. K. C., & Rettura, A. (2013b). Discovery of a Rich Cluster at z = 1.63 Using the Rest-frame 1.6 μm "Stellar Bump Sequence" Method. ApJ, 767, 39.

Newman, A. B., Ellis, R. S., Andreon, S., Treu, T., Raichoor, A., & Trinchieri, G. (2014). Spectroscopic Confirmation of the Rich z = 1.80 Galaxy Cluster JKCS 041 using the WFC3 Grism: Environmental Trends in the Ages and Structure of Quiescent Galaxies. ApJ, 788, 51.

Newman, A. B., Ellis, R. S., Bundy, K., & Treu, T. (2012). Can Minor Merging Account for the Size Growth of Quiescent Galaxies? New Results from the CANDELS Survey. ApJ, 746, 162.

Papovich, C. (2008). The Angular Clustering of Distant Galaxy Clusters. ApJ, 676, 206–217.

Papovich, C., Momcheva, I., Willmer, C. N. A., Finkelstein, K. D., Finkelstein, S. L., Tran, K.-V., Brodwin, M., Dunlop, J. S., Farrah, D., Khan, S. A., Lotz, J., McCarthy, P., McLure, R. J., Rieke, M., Rudnick, G., Sivanandam, S., Pacaud, F., & Pierre, M. (2010). A Spitzer-selected Galaxy Cluster at z = 1.62. ApJ, 716, 1503–1513.

Rudnick, G. H., Tran, K.-V., Papovich, C., Momcheva, I., & Willmer, C. (2012). A Tale of Dwarfs and Giants: Using a z = 1.62 Cluster to Understand How the Red Sequence Grew over the Last 9.5 Billion Years. ApJ, 755, 14.

Stanford, S. A., Brodwin, M., Gonzalez, A. H., Zeimann, G., Stern, D., Dey, A., Eisenhardt, P. R., Snyder, G. F., & Mancone, C. (2012). IDCS J1426.5+3508: Discovery of a Massive, Infrared-selected Galaxy Cluster at z = 1.75. ApJ, 753, 164.

Tanaka, M., Toft, S., Marchesini, D., Zirm, A., De Breuck, C., Kodama, T., Koyama, Y., Kurk, J., & Tanaka, I. (2013). On the Formation Timescale of Massive Cluster Ellipticals Based on Deep Near-infrared Spectroscopy at z ˜ 2. ApJ, 772, 113.

Tran, K.-V. H., Papovich, C., Saintonge, A., Brodwin, M., Dunlop, J. S., Farrah, D., Finkelstein, K. D., Finkelstein, S. L., Lotz, J., McLure, R. J., Momcheva, I., & Willmer, C. N. A. (2010). Reversal of Fortune: Confirmation of an Increasing Star Formation-Density Relation in a Cluster at z = 1.62. ApJ, 719, L126–L129.

Zeimann, G. R., Stanford, S. A., Brodwin, M., Gonzalez, A. H., Snyder, G. F., Stern, D., Eisenhardt, P., Mancone, C., & Dey, A. (2012). IDCS J1433.2+3306: An Infrared-selected Galaxy Cluster at z = 1.89. ApJ, 756, 115.

Appendix A

Appendix

It was not necessary to include all the figures in this Appendix in the Results section, but they are presented here for those who are curious or looking for more information.

A.1 aXeSIM: The Slitless Simulation Package

Figure A.1 shows a sample z = 1.62 galaxy template spectrum and its corresponding aXeSIM extracted spectrum, including uncertainty, at J-band magnitudes of 21.0, 21.6, 22.2, and 22.8 (the magnitude limit of the study). It is easy to see that the uncertainties worsen as the magnitude becomes fainter.

A.2 Model Galaxy Spectra

The Bruzual & Charlot GALAXEV spectra for all galaxies in the grid of models were plotted and normalized to 22.8 mag at 1250 nm, corresponding to the J-band magnitude limit of the study, and any differences in the spectra were noted. Figures A.2, A.3, A.4, and A.5 shows trends in metallicity at all optical depths and average stellar ages. There is very little difference in the spectra for $Z/Z_{\odot} = 0.2$ and $Z/Z_{\odot} = 1.0$ in all cases, but each $Z/Z_{\odot} = 1.0$ spectrum clearly shows a slightly larger 4000 Å break than its corresponding $Z/Z_{\odot} = 0.2$ spectrum. This is because metal

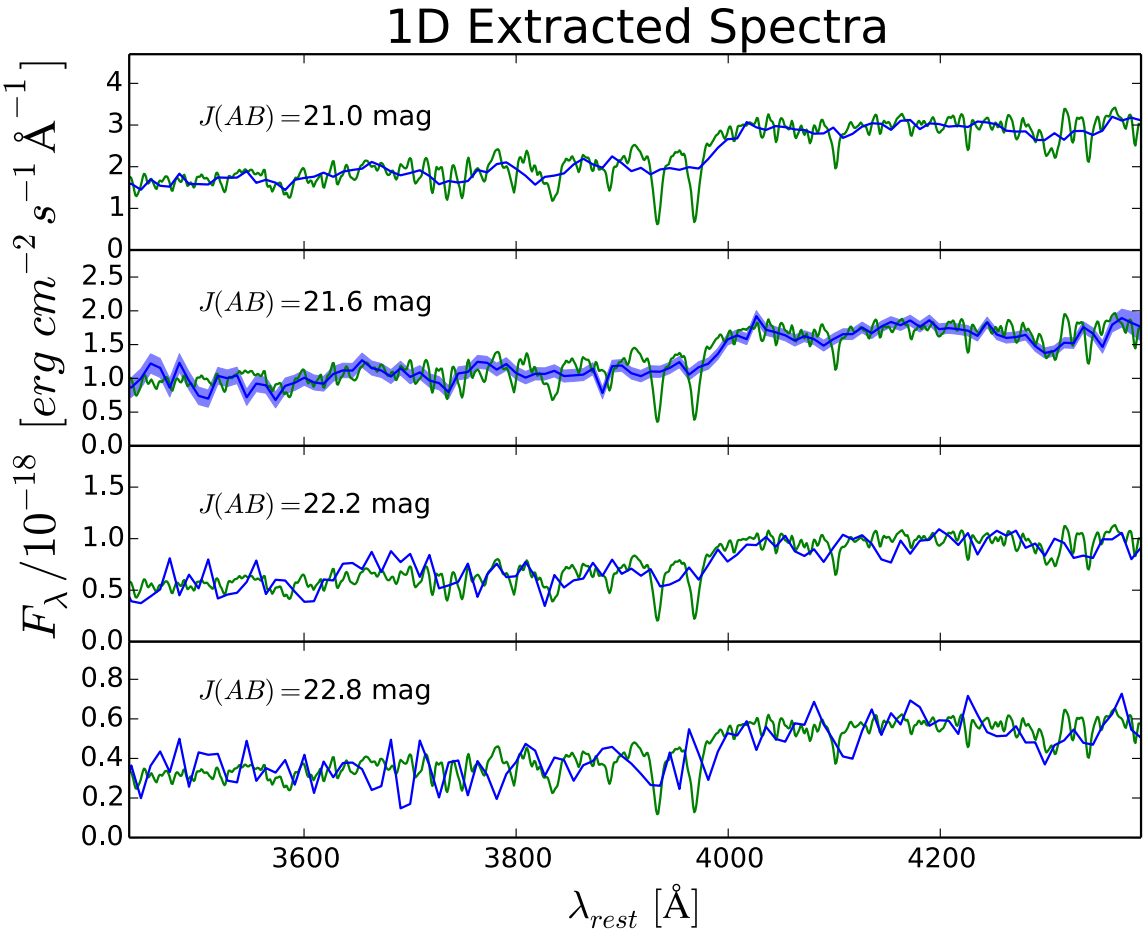

Figure A.1: Sample galaxy template spectrum and its corresponding aXeSIM extracted spectrum for a 10-orbit HST observation. The green line in each plot represents the intrinsic spectrum of a galaxy with metallicity $Z/Z_\odot = 0.2$, attenuation optical depth $\tau_V = 0.0$, and elapsed time since the end of star formation $t = 3$. This spectrum is identical in all four plots. The blue line gives the aXeSIM one-dimensional extracted spectrum, with a measurement uncertainty shown by the blue shaded region. The magnitudes represented in the plots are, from top to bottom, $J(AB) = 21.0$ mag, $J(AB) = 21.6$ mag, $J(AB) = 22.2$ mag, and $J(AB) = 22.8$ mag.

absorption lines are responsible for creating the 4000 Å break. The differences between $Z/Z_{\odot} = 0.2$ and $Z/Z_{\odot} = 1.0$ galaxy spectra increase with increasing age cut to the fact that a galaxy's spectrum becomes less dominated by hot, massive stars with ionized metals (and therefore no metal absorption lines) over time and becomes more dominated by cool stars with noticeable metal lines.

Next, the entire grid of model galaxies was run through aXeSIM. Figures A.6, A.7, A.8, and A.9 show the aXeSIM extracted spectra of the same template galaxies displayed in Figures A.2-A.5, 'observed' at a J-band magnitude of 21.0. At this magnitude, it is possible to see that the $Z/Z_{\odot} = 1.0$ spectra have a larger 4000 Å break than the $Z/Z_{\odot} = 0.2$ spectra.

Figures A.10 and A.11 explore the effect of optical depth on the template spectra. Varying τ_V apparently has an insignificant effect on the spectra once the giant molecular birth clouds disperse at $t = 0.01$ Gyr. Figures A.12 and A.13 show the corresponding aXeSIM extracted spectra.

Figures A.14, A.15, and A.16 illustrate the effect of varying the t parameter on Bruzual & Charlot GALAXEV galaxy spectra. The plot corresponding to $\tau_V = 0.0$ is given in the Results section. As expected, $D(4000)$ increases with increasing t, with the largest jump occurring between the $t = 0.0$ Gyr spectrum and the $t = 0.5$ Gyr spectrum. Figures A.17, A.18, and A.19 show the same plots for the aXeSIM one-dimensional extracted spectra, in which the same trends can be seen.

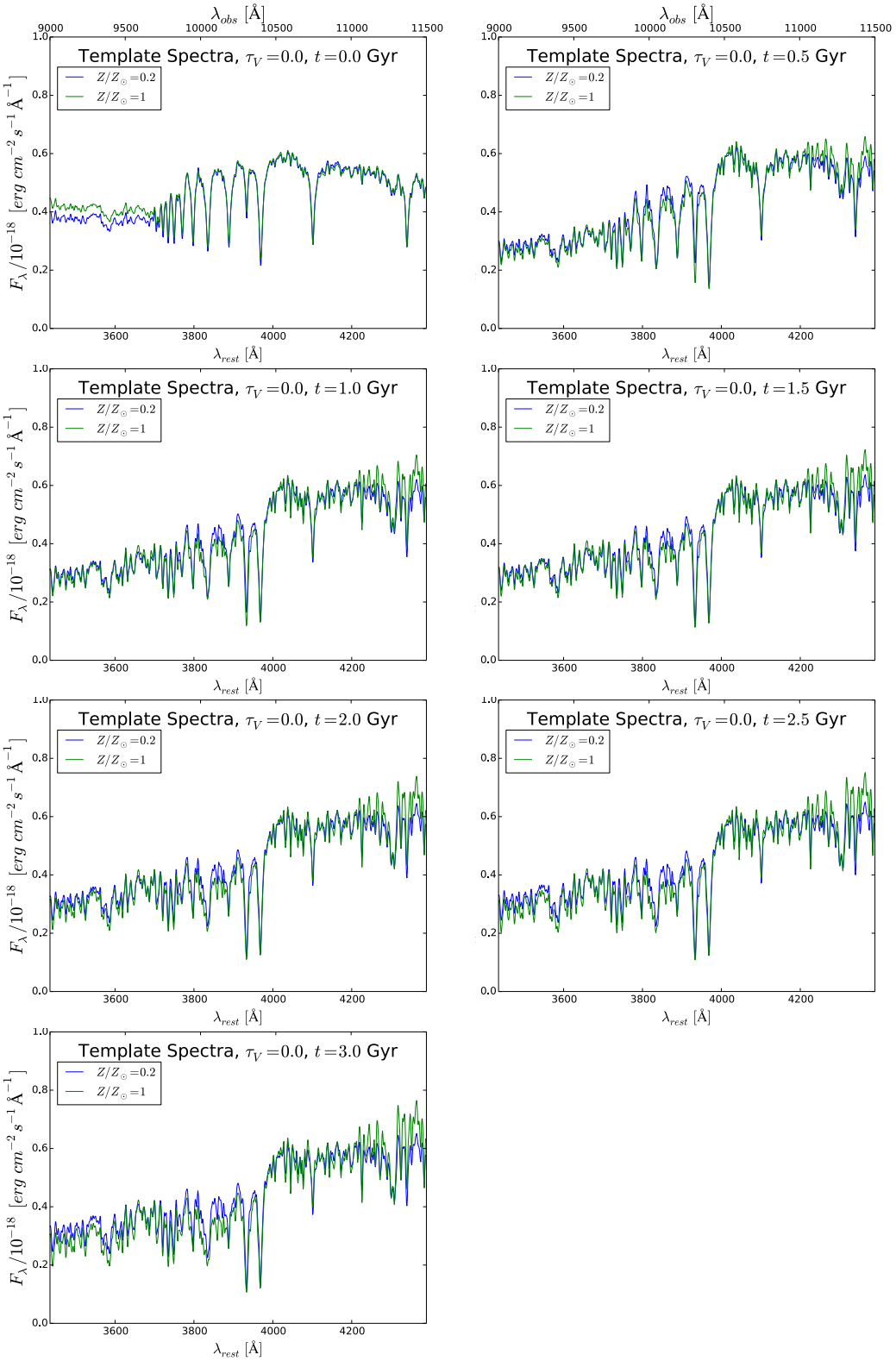

Figure A.2: Bruzual & Charlot GALAXEV spectra, normalized at an observed wavelength of 1250 nm, for galaxies with $\tau_V = 0.0$. Although differences between $Z/Z_\odot = 0.2$ and $Z/Z_\odot = 1.0$ are minor, these differences generally increase with average stellar age, and galaxies with higher metallicity exhibit stronger 4000 Å breaks. The different plots correspond to different values of t.

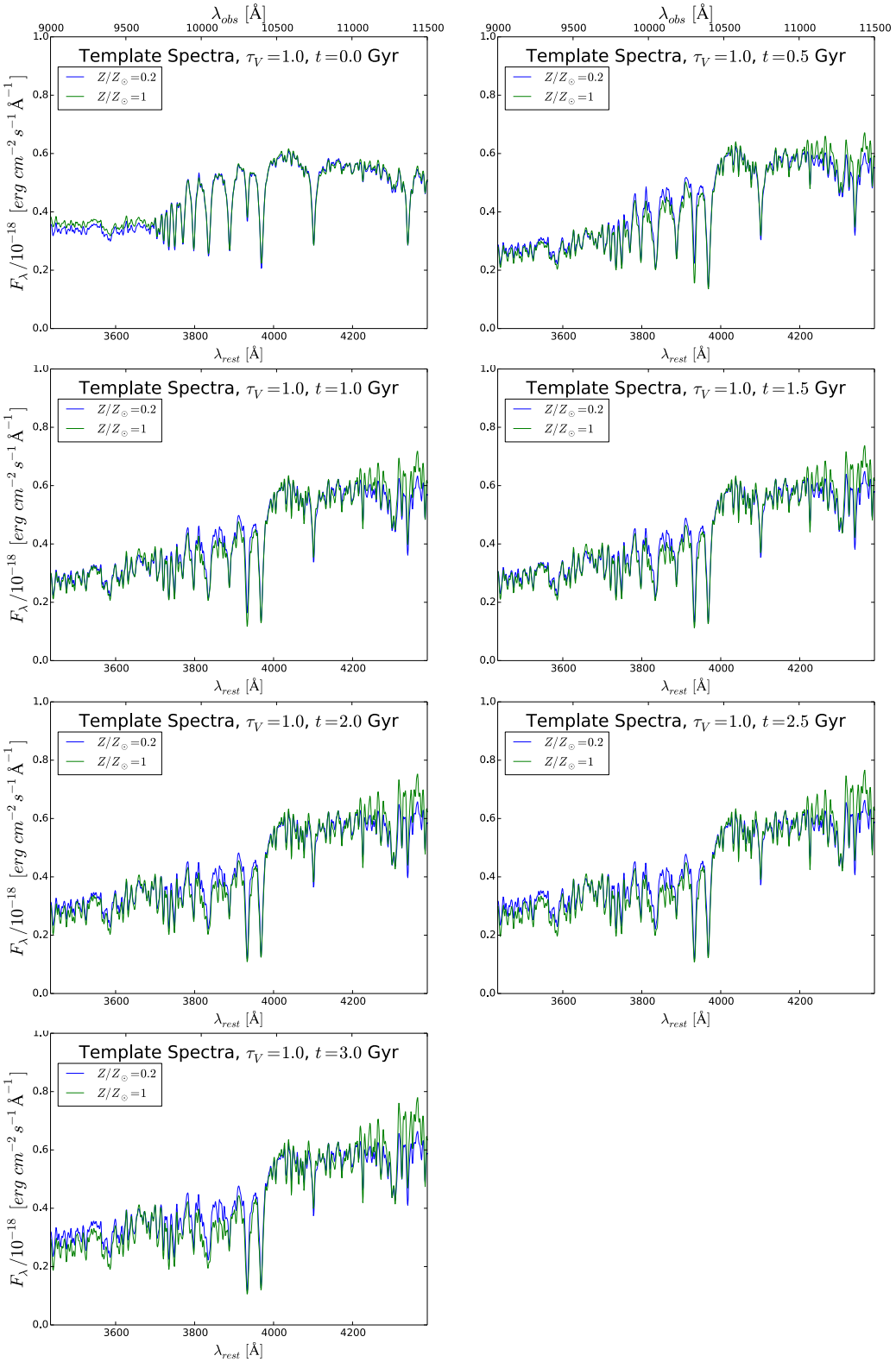

Figure A.3: Bruzual & Charlot GALAXEV spectra, normalized at an observed wavelength of 1250 nm, for galaxies with $\tau_V = 1.0$. Although differences between $Z/Z_\odot = 0.2$ and $Z/Z_\odot = 1.0$ are minor, these differences generally increase with average stellar age, and galaxies with higher metallicity exhibit stronger 4000 Å breaks. The different plots correspond to different values of t.

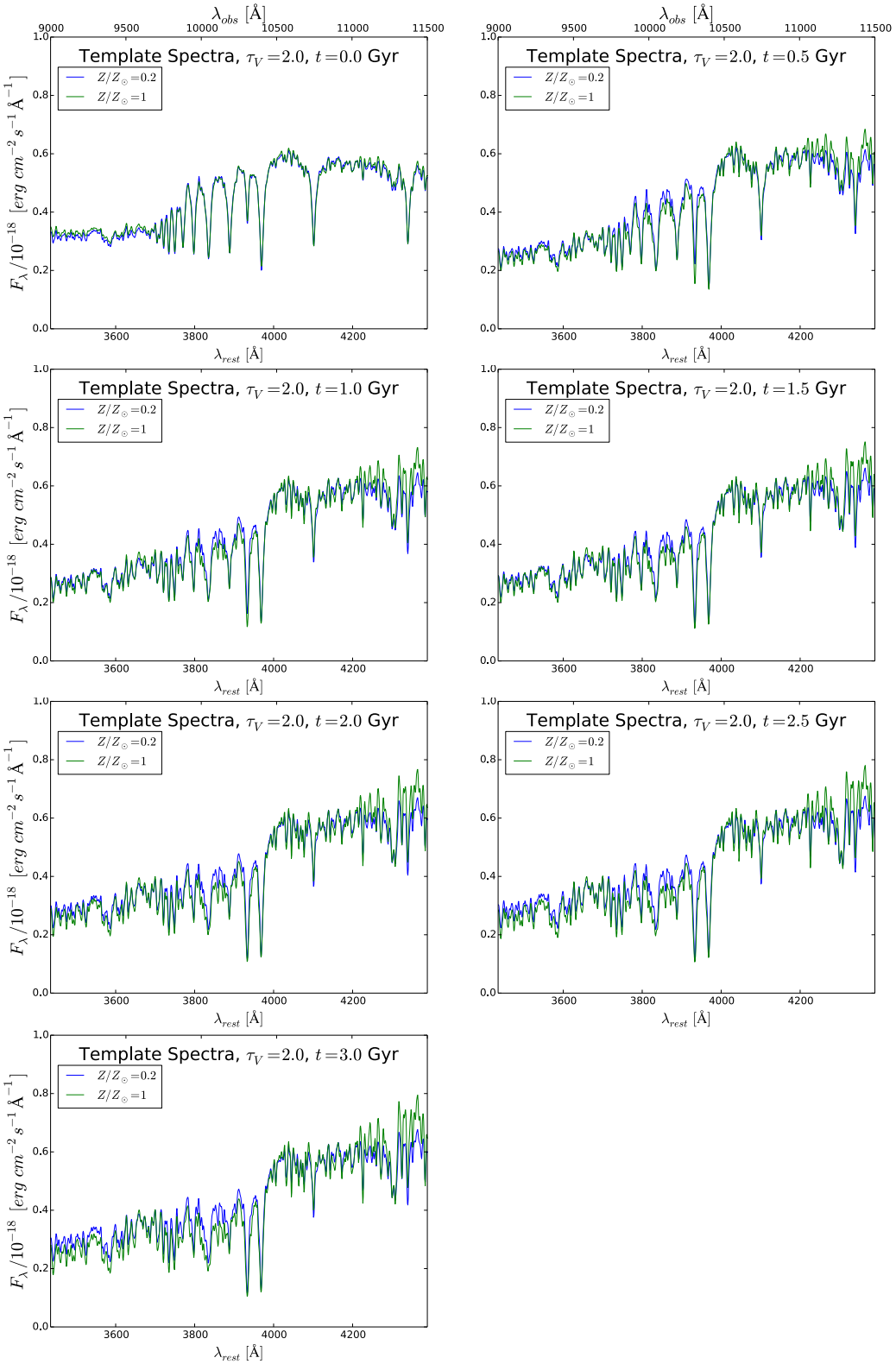

Figure A.4: Bruzual & Charlot GALAXEV spectra, normalized at an observed wavelength of 1250 nm, for galaxies with $\tau_V = 2.0$. Although differences between $Z/Z_\odot = 0.2$ and $Z/Z_\odot = 1.0$ are minor, these differences generally increase with average stellar age, and galaxies with higher metallicity exhibit stronger 4000 Å breaks. The different plots correspond to different values of t.

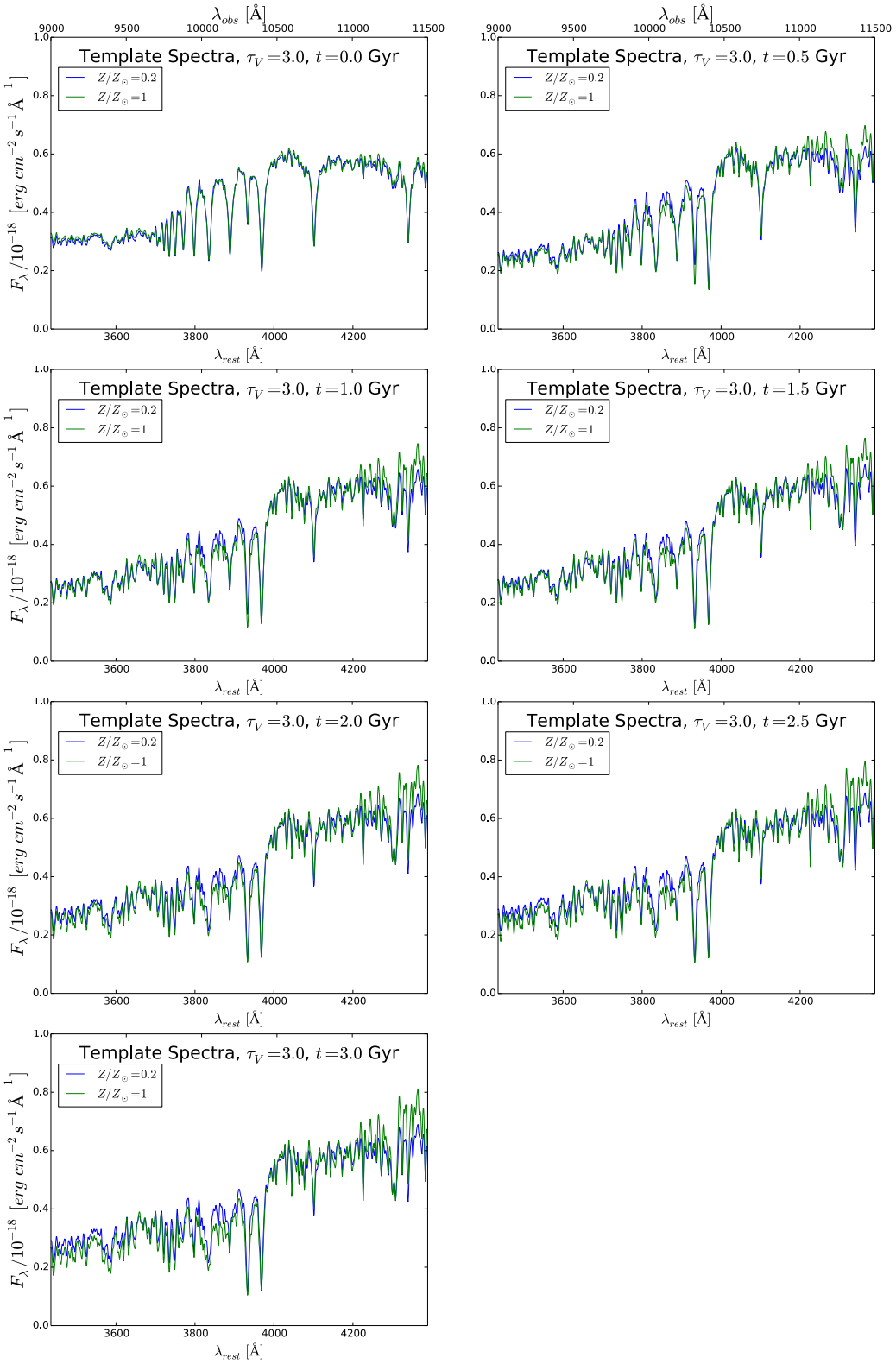

Figure A.5: Bruzual & Charlot GALAXEV spectra, normalized at an observed wavelength of 1250 nm, for galaxies with $\tau_V = 3.0$. Although differences between $Z/Z_\odot = 0.2$ and $Z/Z_\odot = 1.0$ are minor, these differences generally increase with average stellar age, and galaxies with higher metallicity exhibit stronger 4000 Å breaks. The different plots correspond to different values of t.

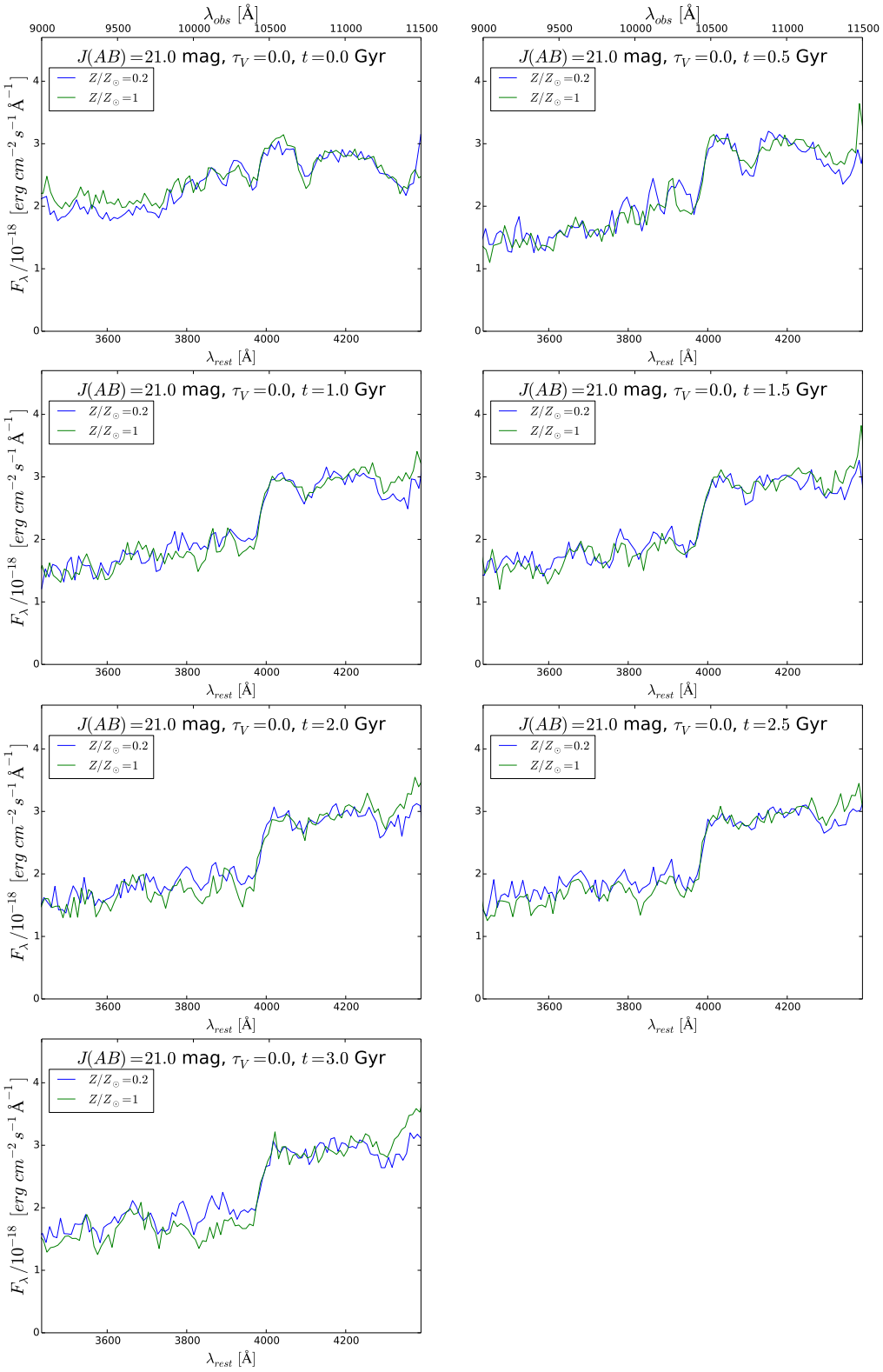

Figure A.6: Extracted aXeSIM spectra, normalized to 21.0 mag at an observed wavelength of 1250 nm, for galaxies with $\tau_V = 0.0$. Although differences between $Z/Z_\odot = 0.2$ and $Z/Z_\odot = 1.0$ are minor, these differences generally increase with average stellar age, and galaxies with higher metallicity exhibit stronger 4000 Å breaks. The different plots correspond to different values of t.

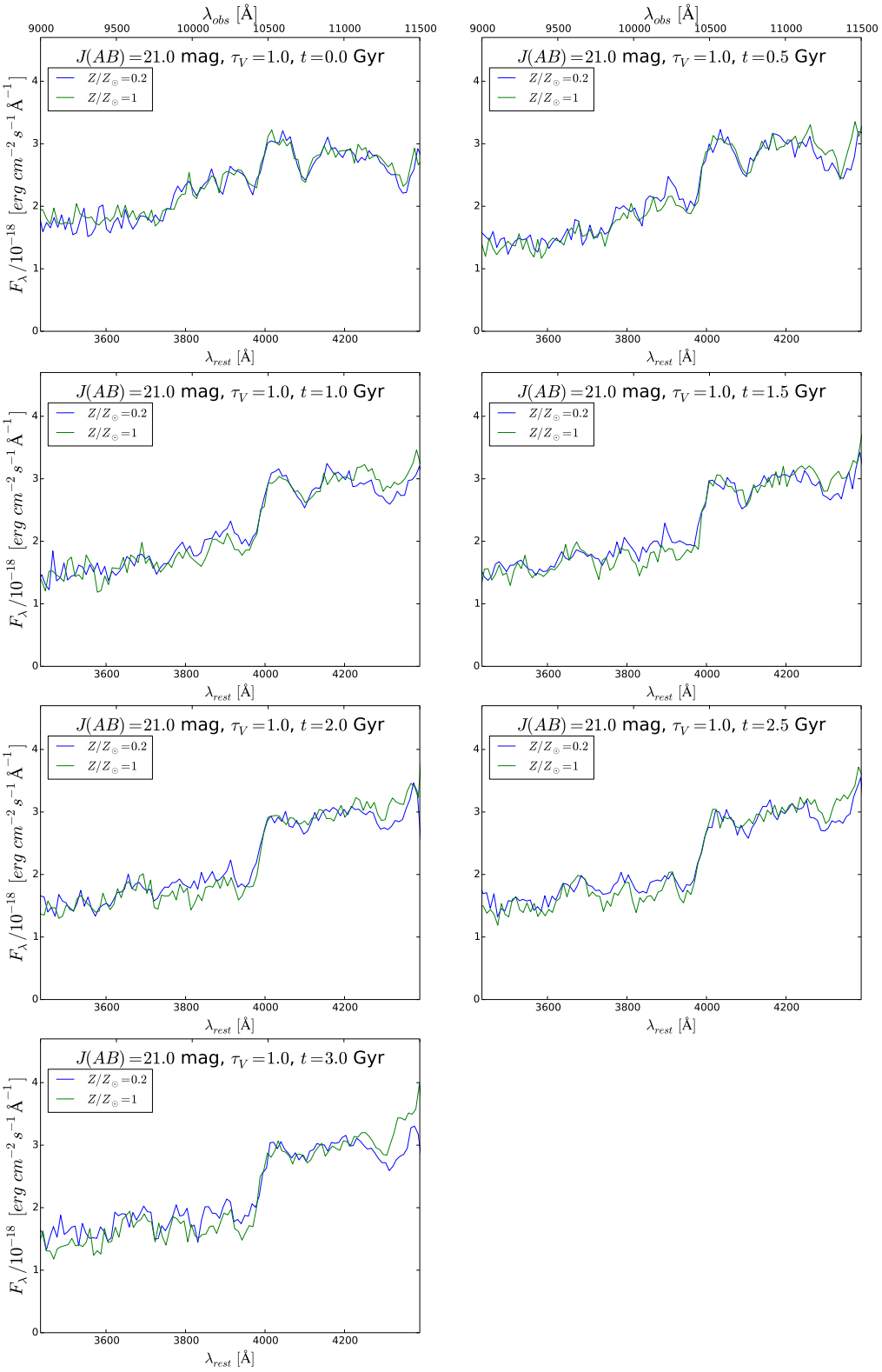

Figure A.7: Extracted aXeSIM spectra, normalized to 21.0 mag at an observed wavelength of 1250 nm, for galaxies with $\tau_V = 1.0$. Although differences between $Z/Z_\odot = 0.2$ and $Z/Z_\odot = 1.0$ are minor, these differences generally increase with average stellar age, and galaxies with higher metallicity exhibit stronger 4000 Å breaks. The different plots correspond to different values of t.

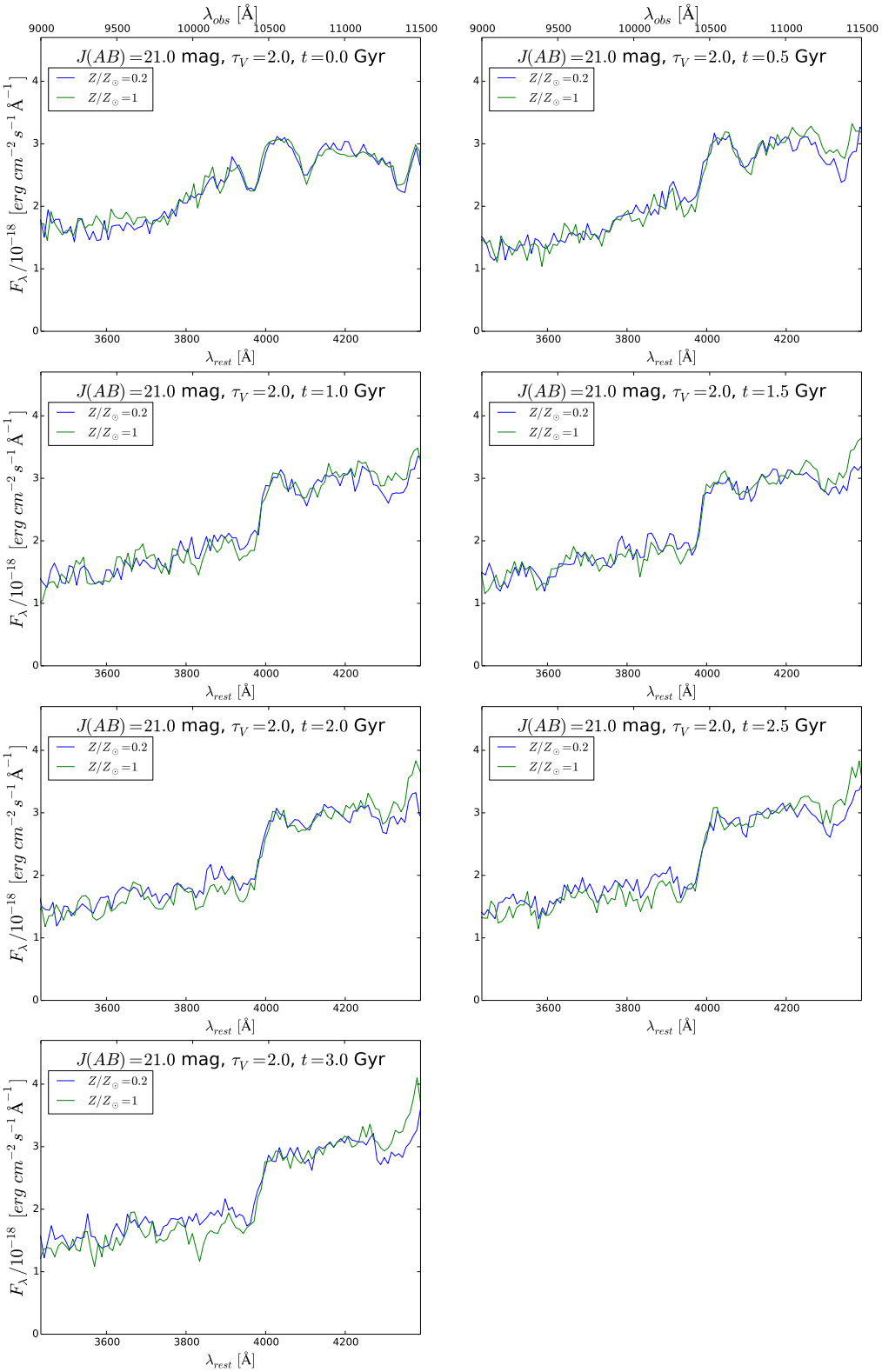

Figure A.8: Extracted aXeSIM spectra, normalized to 21.0 mag at an observed wavelength of 1250 nm, for galaxies with $\tau_V = 2.0$. Although differences between $Z/Z_\odot = 0.2$ and $Z/Z_\odot = 1.0$ are minor, these differences generally increase with average stellar age, and galaxies with higher metallicity exhibit stronger 4000 Å breaks. The different plots correspond to different values of t.

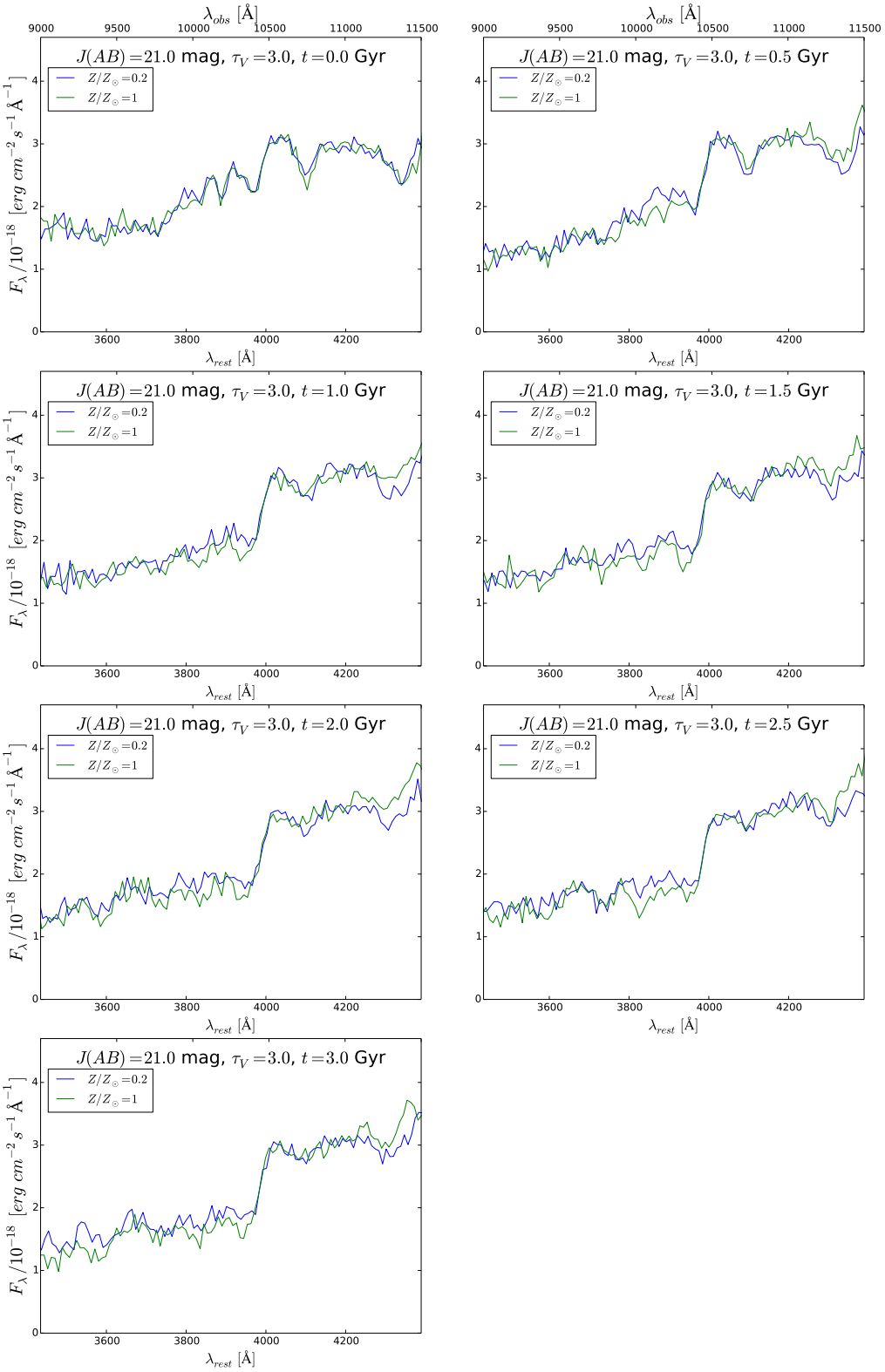

Figure A.9: Extracted aXeSIM spectra, normalized to 21.0 mag at an observed wavelength of 1250 nm, for galaxies with $\tau_V = 3.0$. Although differences between $Z/Z_\odot = 0.2$ and $Z/Z_\odot = 1.0$ are minor, these differences generally increase with average stellar age, and galaxies with higher metallicity exhibit stronger 4000 Å breaks. The different plots correspond to different values of t.

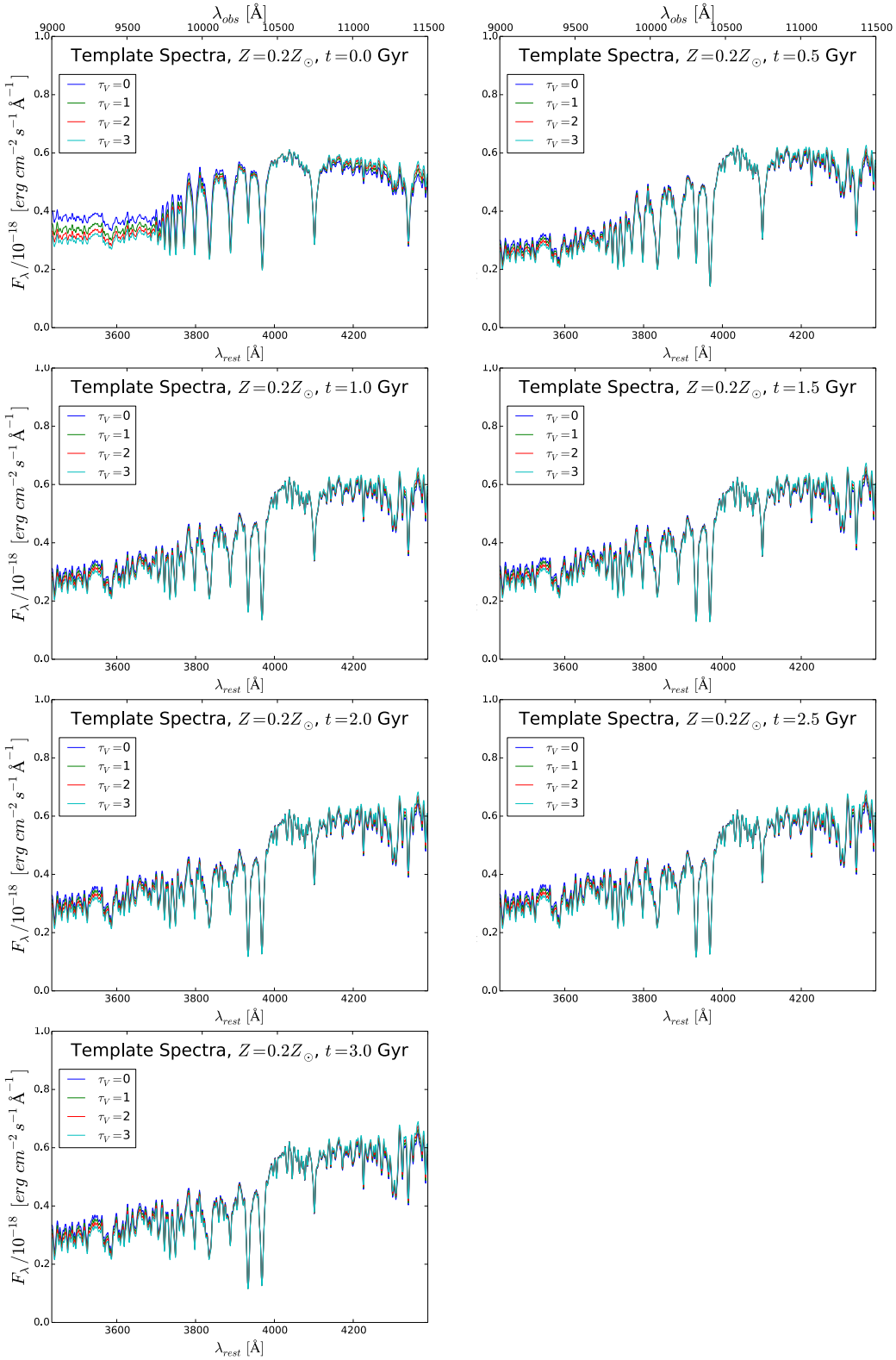

Figure A.10: Bruzual & Charlot GALAXEV spectra, normalized at an observed wavelength of 1250 nm, for galaxies with $Z/Z_\odot = 0.2$. Higher values of τ_V correspond to more extinction by dust. After the giant molecular birth clouds disperse 0.01 Gyr after star formation ends, the minor spectral differences caused by τ_V virtually disappear. The different plots correspond to different values of t.

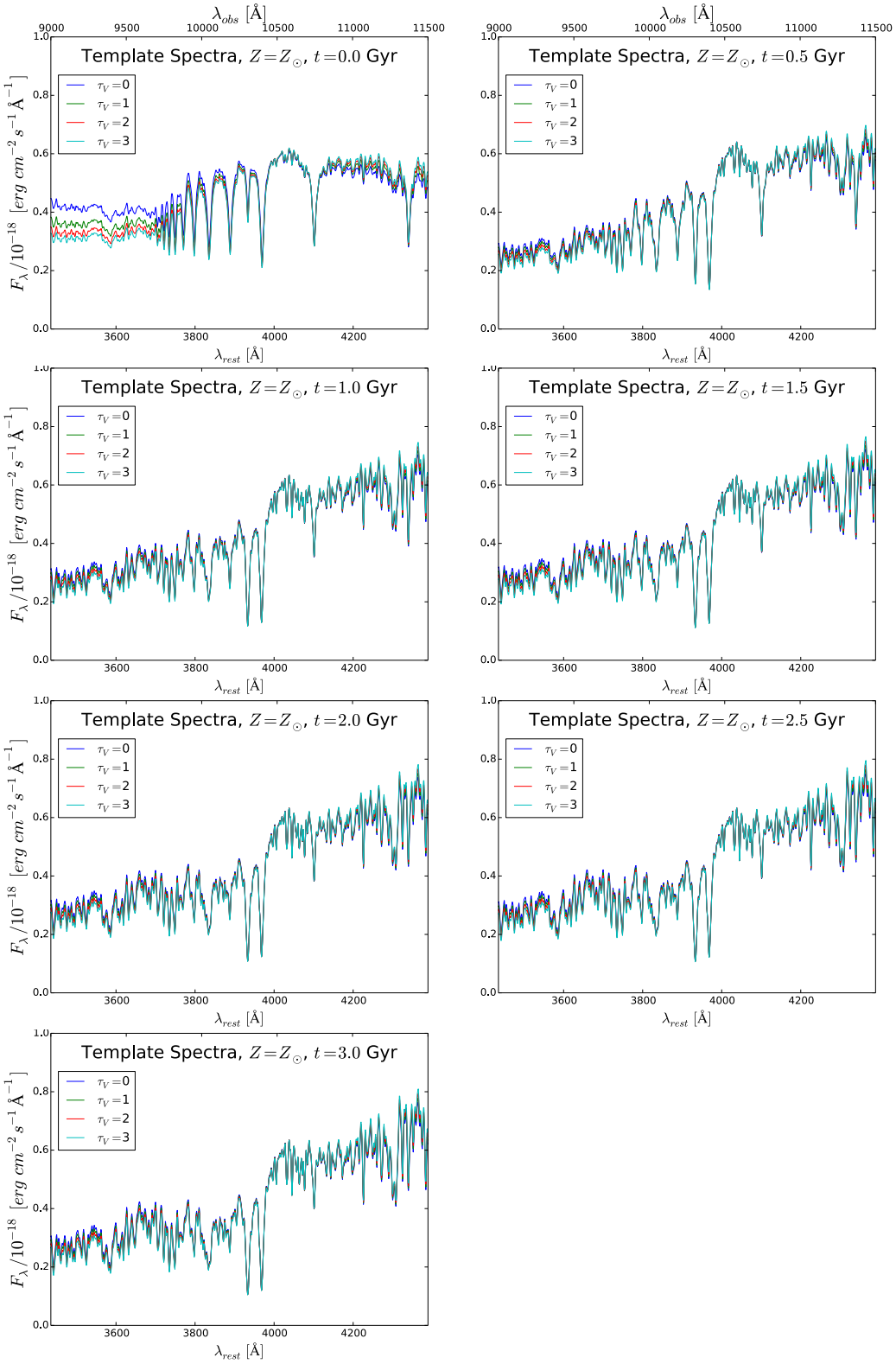

Figure A.11: Bruzual & Charlot GALAXEV spectra, normalized at an observed wavelength of 1250 nm, for galaxies with $Z/Z_\odot = 1.0$. Higher values of τ_V correspond to more extinction by dust. After the giant molecular birth clouds disperse 0.01 Gyr after star formation ends, the minor spectral differences caused by τ_V virtually disappear. The different plots correspond to different values of t.

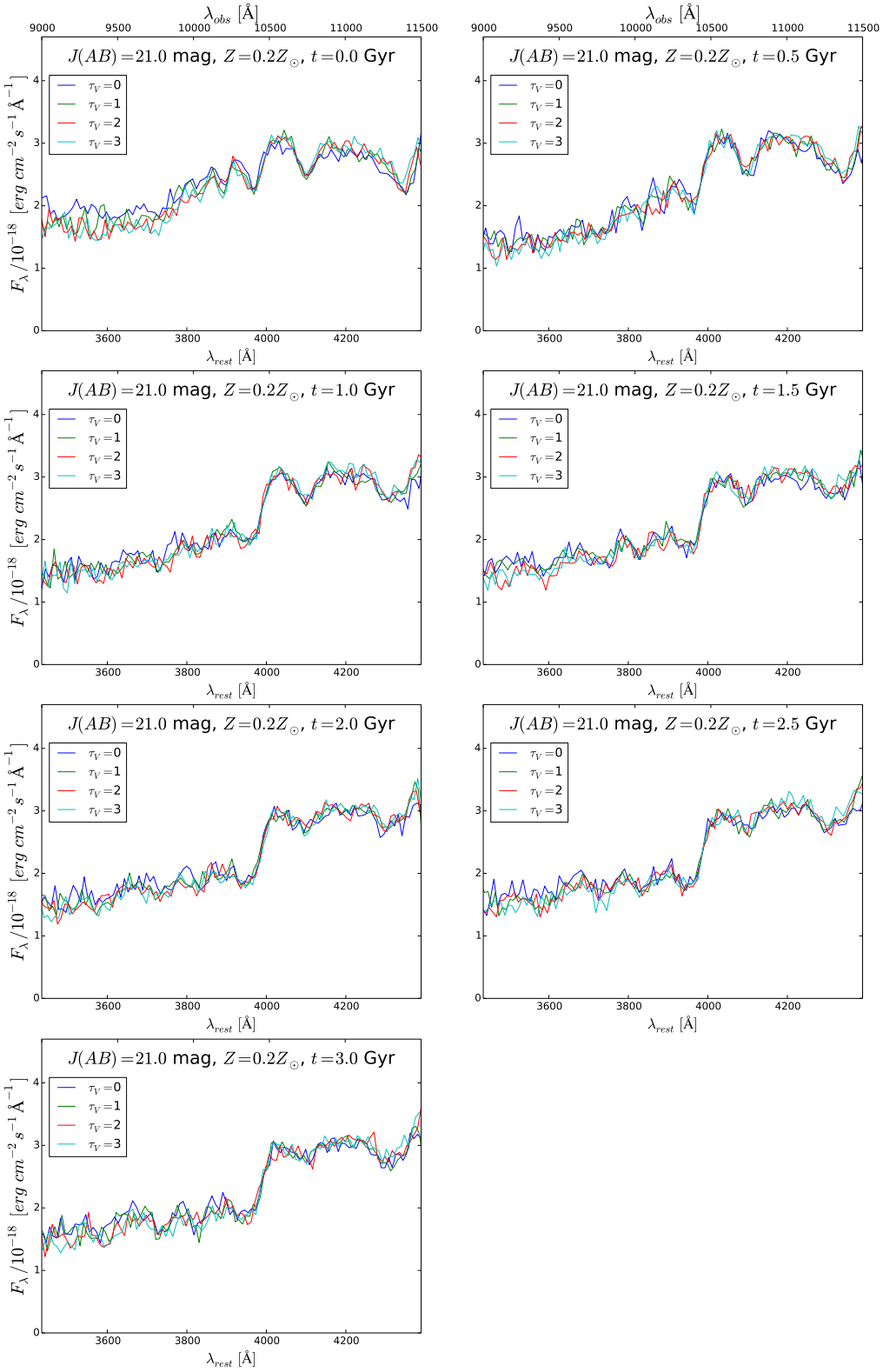

Figure A.12: Extracted aXeSIM spectra, normalized to 21.0 mag at an observed wavelength of 1250 nm, for galaxies with $Z/Z_\odot = 0.2$. Higher values of τ_V correspond to more extinction by dust. After the giant molecular birth clouds disperse 0.01 Gyr after star formation ends, the minor spectral differences caused by τ_V virtually disappear. The different plots correspond to different values of t.

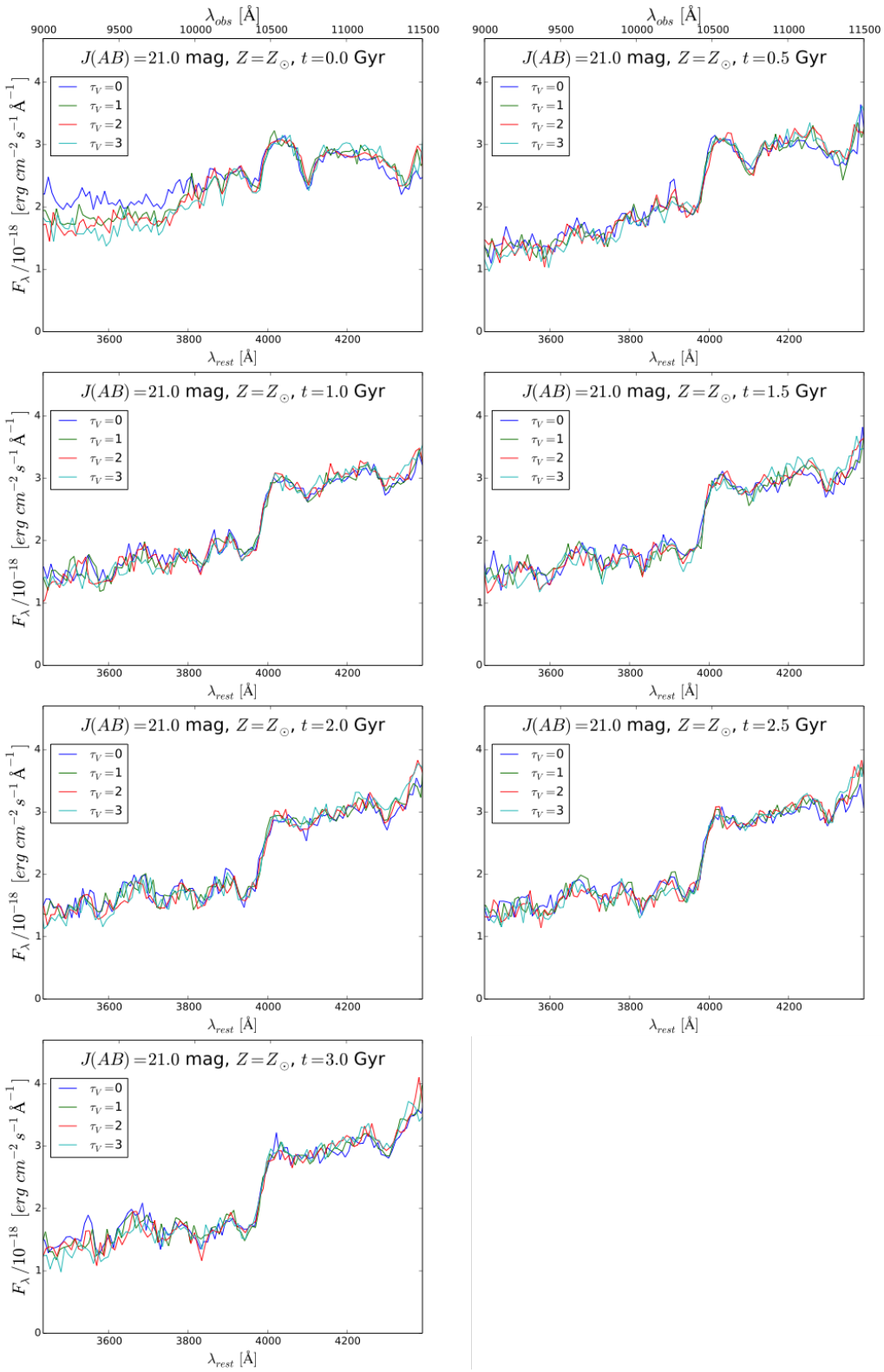

Figure A.13: Extracted aXeSIM spectra, normalized to 21.0 mag at an observed wavelength of 1250 nm, for galaxies with $Z/Z_\odot = 1.0$. Higher values of τ_V correspond to more extinction by dust. After the giant molecular birth clouds disperse 0.01 Gyr after star formation ends, the minor spectral differences caused by τ_V virtually disappear. The different plots correspond to different values of t.

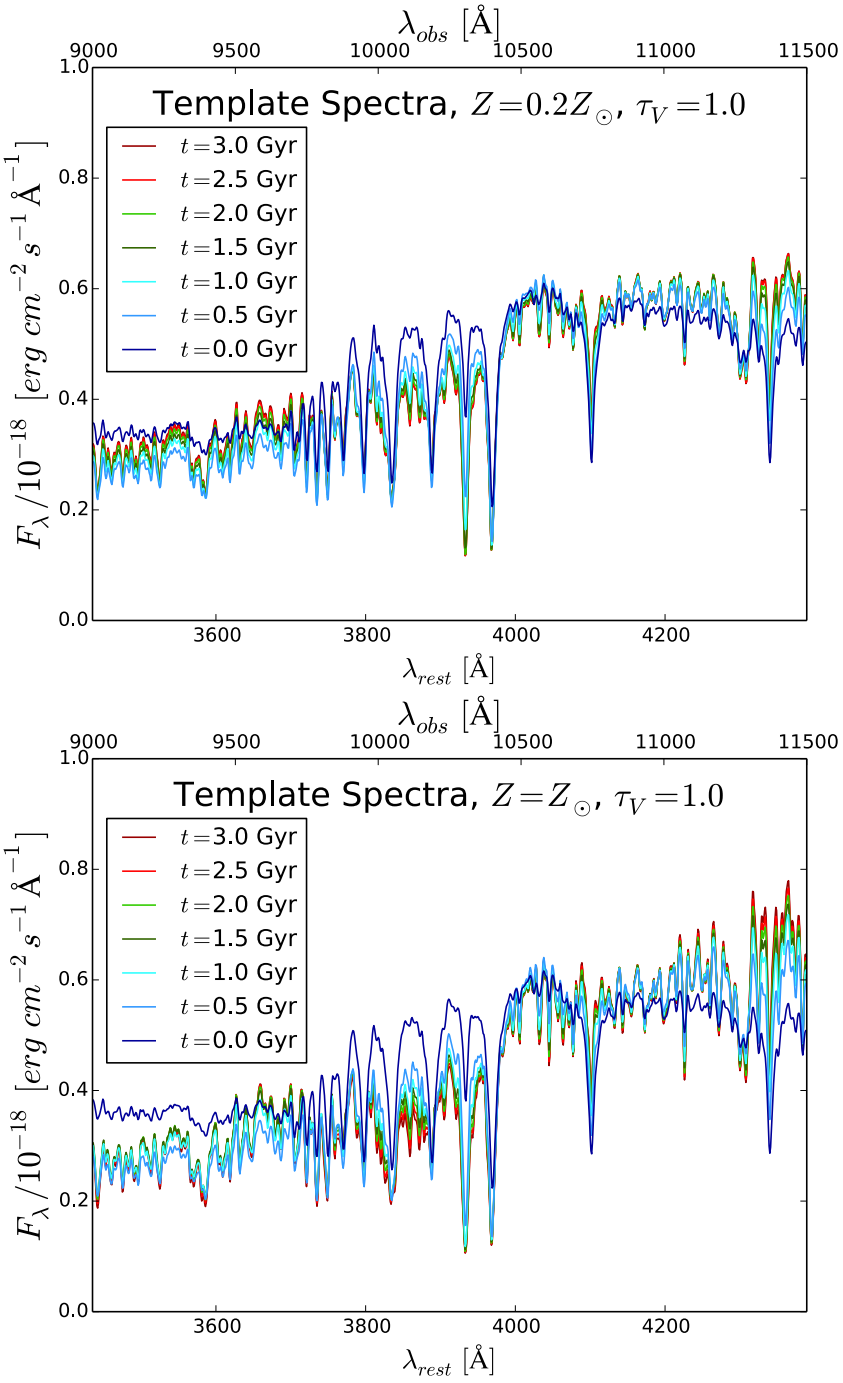

Figure A.14: Bruzual & Charlot GALAXEV spectra, normalized at an observed wavelength of 1250 nm, for galaxies with $\tau_V = 1.0$. Higher values of t correspond to a shorter period of constant star formation and a longer elapsed time since star formation ended. It is evident that the strength of the 4000 Å break increases with increasing t, with the largest jump occurring between the $t = 0.0$ Gyr spectrum and the $t = 0.5$ Gyr spectrum. The two plots correspond to different metal abundances: $Z/Z_\odot = 0.2$, and $Z/Z_\odot = 1.0$.

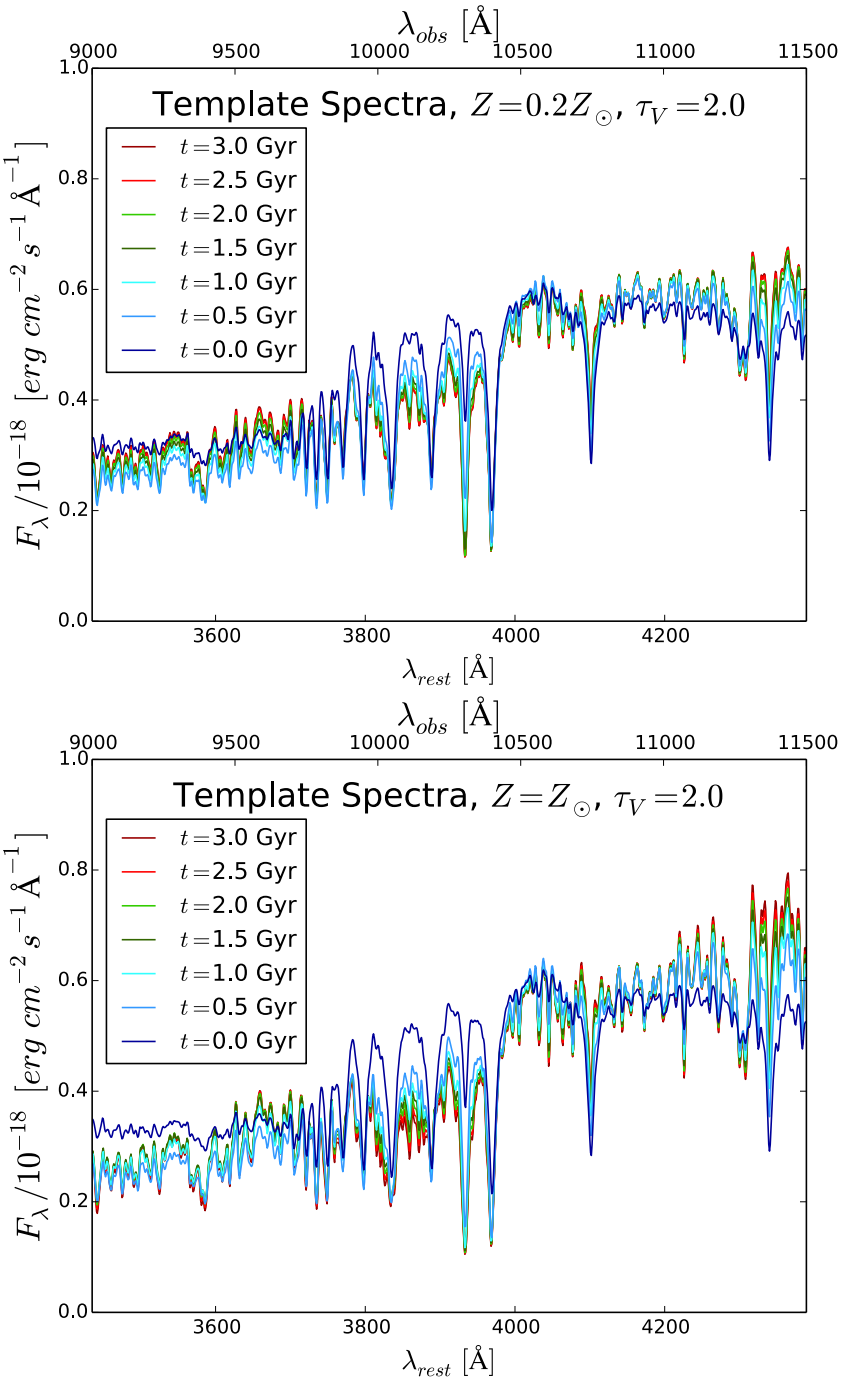

Figure A.15: Bruzual & Charlot GALAXEV spectra, normalized at an observed wavelength of 1250 nm, for galaxies with $\tau_V = 2.0$. Higher values of t correspond to a shorter period of constant star formation and a longer elapsed time since star formation ended. It is evident that the strength of the 4000 Å break increases with increasing t, with the largest jump occurring between the $t = 0.0$ Gyr spectrum and the $t = 0.5$ Gyr spectrum. The two plots correspond to different metal abundances: $Z/Z_\odot = 0.2$, and $Z/Z_\odot = 1.0$.

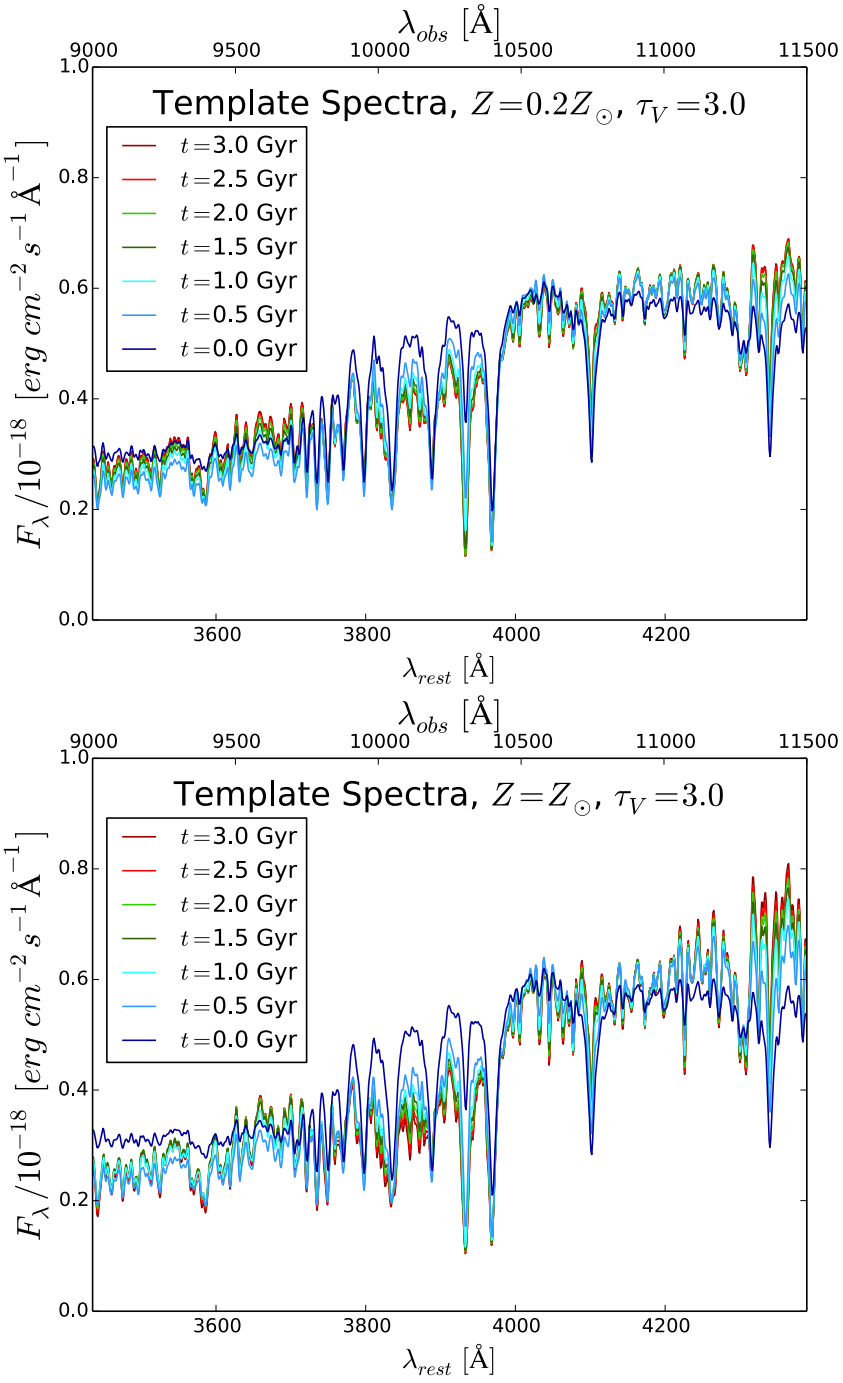

Figure A.16: Bruzual & Charlot GALAXEV spectra, normalized at an observed wavelength of 1250 nm, for galaxies with $\tau_V = 3.0$. Higher values of t correspond to a shorter period of constant star formation and a longer elapsed time since star formation ended. It is evident that the strength of the 4000 Å break increases with increasing t, with the largest jump occurring between the $t = 0.0$ Gyr spectrum and the $t = 0.5$ Gyr spectrum. The two plots correspond to different metal abundances: $Z/Z_\odot = 0.2$, and $Z/Z_\odot = 1.0$.

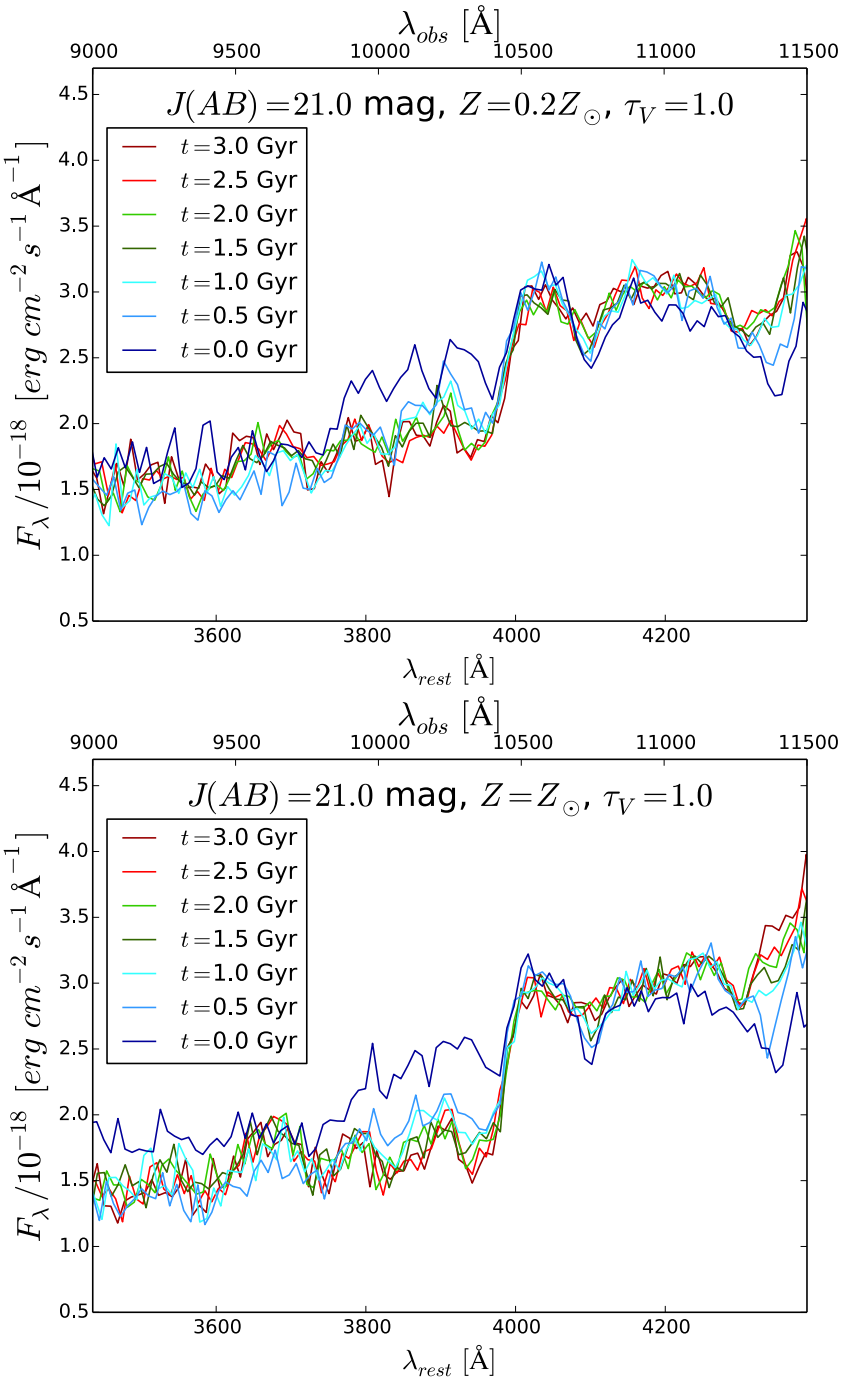

Figure A.17: Extracted aXeSIM spectra, normalized to 21.0 mag at an observed wavelength of 1250 nm, for galaxies with $\tau_V = 1.0$. Higher values of t correspond to a shorter period of constant star formation and a longer elapsed time since star formation ended. It is evident that the strength of the 4000 Å break increases with increasing t, with the largest jump occurring between the $t = 0.0$ Gyr spectrum and the $t = 0.5$ Gyr spectrum. The two plots correspond to different metal abundances: $Z/Z_\odot = 0.2$, and $Z/Z_\odot = 1.0$.

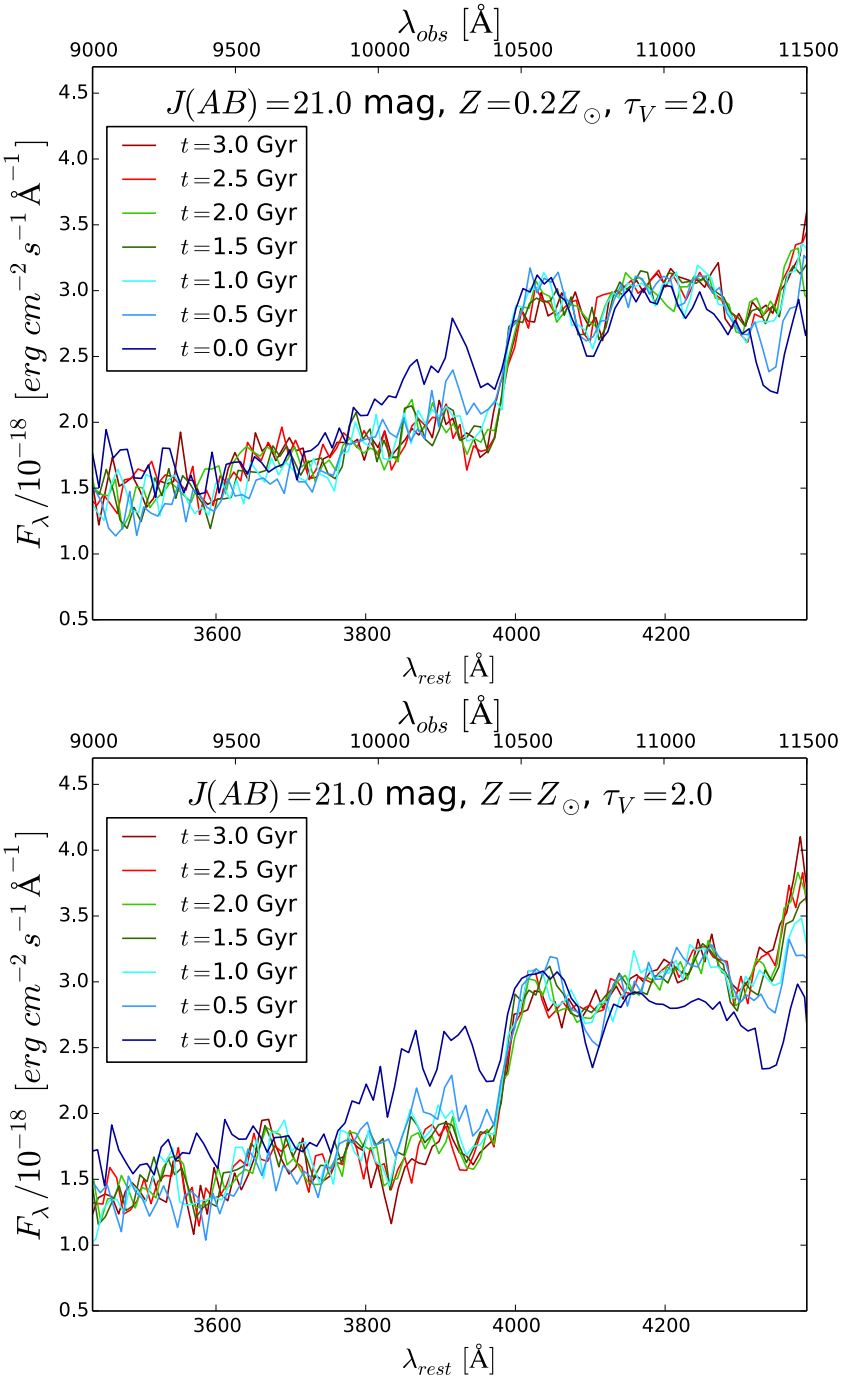

Figure A.18: Extracted aXeSIM spectra, normalized to 21.0 mag at an observed wavelength of 1250 nm, for galaxies with $\tau_V = 2.0$. Higher values of t correspond to a shorter period of constant star formation and a longer elapsed time since star formation ended. It is evident that the strength of the 4000 Å break increases with increasing t, with the largest jump occurring between the $t = 0.0$ Gyr spectrum and the $t = 0.5$ Gyr spectrum. The two plots correspond to different metal abundances: $Z/Z_\odot = 0.2$, and $Z/Z_\odot = 1.0$.

A.3 Systematic Errors

Potential systematic biases in the $D(4000)$ and $D_n(4000)$ measurements were investigated by comparing the measured values for the two indices to their intrinsic values for each galaxy and plotting the result against the stellar population parameters Z, τ_V, and t. Several of these plots are shown in Figures A.20, A.21, and A.22. There are no obvious trends in metallicity, dust extinction, or stellar age that are consistent across multiple parameter sets.

A.4 Random Errors

Random measurement errors, which increase at greater magnitudes, appear in aXeSIM extracted spectra due to readout and photon noise from sky background and from objects in the image. As with the other three galaxy template variables, I compared the measured values for $D(4000)$ and $D_n(4000)$ to their intrinsic values for each galaxy and plotted the result against magnitude to gain a better understanding of how uncertainties affect these measurements (see Figure A.23). The $D(4000)$ and $D_n(4000)$ measurements are almost always within 10% and often within 5% of their intrinsic values at all magnitudes with exceptions in $J(AB) = 22.8$ mag galaxies at $\tau_V = 3.0$, $Z/Z_\odot = 0.2$, and $t = 0.5$ and again at $\tau_V = 3.0$, $Z/Z_\odot = 0.2$, and $t = 0.0$. There were no noticeable trends with magnitude in $D(4000)_{measured}/D(4000)_{actual}$ that were consistent across multiple parameter sets.

Plots of the uncertainties in $D(4000)$ and $D_n(4000)$ versus magnitude can be found in Figures A.24 and A.25 for a subset of the galaxies in my grid of Bruzual & Charlot GALAXEV template galaxy spectra. The uncertainty increases at fainter magnitudes due to random error, and the random errors associated with the $D_n(4000)$ measurement are always greater than those of the $D(4000)$. Increasing metallicity, stellar age, and dust extinction all lead to slightly higher uncertainties in $D(4000)$. Percent uncertainties in $D(4000)$ can be found in Figures A.26 and A.27.

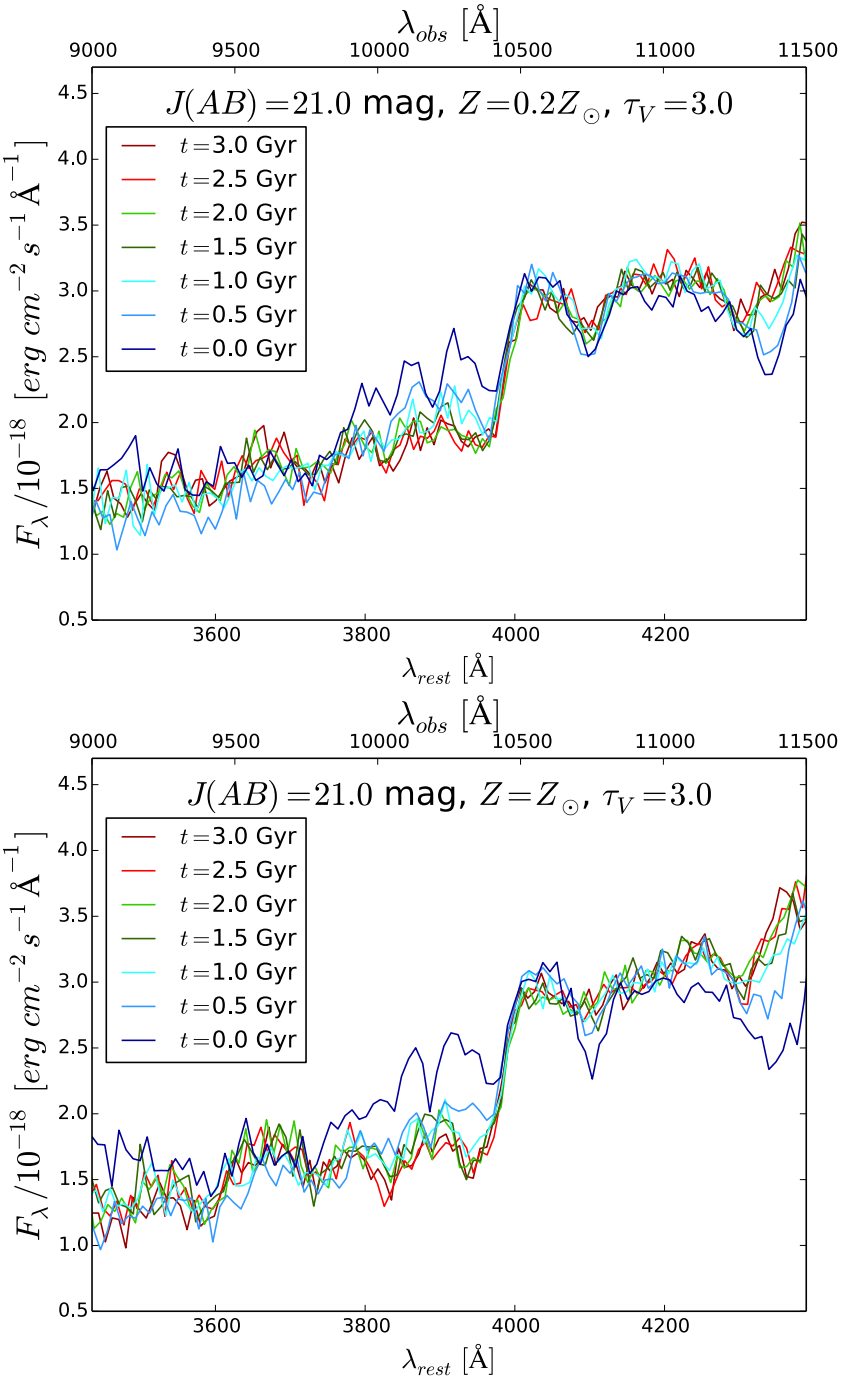

Figure A.19: Extracted aXeSIM spectra, normalized to 21.0 mag at an observed wavelength of 1250 nm, for galaxies with $\tau_V = 3.0$. Higher values of t correspond to a shorter period of constant star formation and a longer elapsed time since star formation ended. It is evident that the strength of the 4000 Å break increases with increasing t, with the largest jump occurring between the $t = 0.0$ Gyr spectrum and the $t = 0.5$ Gyr spectrum. The two plots correspond to different metal abundances: $Z/Z_\odot = 0.2$, and $Z/Z_\odot = 3.0$.

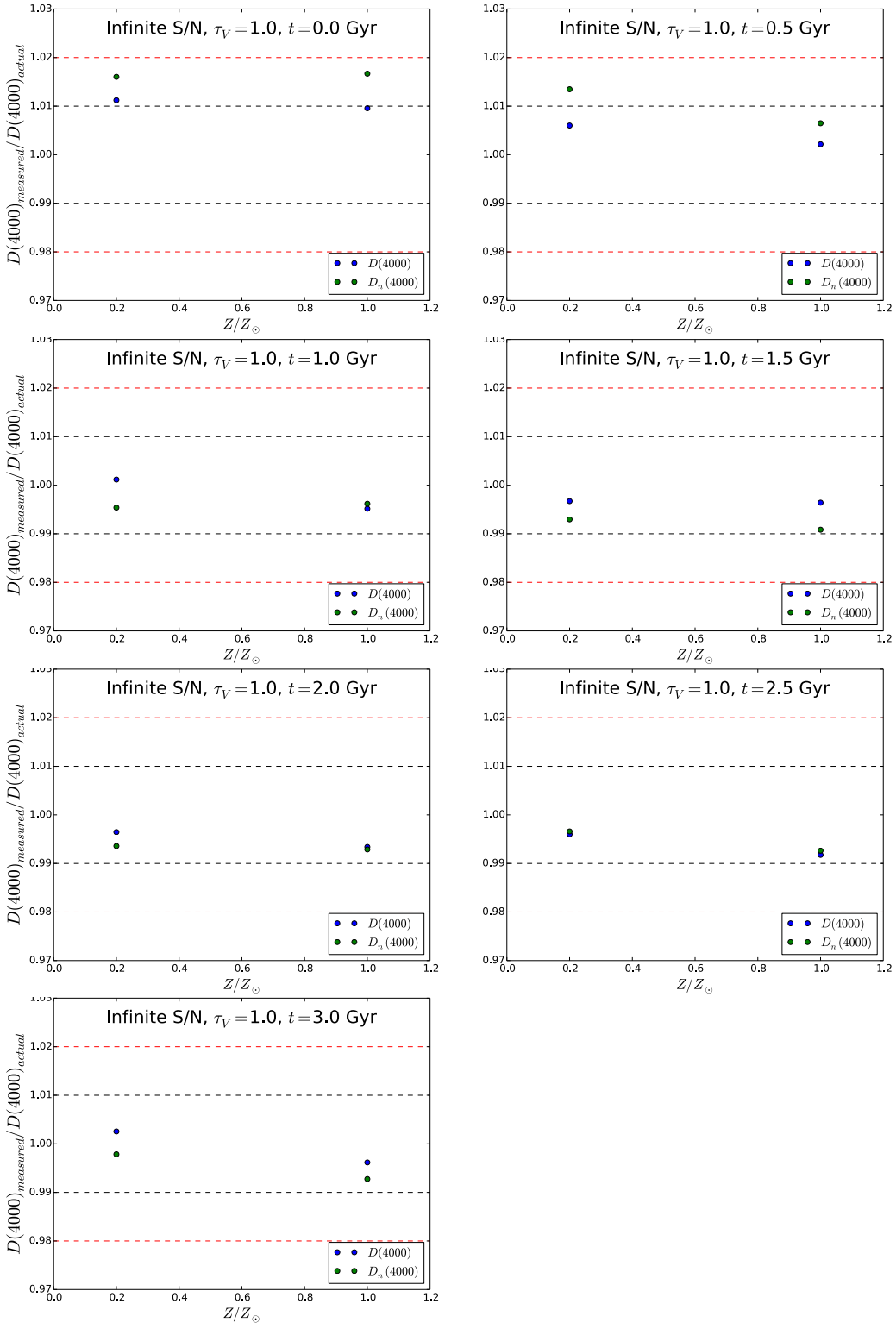

Figure A.20: The measured $D(4000)$ (or $D_n(4000)$) value divided by the intrinsic $D(4000)$ ($D_n(4000)$) measurement for galaxies with infinite signal-to-noise measurements and an optical depth of $\tau_V = 1.0$. The black dotted lines correspond to a 1% difference from unity, and the red dotted lines correspond to a 2% difference. The different plots correspond to different values of t.

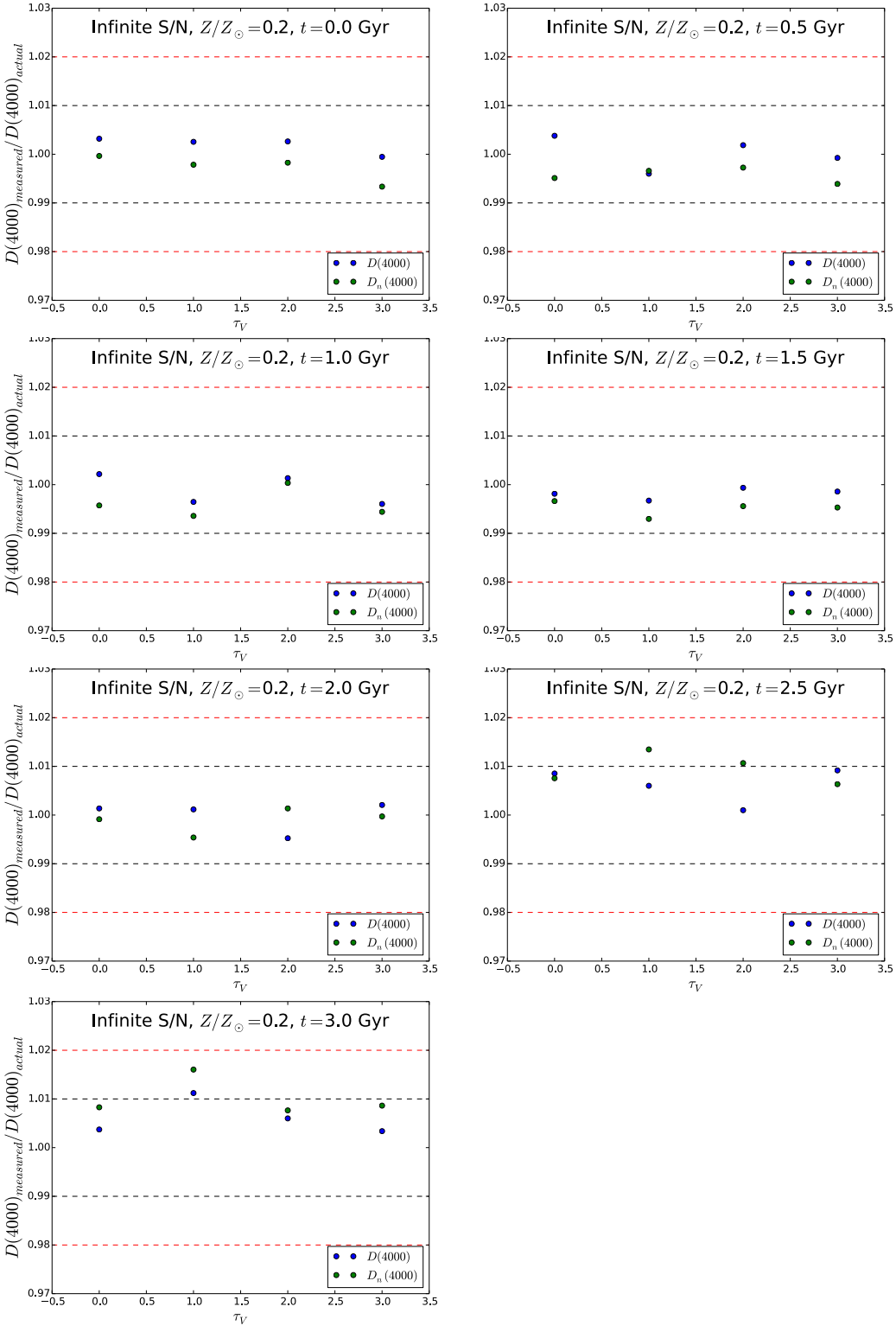

Figure A.21: The measured $D(4000)$ (or $D_n(4000)$) value divided by the intrinsic $D(4000)$ ($D_n(4000)$) measurement for galaxies with infinite signal-to-noise measurements and a metal abundance of $Z/Z_\odot = 0.2$. The black dotted lines correspond to a 1% difference from unity, and the red dotted lines correspond to a 2% difference. The different plots correspond to different values of t.

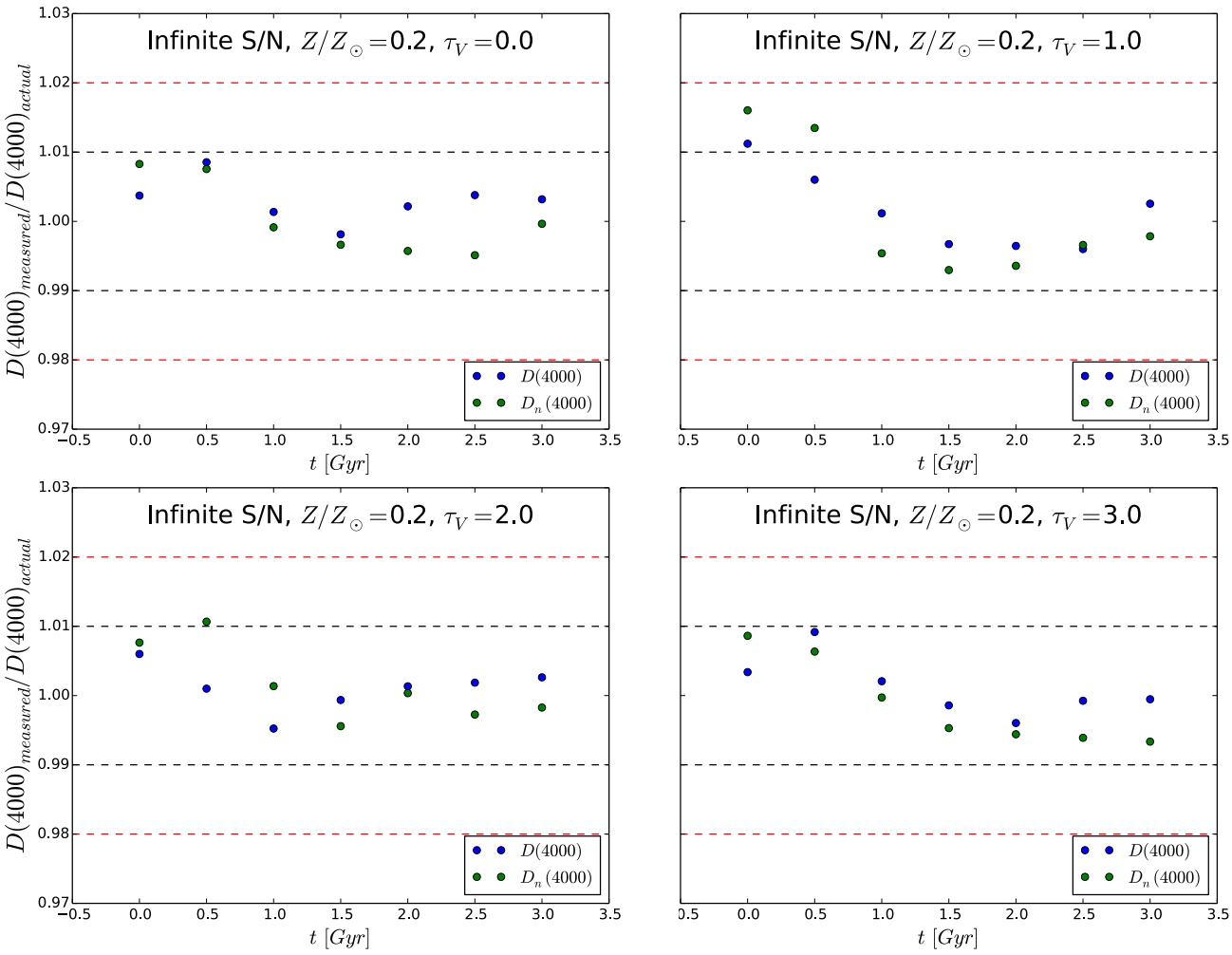

Figure A.22: The measured $D(4000)$ (or $D_n(4000)$) value divided by the intrinsic $D(4000)$ ($D_n(4000)$) measurement for galaxies with infinite signal-to-noise measurements and a metal abundance of $Z/Z_\odot = 0.2$. The black dotted lines correspond to a 1% difference from unity, and the red dotted lines correspond to a 2% difference. The different plots correspond to different values of τ_V.

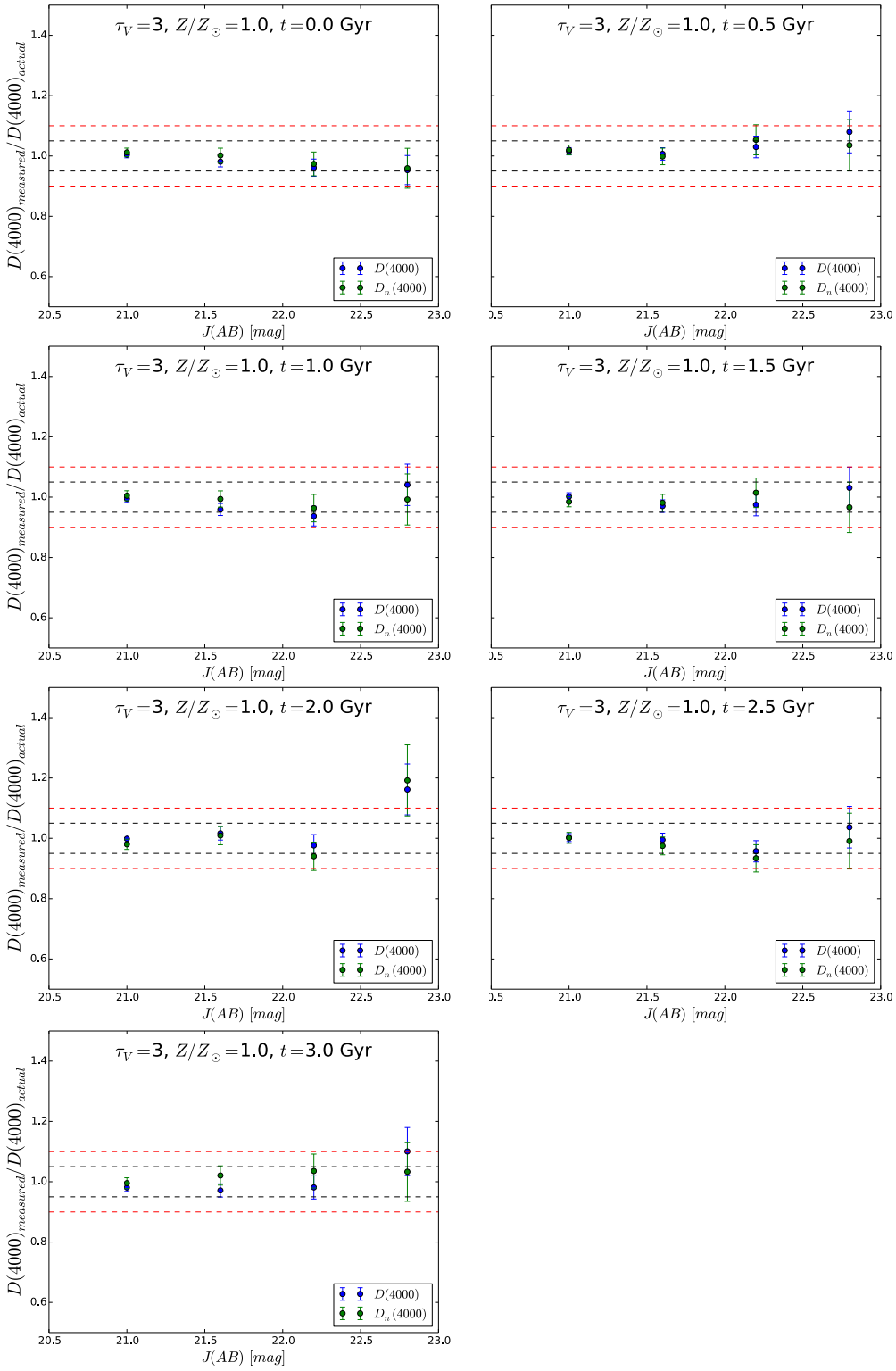

Figure A.23: The measured $D(4000)$ (or $D_n(4000)$) value divided by the intrinsic $D(4000)$ ($D_n(4000)$) measurement for galaxies attenuation optical depth $\tau_V = 3.0$ and metal abundance of $Z/Z_\odot = 1.0$. The black dotted lines correspond to a 5% difference from unity, and the red dotted lines correspond to a 10% difference. The different plots correspond to different values of t.

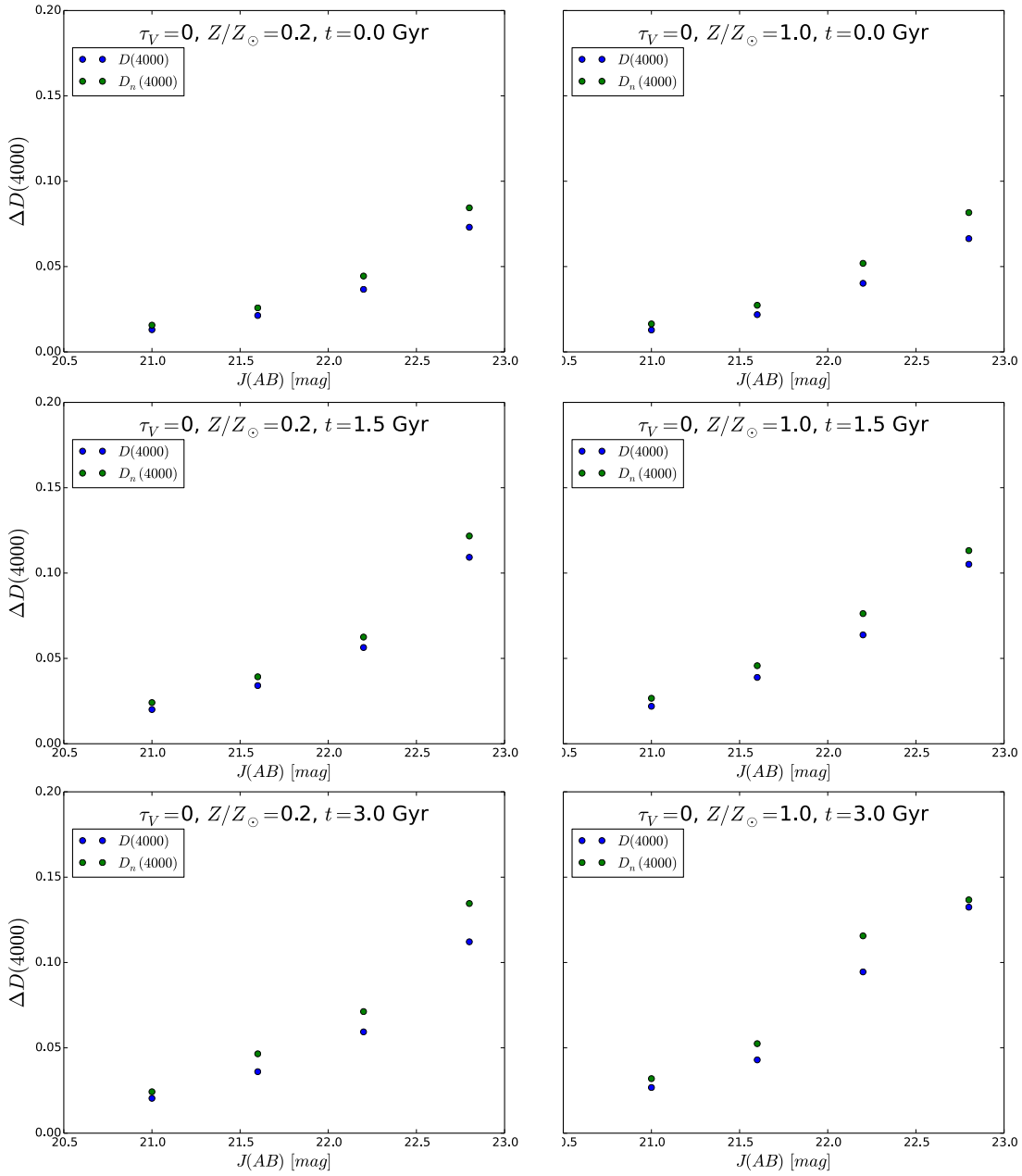

Figure A.24: Uncertainties $\Delta D(4000)$ in $D(4000)$ and $D_n(4000)$ plotted against the magnitudes considered in the feasibility study. $\Delta D(4000)$ always rises at fainter magnitudes, and the uncertainty in $D_n(4000)$ is always greater than that of $D(4000)$. The galaxies all have identical dust extinctions. Average stellar age increases from the top to the bottom of each column, and metallicity increases from the left to the right of each row. Increasing the metallicity or the stellar age leads to higher uncertainties in $D(4000)$ and $D_n(4000)$.

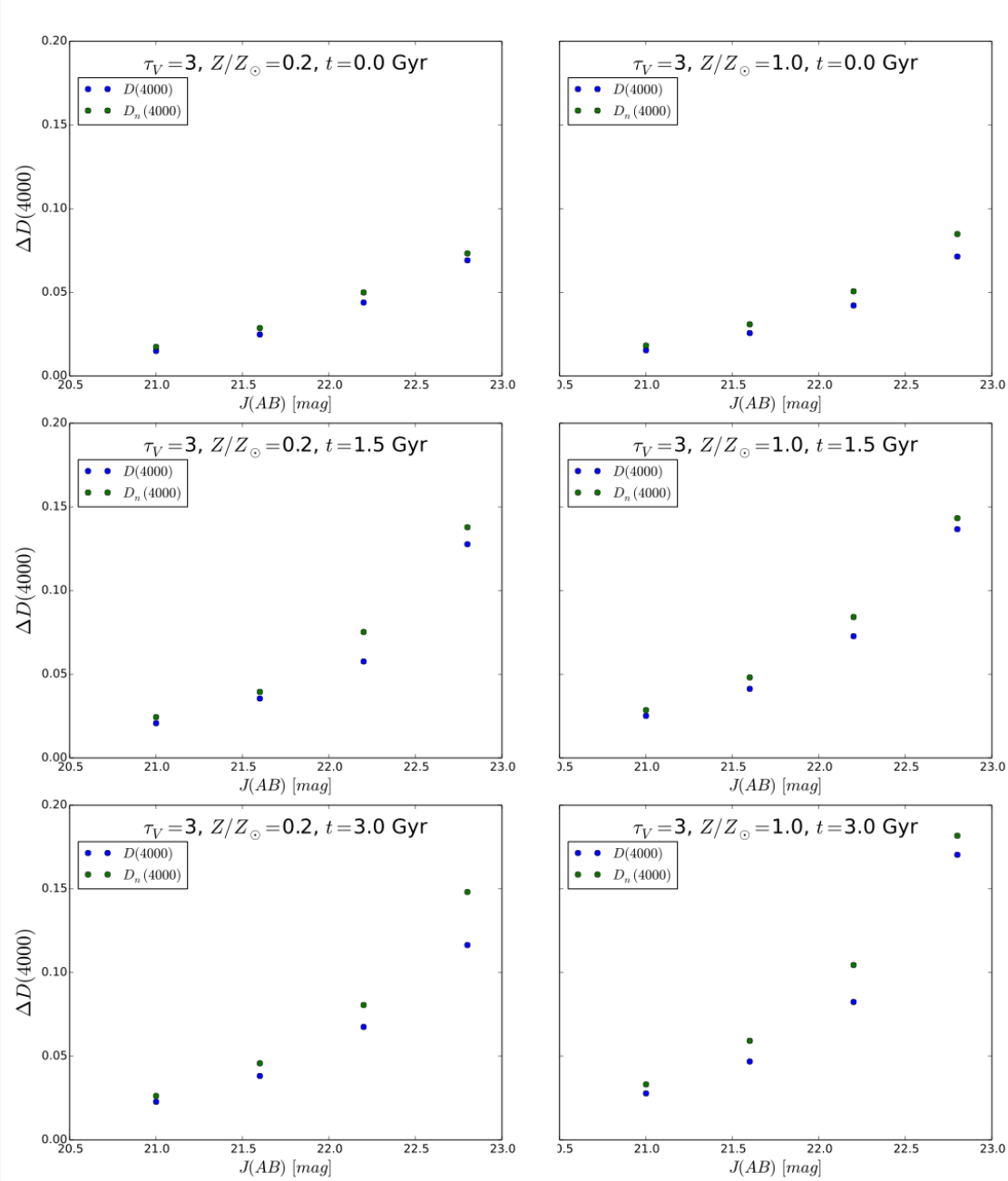

Figure A.25: Uncertainties $\Delta D(4000)$ in $D(4000)$ and $D_n(4000)$ plotted against the magnitudes considered in the feasibility study. $\Delta D(4000)$ always rises at fainter magnitudes, and the uncertainty in $D_n(4000)$ is always greater than that of $D(4000)$. The galaxies all have identical dust extinctions. Average stellar age increases from the top to the bottom of each column, and metallicity increases from the left to the right of each row. Increasing the metallicity or the stellar age leads to higher uncertainties in $D(4000)$ and $D_n(4000)$.

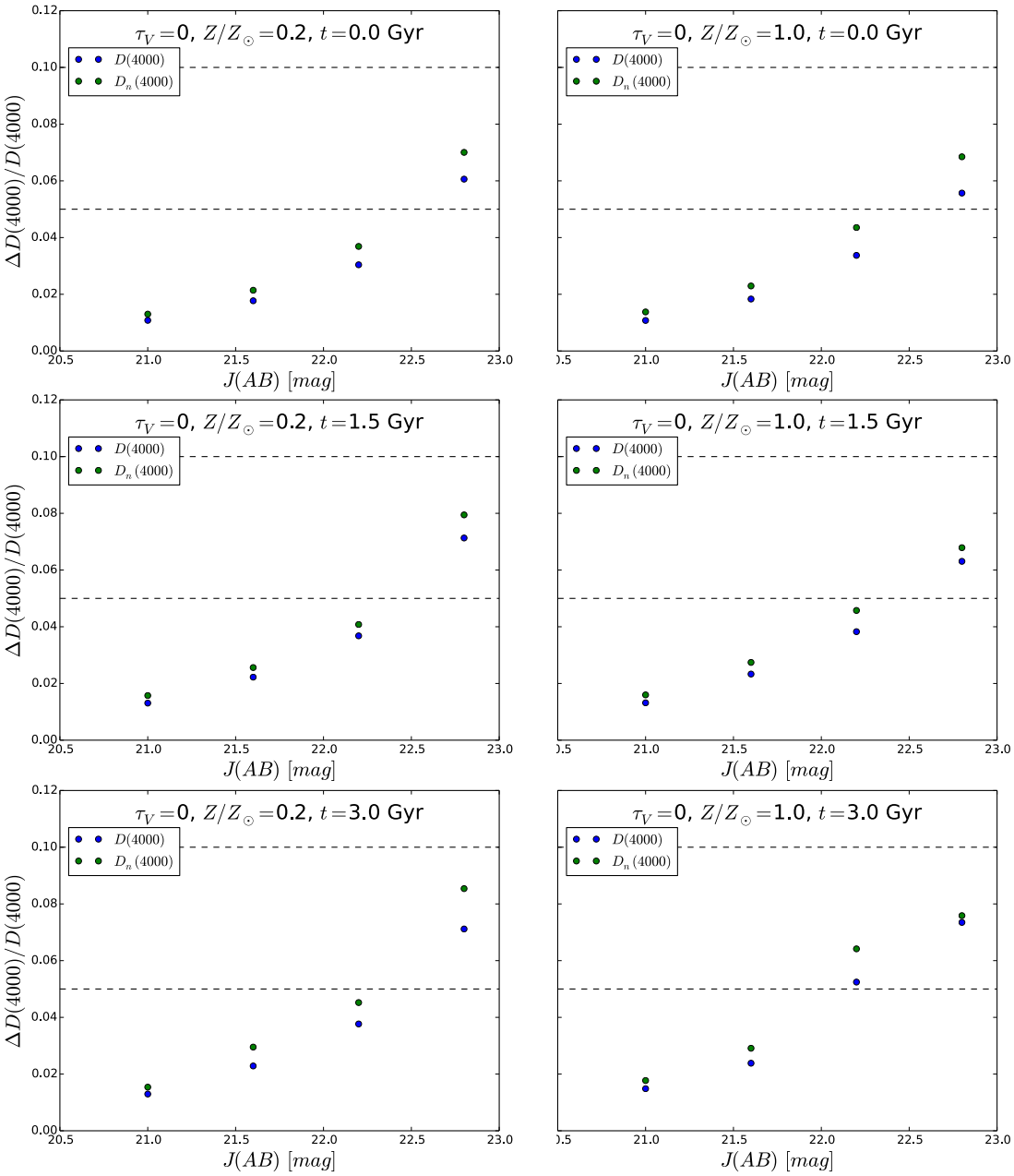

Figure A.26: Percent uncertainties $\Delta D(4000)$ in $D(4000)$ and $D_n(4000)$ plotted against the magnitudes considered in the feasibility study. The galaxies correspond to those in Figure A.24. As before, increasing the metallicity or the stellar age leads to higher uncertainties in $D(4000)$ and $D_n(4000)$.

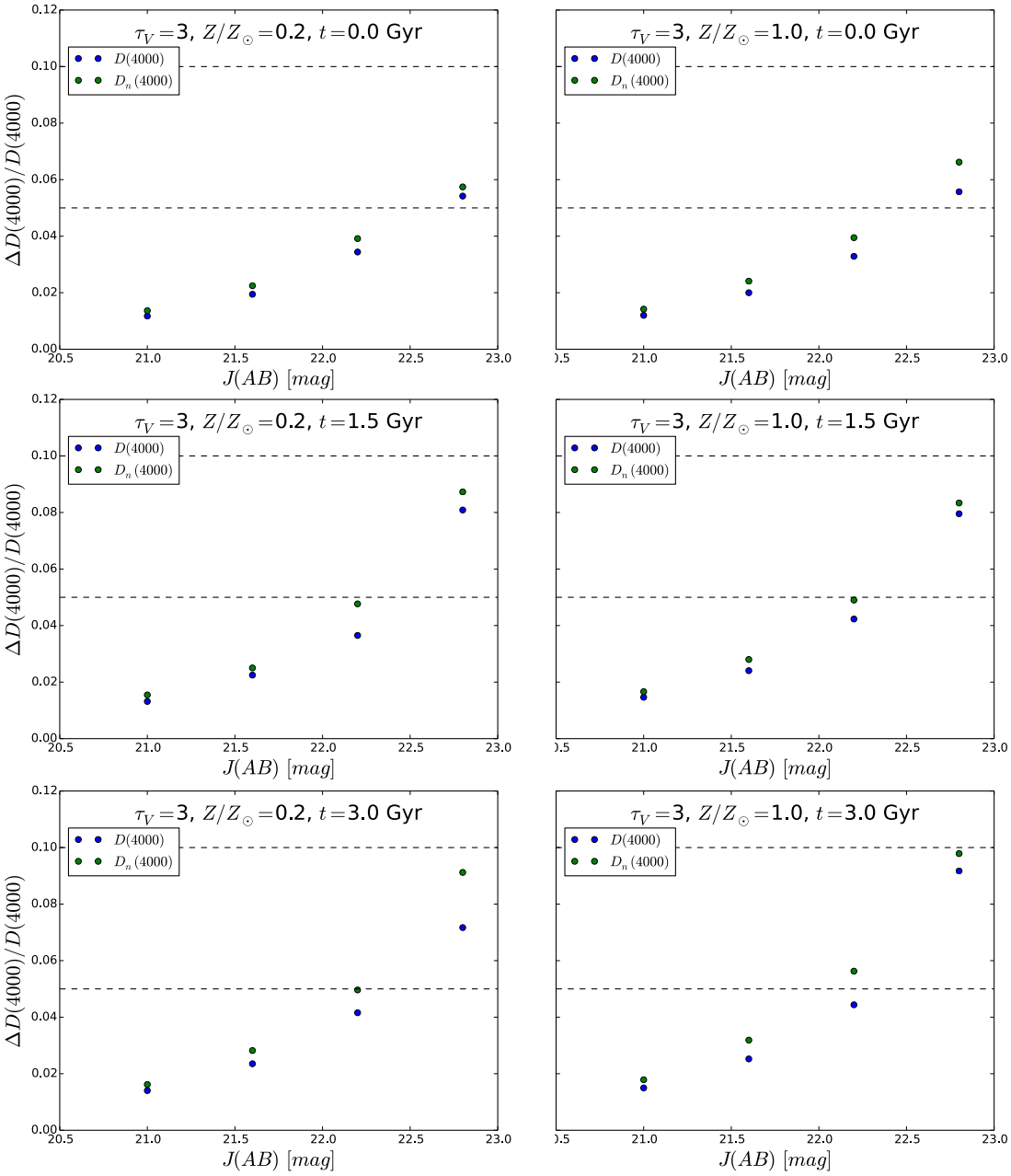

Figure A.27: Percent uncertainties $\Delta D(4000)$ in $D(4000)$ and $D_n(4000)$ plotted against the magnitudes considered in the feasibility study. The galaxies correspond to those in Figure A.25. As before, increasing the metallicity or the stellar age leads to higher uncertainties in $D(4000)$ and $D_n(4000)$.